CONTROL OF PHASE CENTRE AND POLARIZATION IN CIRCULAR MICROSTRIP ANTENNAS

By

Zahra Allahgholi Pour

A Thesis
submitted to the Faculty of Graduate Studies
in partial fulfillment of the requirements
for the degree of

Master of Science

Department of Electrical and Computer Engineering
The University of Manitoba
Winnipeg, Manitoba, Canada

THE UNIVERSITY OF MANITOBA

FACULTY OF GRADUATE STUDIES

*****

COPYRIGHT PERMISSION

CONTROL OF PHASE CENTRE AND POLARIZATION IN CIRCULAR MICROSTRIP ANTENNAS

BY

Zahra Allahgholi Pour

A Thesis/Practicum submitted to the Faculty of Graduate Studies of The University of Manitoba in partial fulfillment of the requirement of the degree

OF

MASTER OF SCIENCE

Acknowledgements

I would like to express my most sincere appreciation and gratitude to my academic and research advisor, Professor L. Shafai for his wise advice and invaluable guidance throughout my research. This work would not have been possible without his priceless support and encouragement.

I would also like to thank the members of my examining committee, Dr. G. Bridges and Dr. H. Soliman. Moreover, I especially want to thank Mr. B. Tabachnik for his technical support and Ms. S. Girardin for her extensive help, whenever it was needed, during my studies at The University of Manitoba.

Finally, I would like to thank my beloved family for their endless love and support.

ABSTRACT:

A microstrip antenna operating at the fundamental TM_{11} mode generates a broadside radiation pattern. As the higher order modes are excited, boresight-nulled patterns are formed and the beam peak direction moves toward the endfire, as the mode order increases. The phase centre of the microstrip antenna, when it is excited at a single mode, is located at the center of the patch. But, when two or more modes are excited, the phase centre is no longer located at the center of the patch and phase loci may exist instead of a single point.

In this thesis, the phase centre of multi-mode circular microstrip antennas is studied. To guarantee exact mode excitations, stacked patch configurations are considered and three cases are investigated, stacked TM_{11} and TM_{21} modes, TM_{11} and TM_{02} modes, and TM_{11}, TM_{21} and TM_{02} modes. In each case, the investigation is carried out for the phase centre, main beam tilt angle, radiation patterns and copolar and crosspolarization in terms of different mode amplitude and phase excitations. All three cases are treated both analytically and numerically. The case of special interest is when the beam is at broadside, generated by multiple modes, and the phase centre moves away from the patch center. This is equivalent to virtual antennas and has applications for remote sensing, and wireless communications. Dependence of the phase centre location on the mode excitation is investigated. Effects of the mode excitations on the radiation patterns, especially the crosspolarization are also studied.

Table of Contents

List of Figures

List of Tables

Chapter 1

Introduction

1.1 Preface

Microstrip antennas have been receiving widespread attentions in communication systems due to their attractive features of light weight, low cost, conformal profile, and ease of fabrication. The concept of these antennas was first proposed by Deschamps [1] in 1953 and patented in France in 1955 by Gutton and Baissinot [2]. The microstrip antenna consists of a very thin metallic strip or patch placed on a small fraction of a wavelength above a ground plane so that the patch and the ground plane are separated by a dielectric sheet. The radiating patch may have any geometrical shape like square, rectangular, circular and elliptical [3]. They can also be used as a feed for the reflector antennas in satellite or terrestrial applications. In this particular application, it is important to know the phase centre of the feed and to have low crosspolarization. There are a number of work dealing with the phase centre and polarization properties of microstrip antenna, operating in the fundamental mode. This thesis investigates the phase centre and polarization properties of a circular microstrip patch antenna operating at the fundamental and higher order modes and shows how they can be controlled.

1.2 Literature review

In some applications, like high-performance radio local area network (HIPERLAN) [4], global positioning systems (GPS) [5], radar and military applications, boresight-nulled radiation patterns are desired. This feature can be provided by microstrip patch antennas operating at higher order modes. The peak direction of these patterns moves toward the endfire by increasing the mode index number [6], which will be explained in detail later. Moreover, in some particular applications like GPS, radar, and military programs, it is important to know the phase centre location of the antenna.

Although there are many papers dealing with the theoretical and experimental aspects of higher order microstrip antennas, there are only a limited publications related to their phase centre. In [7], a phased array antenna was developed using self scanning elements, which could be N-stacked circular microstrip patch antennas, operating at the TM_{n1} modes. It was shown that, the element radiation pattern can be shaped and scanned. This can reduce the grating lobe effects by setting a null of the element pattern at its location and enhance the array gain, allowing the use of fewer elements than in conventional phased array antennas. The concept also simplified the required beam forming network due to the smaller number of elements.

Authors in [8] studied the input impedance of a circular microstrip antenna at the fundamental and higher order modes, as well as the effects of feed probe and the ground plane size, on the resonant frequency.

Microstrip patch antennas can be used as a feed for reflector antennas. They can be either a single feed for a prime-focus reflector or an array feed for offset or dual reflectors [9]. However, they suffer from narrow impedance bandwidth, asymmetrical

radiation pattern and high backlobe level, which have made them impractical for reflector feeds in the past. In [10], the circular microstrip antennas were optimized to overcome these problems. It was shown that, the backlobe level can be reduced by adding a $\frac{\lambda}{4}$ choke to the side wall or the ground plane of the antenna, and the crosspolarization can be reduced by controlling the ground plane size, which affects the symmetry of the radiation pattern. The bandwidth can be improved by stacking technique or parasitic coupling to adjacent patches. The effects of ground plane size, feed location, dielectric permittivity of the substrate and substrate thickness on the radiation patterns and mode excitation of circular microstrip antennas were also studied in [11]. It was shown that, the patch size and the feed position can control the mode excitation efficiency. As a rule, by moving the feed toward the edge of a circular microstrip antenna, the efficiency of higher order mode excitation is increased.

In [12], authors did investigations into defining an "effective point of radiation" (EPR) for a rectangular microstrip antenna operating at the fundamental mode through two methods: "phase-centre method" and "group-delay" method. However, no investigation has been conducted on the phase centre of circular microstrip antennas, when operating simultaneously in multiple modes, including the TM_{11}, TM_{21} and TM_{02} modes.

This thesis investigates the phase centre and polarization properties of circular microstrip antennas, excited at the fundamental mode and the next two higher order modes in a stacked configuration. It is shown that, by controlling the excitation amplitude and phase of each mode, one can control the radiation pattern, phase centre location and crosspolarization of the antenna. These have been done both analytically and

numerically. It is shown that, the peak radiation pattern and the phase centre location can be controlled simultaneously. In particular, when the peak radiation pattern is at the boresight angle, the phase centre location can be moved away from the antenna center. This case can lead to the virtual antenna concept, and the antenna can be made to have more than one phase centre by altering sequentially its excitation. That is, it becomes equivalent to multiple antennas. This property can be used in many applications in remote sensing and signal processing techniques.

1.3 Structure of the thesis

The thesis is presented in seven chapters. Chapter one covers introduction and literature review on the topic and describes its overall goals. Chapter two gives the background theory on circular microstrip antennas, to show how they radiate at the fundamental and higher order modes, through formulation of the problem. The definition of phase centre is also reviewed in this chapter along with the proposed theory. The radiation properties and the phase centre of a two-layer stacked circular microstrip antenna operating at the TM_{11} and TM_{21} modes is addressed in chapter three, which are treated both analytically based on the cavity model, and numerically by a Method of Moment, MOM, using Ansoft Designer version 2. In this chapter, two cases are considered in terms of the angle between the two excitation ports of the modes, when both are along the X-axis and when placed 45 degrees away from each other. Chapter four repeats the same procedure as chapter three for the fundamental TM_{11} mode, and TM_{02} mode, except due to the symmetry of TM_{02} mode, only one case is reported. A three-layer stacked circular patch antenna operating at the first three modes is studied in

chapter five, in terms of the radiation patterns, main beam tilt angle, phase centre location, copolarization and crosspolarization. It is shown that, by adding a proper ratio of the TM_{02} mode, the crosspolarization of this structure can be decreased. In chapter six, practical techniques to feed the proposed antenna are introduced. Finally, the conclusion and future work are given in chapter seven.

Chapter 2

Circular Microstrip Antenna Theory

2.1 Introduction

Microstrip antennas are well known because of their attractive features, like light weight, low cost, capability of integrating with active circuits and ease of fabrication, which makes them good candidates for wireless applications. On the other hand, they have a few disadvantages, like narrow bandwidth, surface wave excitation, that need to be overcome. Basically, a microstrip antenna consists of a patch etched on a grounded dielectric substrate. The geometry of the patch can be any shape: rectangular, circular, triangular etc, among them the circular microstrip antenna is studied in this thesis.

There are several methods to analyze a circular microstrip antenna, the cavity model, mode matching with edge admittance, the generalized transmission-line model, finite difference time domain (FDTD), and integral equation approach [13]. Here, the cavity model has been used to formulate the problem, which is accurate for our studies. As mentioned before, to verify the results, simulations have also been done using Ansoft Designer package version 2, which employs the full wave analysis by using the Method of Moment.

In this chapter, the basic background theory of circular microstrip patch antennas, operating at the fundamental and higher order modes, is reviewed along with the definition of the phase centre. The proposed theory is also introduced.

2.2 General principles of circular microstrip antenna

When the substrate thickness is much smaller than the wavelength, the normal fields can be assumed constant in the cavity region, between the patch and the ground plane, assuming the patch is parallel to the x-y plane. Therefore, the electric field within the cavity has only the normal component and the magnetic field has only transverse components. For this structure, the electric current on the microstrip patch has no component normal to the edge of the patch, implying a negligible tangential component of the magnetic field along the edge $(\partial E_z / \partial n = 0)$. With these assumptions, the circular patch antenna can be modeled as a cylindrical cavity bounded by electrical walls at its top and bottom and magnetic wall all along the periphery [13]. Thus, only the transverse magnetic or TM_{nm} modes can be excited in this type of antennas, and for small heights the TE modes are non-propagating.

The circular microstrip patch antennas can produce broadside radiation patterns while operating at the fundamental mode (TM_{11}). They produce boresight-nulled radiation patterns while working at the higher order modes. The peak radiation moves toward the endfire direction as "n", the mode index, increases, and they are capable of covering a fairly wide angular range up to 70 degrees from the broadside [6].

2.2.1 Resonant frequency

The basic geometry of a circular microstrip patch antenna is shown in Fig. 2.1 including a thin metalized circular disk on a grounded dielectric substrate. By using the cavity model [13] the fields within the dielectric region of the microstrip cavity, for the TM_{nm} modes, can be determined by solving the wave equation. When there is no excitation current, this equation can be expressed as:

$$\left(\nabla^2 + k^2\right)\vec{E} = 0 \qquad k = 2\pi\sqrt{\varepsilon_r}/\lambda_0 \tag{2.1}$$

Where ε_r is the dielectric constant of the substrate, λ_0 is the free space wavelength, and k is the propagation constant. The solution of equation 2.1, in the cylindrical coordinates, which must satisfy the magnetic wall boundary conditions is:

$$E_z = E_0 J_n(k\rho)\cos n\phi \tag{2.2}$$

Where $J_n(k\rho)$ are the Bessel functions of order n.

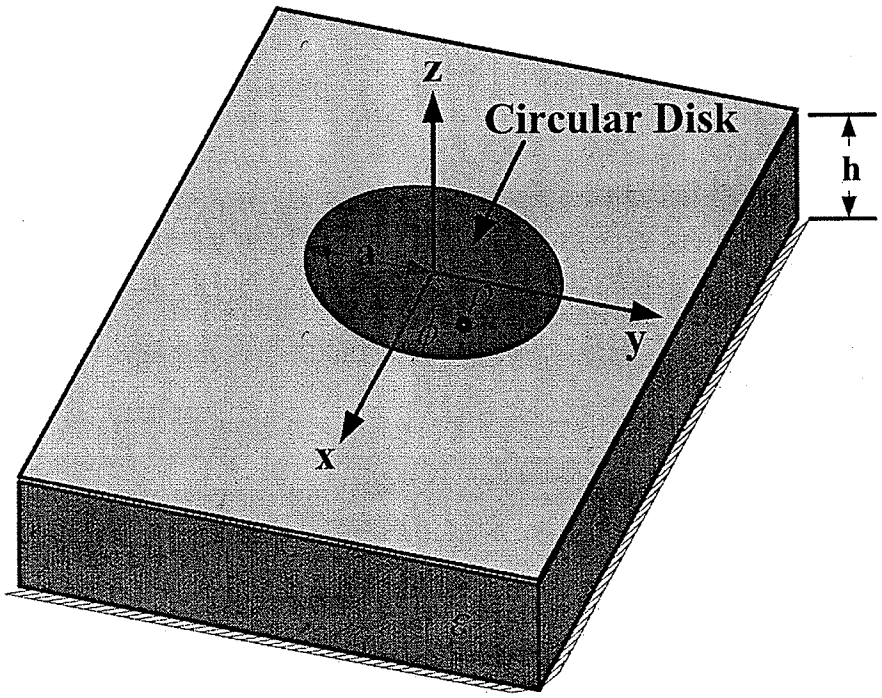

Fig 2.1 Configuration of a circular microstrip patch antenna

Since the electric field has only the z-component and $\partial E_z / \partial z \equiv 0$, the magnetic field components will be:

$$H_\rho = \frac{j}{\omega\mu\rho}\frac{\partial E_z}{\partial \phi} = -\frac{jn}{\omega\mu\rho}E_0 J_n(k\rho)\sin n\phi \qquad (2.3)$$

$$H_\phi = -\frac{j}{\omega\mu}\frac{\partial E_z}{\partial \rho} = -\frac{jk}{\omega\mu}E_0 J_n'(k\rho)\cos n\phi \qquad (2.4)$$

Where the prime sign indicates differentiation with respect to the argument. The other field components are zero inside the cavity,

$$E_\rho = E_\phi = H_z = 0 \qquad (2.5)$$

The magnetic wall boundary condition requires that the tangential magnetic field at the edge of the disk to be zero,

$$H_\phi(\rho = a) = 0 \qquad (2.6)$$

Where a is the radius of the circular patch. Thus,

$$J_n'(ka) = 0 \qquad (2.7)$$

Therefore, for each mode, a particular radius can be found associated with the zeros of the derivative of the Bessel functions [14]. Thus, the resonant frequency of circular microstrip antennas can be determined from the following equation:

$$f_{nm} = \frac{\chi'_{nm} C}{2\pi a_e \sqrt{\varepsilon_r}} \qquad (2.8)$$

Where χ'_{nm} is the m^{th} zero of $J_n'(ka)$, C is the velocity of light in free space, and a_e is the effective radius of the patch, taking into account the fringing effect.

The first seven order modes are listed in Table 2.1 in ascending order of χ'_{nm} value. It shows that the mode corresponding to $n = m = 1$ has the smallest radius, or resonant frequency, and is known as the dominant mode.

Mode (n,m)	0,1	1,1	2,1	0,2	3,1	4,1	1,2
Root χ'_{nm} or $k_{nm}a$	0	1.84118	3.05424	3.83171	4.20119	5.317	5.331

Table 2.1 Roots of $J'_n(ka)=0$ for TM_{nm} modes for circular microstrip patch [13]

As mentioned before, the effective radius of the disk is slightly larger than the physical one, due to the fringing fields along the edge of the resonator. For the fundamental mode, the following relationship gives an error less than 2.5% for $a/h>>1$ [15]:

$$a_e = a\left[1+\frac{2h}{\pi a\varepsilon_r}\left(\ln\frac{\pi a}{2h}+1.7726\right)\right]^{1/2} \qquad (2.9)$$

Based on [16], the fringing effects should be modified for higher order modes by taking into account the mode variables, n and m, to obtain a better accuracy. Therefore, equation 2.9 should be modified as below for all modes [16],

$$a_e = a\left[1+\frac{2h}{\pi a\varepsilon_r}\left(\ln\frac{\pi a}{2h\alpha^2}.\beta^3+1.7726\right)\right]^{1/2} \qquad (2.10)$$

where,

$$\alpha=\begin{Bmatrix} n, n\geq 1 \\ 1, n=0 \end{Bmatrix}, \quad \text{for all values of m when } \beta = m \qquad (2.11)$$

All above equations are valid when the patch is etched over an infinite ground plane.

At a given frequency and identical dielectric constant, the radius of a disk antenna becomes larger at higher order modes, because the corresponding eigenvalues increase as shown in table 2.1.

2.2.2 Radiation Pattern

The radiation patterns of the circular disk, in the upper half space, are derived using the image theory and replacing the infinite ground plane by doubling the equivalent magnetic current [14]. The antenna is located at the center of the coordinates. As one can expect, displacing the antenna from the origin of the coordinates produces a phase term, playing a prominent role, in our studies due to its impact on the phase centre of the antenna. Based on this fact, we have considered the general case, when the center of the circular disk is placed at $(r_0, \phi_0, 0)$, as shown in Fig. 2.2.

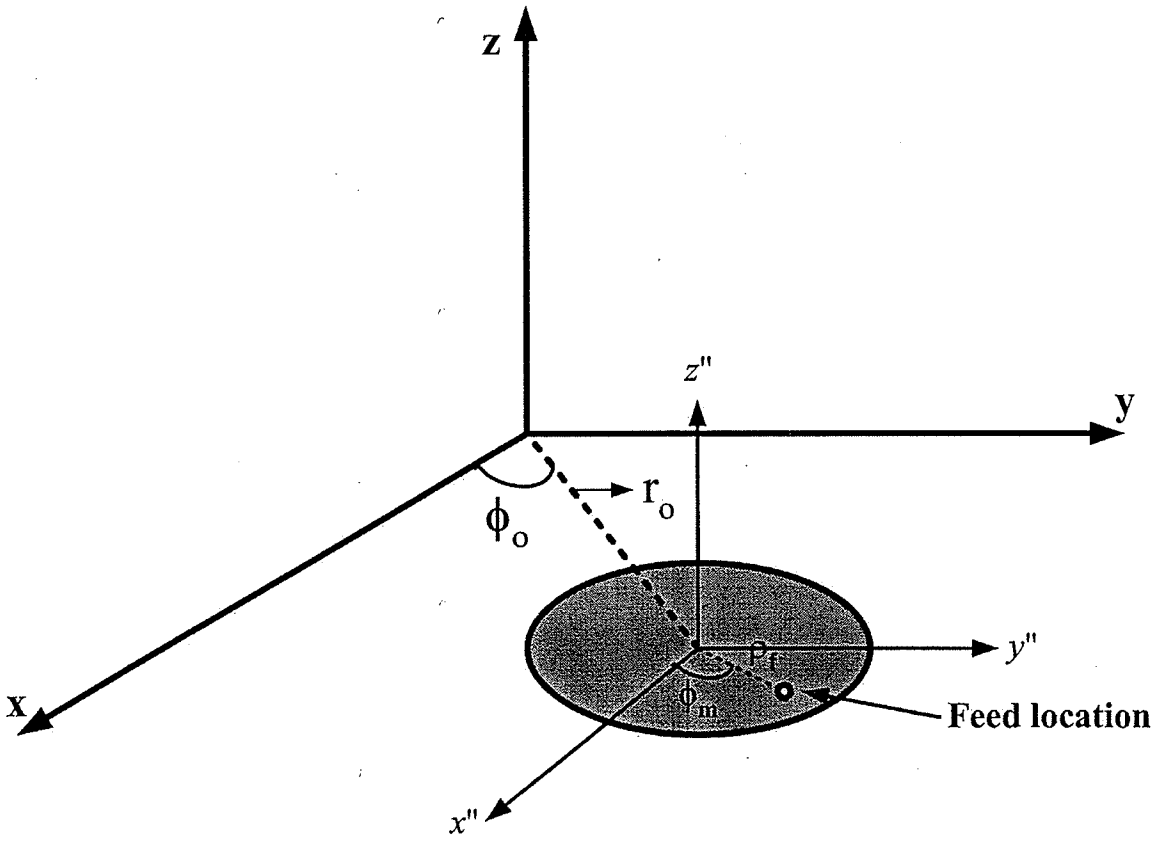

Fig. 2.2 The geometry of a circular disk antenna when its center is located at $(r_0, \phi_0, 0)$

The far fields corresponding to the TM_{nm} modes are given as,

$$E_\theta = -j^n \frac{V_n a_n k_o}{2} \frac{e^{-jk_0 r}}{r} e^{jk_0 r_o \sin\theta\cos(\phi-\phi_0)} \left[J_{n-1}(k_0 a\sin\theta) - J_{n+1}(k_0 a\sin\theta)\right]\cos n(\phi-\phi_m) \qquad (2.12)$$

$$E_\phi = j^n \frac{V_n a_n k_o}{2} \frac{e^{-jk_0 r}}{r} e^{jk_0 r_o \sin\theta\cos(\phi-\phi_0)} \left[J_{n-1}(k_0 a\sin\theta) + J_{n+1}(k_0 a\sin\theta)\right]\cos\theta \sin n(\phi-\phi_m) \qquad (2.13)$$

Where $V_n = hE_n J_n(\chi'_{nm})$ and is known as the edge voltage at $\phi = 0$, a is the physical radius of the patch and ϕ_m* is the angular location of the feed, k_0 is the free space propagation constant and (r_0, ϕ_0) is the coordinates of the antenna center. The term $e^{jk_0 r_o \sin\theta\cos(\phi-\phi_0)}$ stands for the far field phase of the antenna and depends on the location of the antenna as we expected. In order to simplify equations 2.12 and 2.13, the mode constant factor, C_n, may be defined as,

$$C_n = \frac{V_n a_n k_o}{2} \quad , \quad C_n = |C_n| \angle \alpha_n \qquad (2.14)$$

In the above equations, the effect of dielectric substrate, h, on the phase distribution has been neglected since it is very small with respect to wavelength for the microstrip patch antennas. Otherwise, an additional phase term, $e^{jk_0 h\cos\theta}$, due to the z-displacement, should be added to the equations 2.12 and 2.13.

Figure 2.3 shows the magnitudes of E_θ and E_ϕ for the dominant mode, and the next two higher order modes, including TM_{21} and TM_{02} modes. As can be seen, the peak radiation patterns are moved toward the endfire direction. These patterns have been plotted for a single patch antenna with ε_r=1.15 and h=1.5mm over an infinite ground plane, based on equations 2.12 and 2.13.

---

* Please note that the index "m" in "ϕ_m" is not the same as the one in the mode index "nm". ϕ_m just shows the angular location of the feed.

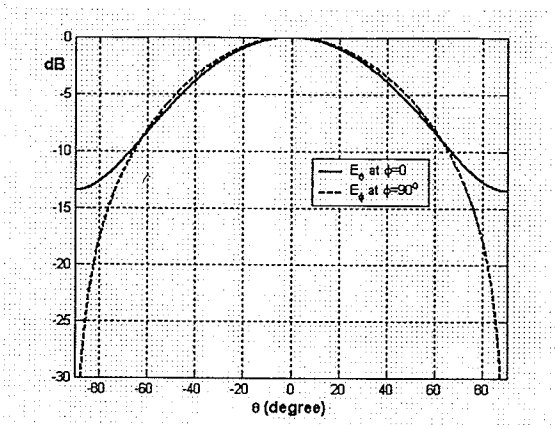

(a)

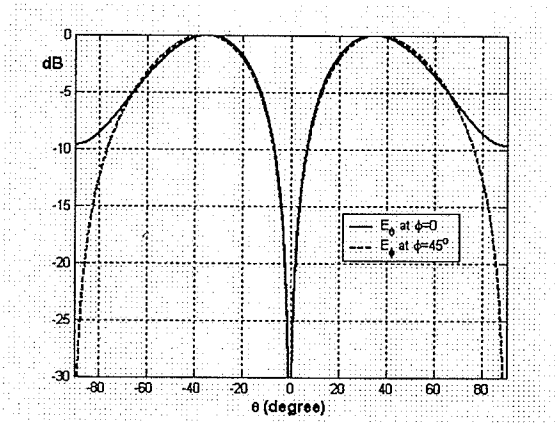

(b)

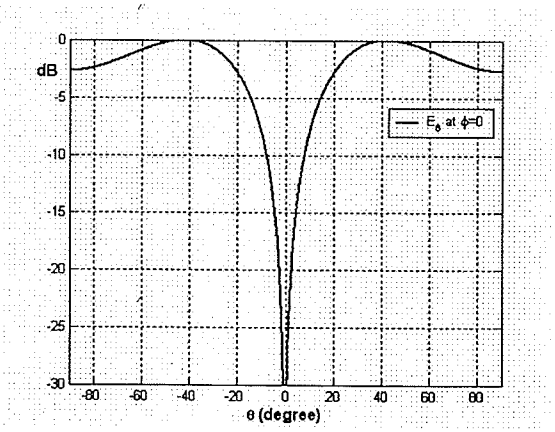

(c)

Fig. 2.3 The magnitude of E_θ and E_ϕ of higher order mode circular microstrip antenna, ε_r=1.15 and h=1.5mm, f=10GHz. (a) TM_{11} mode (b) TM_{21} mode (c) TM_{02} mode

2.2.3 Feed point location

Conventional microstrip patch antennas have a small bandwidth in each mode, due to their resonant structures. It is, therefore, important to excite each mode properly, in order to have a relatively pure mode, which depends on both disk size and location of the feed [8]. In reality, however all modes are excited, although only one mode is required. It is possible to eliminate the effects of other modes by placing the feed at the optimum location.

In [8], the input impedance of a circular microstrip patch antenna was studied for the dominant and higher order modes: The input standing wave ratios of the antenna, versus feed location, are shown in Fig. 2.4. The antenna was considered on a finite ground plane, when the radius of the ground plane was 1.3 times that of the disk.

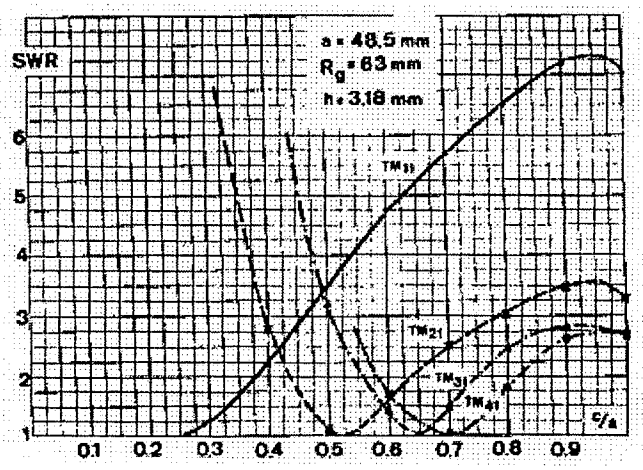

Fig. 2.4 Circular patch antenna input standing wave ratio (SWR) versus feed location [8]

As a summary, Table 2.2 lists the best feed location for the first four modes of the circular patch antenna based on Fig. 2.4.

Mode	Feed Location (ρ_f / a)
TM_{11}	0.25
TM_{21}	0.5
TM_{31}	0.65
TM_{41}	0.7

Table 2.2 Ratio of feed location to disk radius for some modes

From the above information, one can conclude that, the location of the probe feed moves away from the patch center as the mode index, n, increases. Another study in [11] shows the effect of feed location on the excitation efficiency of the TM_{11} and TM_{21} modes. Figure 2.5 illustrates these effects on the fundamental and TM_{21} modes. As can be seen, for the TM_{11} mode, moving the feed toward the edge of the patch increases the effects of TM_{21} and TM_{02} modes, while for the TM_{21} mode the best feed location, in terms of having minimum effects of other modes, is at $\rho_f = 0.75a$ [11].

Among all TM_{nm} modes, TM_{0m} modes have found special attention in applications where circular symmetric patterns are needed, as they can generate omnidirectional patterns, in azimuth, similar to a monopole. The TM_{01} mode is the static mode. Thus, in this thesis, we will study the properties of the TM_{02} mode, which will be shown to have a pronounced effect on crosspolarization. The excitation of the $n = 0$ modes needs a central feeding probe, where the electric field is the strongest [17].

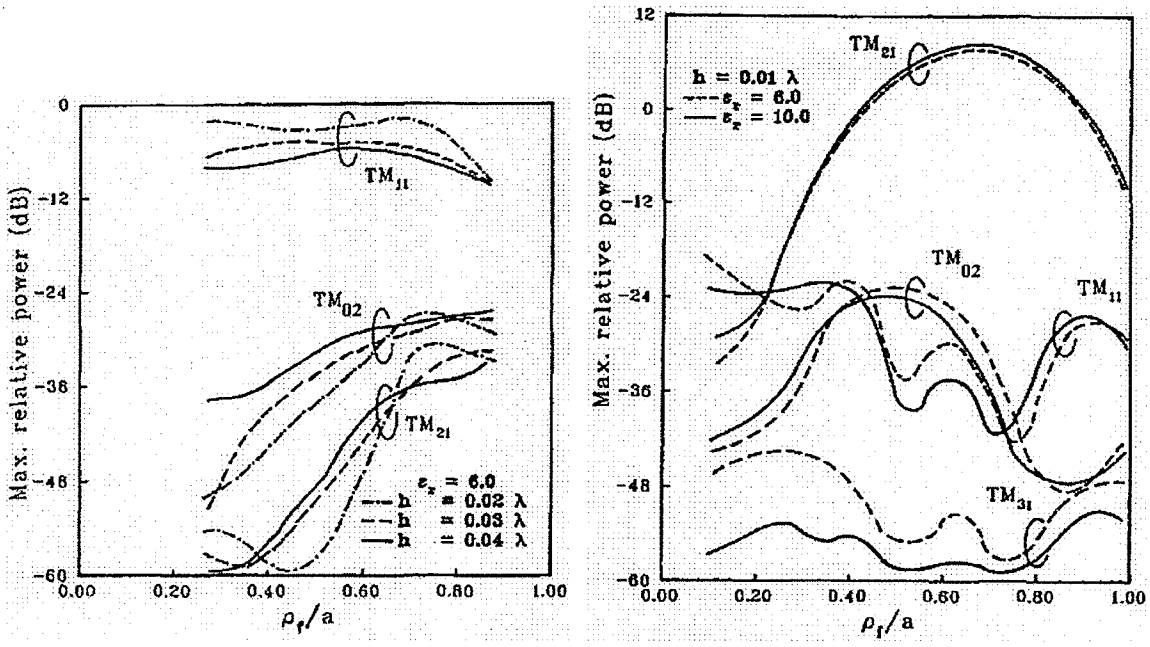

Fig. 2.5 The effect of feed position on the excitation efficiency of

(a) TM_{11} mode (b) TM_{21}mode [11]

2.2.4 Directivity

The directivity is a measure of the directional properties of an antenna, compared to that of an isotropic antenna [13], which has equal radiation intensity in all directions, thus, its directivity is unity. The directivity is defined as the ratio of the maximum power density in the main beam direction to the average radiated power density. Mathematically, it is given by [13],

$$D = \frac{\frac{1}{2}\mathrm{Re}\left(E_\theta H_\phi^* - E_\phi H_\theta^*\right)\big|_{\theta=\theta_{MAX}}}{P_r / 4\pi r^2} = \frac{\frac{r^2}{2\eta_0}\left(\left|E_\theta\right|^2 + \left|E_\phi\right|^2\right)\big|_{\theta=\theta_{MAX}}}{P_r / 4\pi} \tag{2.15}$$

Where $\eta_0 = 120\pi$, E_θ and E_ϕ have been expressed in equations 2.12 and 2.13 and P_r is the radiated power, which can be obtained by equation 2.16 for a microstrip antenna over an infinite ground plane [13]:

$$P_r = \frac{1}{2\eta_0}\int_0^{2\pi}\int_0^{\pi/2}(|E_\theta|^2 + |E_\phi|^2)r^2 \sin\theta d\theta d\phi \qquad (2.16)$$

Table 2.3 gives the directivity of the circular patch antenna, for some modes, in terms of different relative dielectric constants, at the frequency of 10GHz over an infinite ground plane.

Mode	ε_r =2.2	ε_r =1.25	ε_r =1.21	ε_r =1.15
TM_{11}	6.827	7.964	8.039	8.158
TM_{21}	5.095	5.49	5.535	5.65
TM_{31}	6.18	5.369	5.437	5.534

Table 2.3 Directivity of circular patch antenna over infinite ground plane,

$h = 1.5mm$ and f=10GHz.

As listed in Table 2.3, the directivity increases by decreasing dielectric constant for all modes, while for a given ε_r, the fundamental mode has the highest directivity.

2.3 Phase Centre

Based on IEEE standard 145-1993, the term of "phase Centre" is defined as "the location of a point associated with an antenna such that, if it is taken as the center of a sphere whose radius extends into the far-field, the phase of a given field component over the surface of the radiation sphere is essentially constant, at least over that portion of the surface where the radiation is significant" [18].

In this thesis, we have studied the phase centre of circular microstrip patch antennas, operating at its dominant mode and higher order modes. As mentioned earlier, such an antenna generates a broadside radiation pattern when operating at its fundamental mode, while it has a null at broadside when it operates at the higher order modes. For each mode, we determine the phase centre of the antenna at a given plane around its main beam, unless otherwise specified.

If a circular microstrip patch antenna operates at a single mode, whether the dominant or a higher order mode, its phase centre will coincident with the physical center of the antenna. However, if two or more modes are excited, the phase centre location may change and the entire antenna may not have a unique phase centre. Instead there may be a locus of the phase centre.

Figures 2.6 and 2.7 show the magnitude and phase of the copolar patterns in the E-plane, for the dominant mode of the disk antenna, when it is located at the coordinate origin, over an infinite ground plane, with ε_r=1.15 and $h = 1.5mm$, at f=10GHz. As can be seen, the phase of E-plane patterns is constant over all observation angles, which means the antenna phase centre is at its physical center.

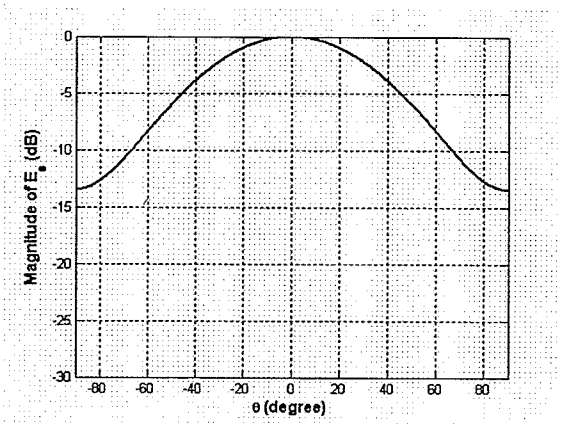

Fig. 2.6 Magnitude of E-plane pattern at ϕ=0 plane for TM_{11} mode over an infinite ground plane, $\varepsilon_r = 1.15$ and $h = 1.5mm$, f=10GHz.

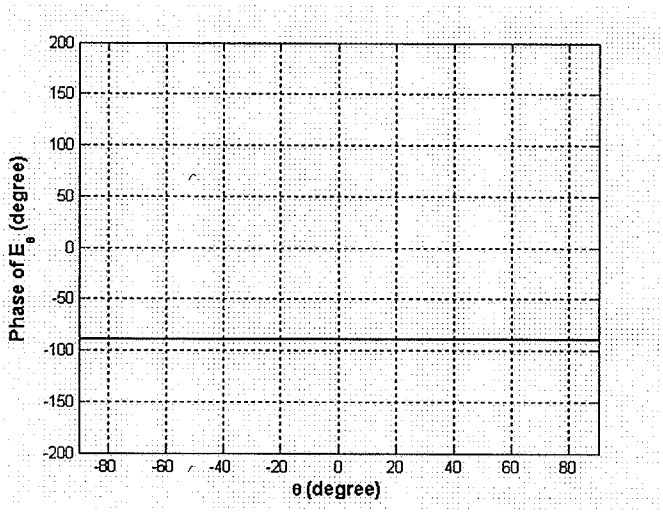

Fig. 2.7 Phase of E-plane pattern at ϕ=0 plane for TM_{11} mode when the antenna is located at the coordinate origin, data same as Fig. 2.6.

Figures 2.8 and 2.9 show the magnitude and phase of the E-plane pattern for the TM_{21} mode of a disk antenna, located at the coordinate origin, having the same parameters as Fig. 2.6. This mode produces a boresight-nulled radiation pattern and the phase around each beam is constant leading again to a phase centre at the physical center of the antenna. This conclusion may be in conflict with the IEEE definition, because there is a

jump in the phase value at the origin. But as mentioned in the IEEE definition, this depends which beam is considered, the right or the left beam, the phase around that beam is constant.

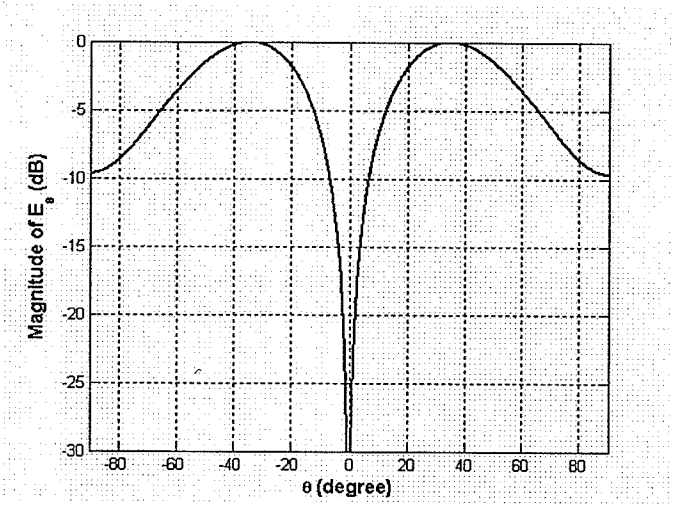

Fig. 2.8 Magnitude of E-plane pattern at ϕ=0 plane for TM_{21} mode, data same as Fig. 2.6.

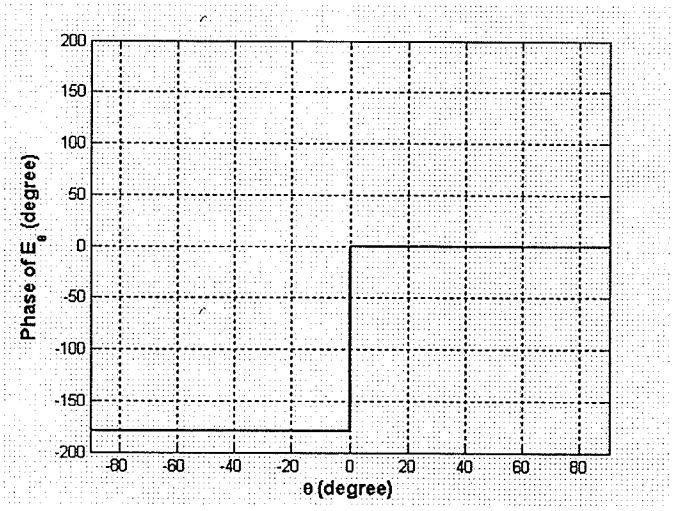

Fig. 2.9 Phase of E-plane pattern at ϕ=0 plane for TM_{21} mode when the antenna is located at the coordinate origin, data same as Fig. 2.6.

Based on equations 2.12 and 2.13, the far field phase is mainly described by the following term,

$$\Phi = k_0 r_0 \sin\theta \cos(\phi - \phi_0) = 2\pi \frac{r_o}{\lambda_0} \sin\theta \cos(\phi - \phi_0) \qquad (2.17)$$

Thus, when we have two or more modes, it should be possible to obtain a constant phase distribution around the main beam, by changing the location of the antenna to the (r_0, ϕ_0), assuming the antenna has been placed on the x-y plane. Thus, the coordinates of the center of the antenna will be given by r_o and ϕ_0, as in Fig. 2.2.

2.4 Proposed study

By employing a multilayer structure and using probe feeds, we have investigated the phase centre location, the tilted main beam and the copolarization and crosspolarization properties of the circular microstrip patch antenna for the following three cases:

i. A two-layer circular microstrip patch antenna operating at the TM_{11} and TM_{21} modes (TM_{11} on top layer , TM_{21} on middle layer, and ground plane in the bottom layer)

ii. A two-layer circular microstrip patch antenna operating at the TM_{11} and TM_{02} modes (TM_{11} on top layer , TM_{02} on middle layer, and ground plane in the bottom layer)

iii. A three-layer circular microstrip patch antenna operating at the TM_{11}, TM_{21} and TM_{02} modes (TM_{11} on top layer , TM_{21} on middle layer, TM_{02} on middle layer, and ground plane in the bottom layer)

As each patch has been excited through an individual probe feed, one can change the magnitude and phase of each port, in order to control the main beam direction and phase, thus the phase centre location of the antenna. Adding the TM_{02} mode, which has an omnidirectional pattern in the azimuth, to the TM_{11} and TM_{21} modes, provides an option to reduce the crosspolarization of the antenna as well. To clarify this idea, surface current distributions for a disk antenna are shown in Fig. 2.10 [19], for mode indices from zero to three. Since $n = 0$ case has a circular symmetry, by adding a proper amount of this mode to the TM_{11} and TM_{21} modes, one may make the direction of current distribution constant, resulting in a lower crosspolarization.

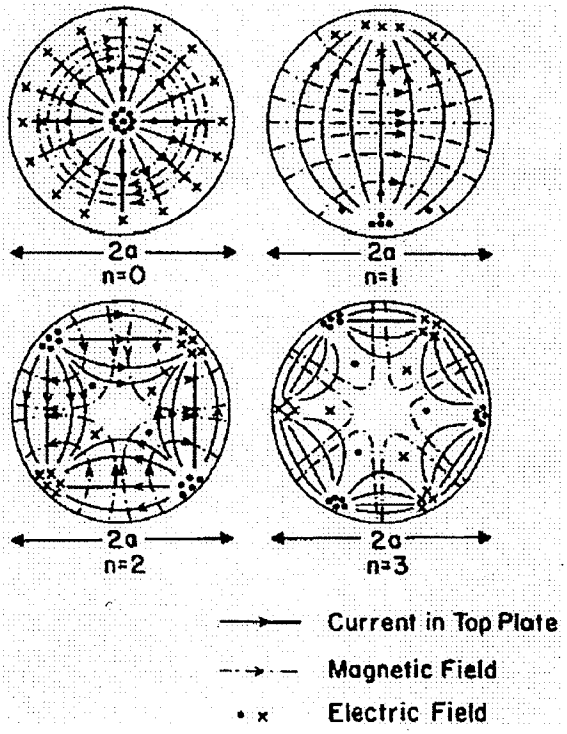

Fig. 2.10 Fields and surface current distributions for various modes (n=0,1,2,3, m=1) [19]

2.5 Summary

In this chapter, a brief background theory on the circular microstrip patch antenna was introduced for both fundamental and higher order modes, including the radiation properties, resonant frequency, feed location and directivity. Then, the antenna phase centre was defined based on the IEEE standard definition, and it was extended for the applications in microstrip antennas. Finally, the proposed concept was explained, in which by varying the excitation amplitude and phase of each mode, one could control the phase centre location, main beam tilt angle and the crosspolarization properties.

Chapter 3

Stacked Patch Circular Microstrip Antenna operating at TM_{11} and TM_{21} modes

3.1 Introduction

In this chapter, a two-layer circular microstrip patch antenna is studied, when the lower patch generates the TM_{21} mode, which has a boresight-nulled radiation pattern, and the upper patch produces the TM_{11} mode which has a broadside radiation pattern. This structure is first treated analytically to better understand the problem in which the ground plane of the antenna is assumed to be infinite in size and the mutual coupling between the two ports is neglected for simplicity. The analysis is based on the cavity model. In order to verify the results, the same structure with a finite ground plane has been simulated by Ansoft Designer version 2, which uses a Method of Moment. Two cases are presented in this chapter, when both patches are fed along the x-axis or placed 45° apart from each other. For each case, the phase centre location, main beam tilt angle and crosspolarization properties are studied in terms of the amplitude ratio and phase difference between the two modes. It will be shown that, the phase centre location is perpendicular to the antenna polarization direction, when two patches are placed 45° apart.

3.2 Case I, both patches are fed along X-axis

3.2.1 Analytical model

3.2.1.1 Radiation amplitude and phase patterns

In this section, we develop a Matlab program to calculate the far field radiation patterns based on the cavity model which was formulated in chapter 2. Thus, the entire antenna is over an infinite ground plane and the mutual coupling between its two ports has been neglected. If they are fed through coaxial probes, these probes may shift the excitation phase. Therefore, the probe effects have been neglected as well to simplify the problem. However, in the numerical simulations, conducted later, these effects are automatically included. Both patches are fed along the x-axis as shown in Fig. 3.1.

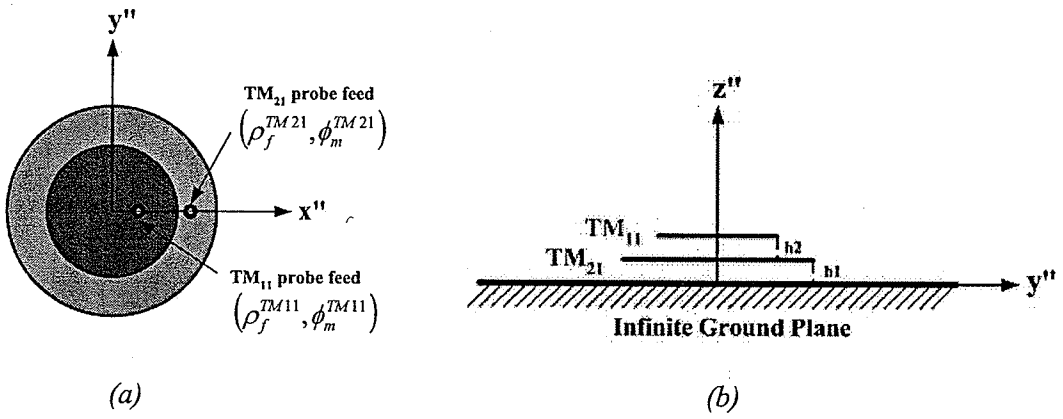

Fig. 3.1 (a) Top view (b) cross-section view of a stacked patch microstrip antenna operating at TM_{11} and TM_{21} modes over an infinite ground plane, when both patches are fed along x-direction $\varepsilon_r = 1.15,\ h_1 = h_2 = 1.5mm,\ a_{TM11} = 6.8mm, a_{TM21} = 12.42mm$, *f=10GHz.*

The antenna was designed to resonate at 10GHz. The patch sizes were determined using equations 2.8 to 2.11, where the eigenvalues for the TM_{11} and TM_{21} modes are 1.841 and 3.054, respectively. Both layers have the same thickness of 1.5mm, and

ε_r=1.15. As discussed in section 2.2.2, due to the small dielectric thickness of each patch, the effect of h_1 and h_2 on the phase distribution can be ignored. Thus, for the TM_{11} and TM_{21} modes, using equations 2.12 ,2.13 and 2.14, the far field in spherical coordinates, with the coordinates of the patch centers at $(r_o, \phi_0, 0)$ according to Fig. 2.2, can be expressed as,

TM_{11} Mode ($\phi_m = 0$):

$$E_\theta = -jC_1 \frac{e^{-jk_0 r}}{r} e^{jk_0 r_o \sin\theta\cos(\phi-\phi_0)} \left[J_0(k_0 a_1 \sin\theta) - J_2(k_0 a_1 \sin\theta)\right]\cos\phi \qquad (3.1)$$

$$E_\phi = jC_1 \frac{e^{-jk_0 r}}{r} e^{jk_0 r_o \sin\theta\cos(\phi-\phi_0)} \left[J_0(k_0 a_1 \sin\theta) + J_2(k_0 a_1 \sin\theta)\right]\cos\theta\sin\phi \qquad (3.2)$$

TM_{21} Mode ($\phi_m = 0$):

$$E_\theta = +C_2 \frac{e^{-jk_0 r}}{r} e^{jk_0 r_o \sin\theta\cos(\phi-\phi_0)} \left[J_1(k_0 a_2 \sin\theta) - J_3(k_0 a_2 \sin\theta)\right]\cos 2\phi \qquad (3.3)$$

$$E_\phi = -C_2 \frac{e^{-jk_0 r}}{r} e^{jk_0 r_o \sin\theta\cos(\phi-\phi_0)} \left[J_1(k_0 a_2 \sin\theta) + J_3(k_0 a_2 \sin\theta)\right]\cos\theta\sin 2\phi \qquad (3.4)$$

Where a_1 and a_2 are the radii of the patches for the TM_{11} and TM_{21} modes, respectively, and $(r_0, \phi_0, 0)$ are the coordinates of the antenna center (two patches are concentric).

The combined far fields are:

$$E_\theta = -jC_1 e^{jk_0 r_o \sin\theta\cos(\phi-\phi_0)} \left\{ \left[J_0(u_1) - J_2(u_1)\right]\cos\phi + j\frac{C_2}{C_1}\left[J_1(u_2) - J_3(u_2)\right]\cos 2\phi \right\} \frac{e^{-jk_0 r}}{r} \qquad (3.5)$$

$$E_\phi = jC_1 e^{jk_0 r_o \sin\theta\cos(\phi-\phi_0)} \left\{ \left[J_0(u_1) + J_2(u_1)\right]\sin\phi + j\frac{C_2}{C_1}\left[J_1(u_2) + J_3(u_2)\right]\sin 2\phi \right\} \cos\theta \frac{e^{-jk_0 r}}{r} \qquad (3.6)$$

Where $\left.\begin{matrix} u_1 = k_0 a_1 \sin\theta \\ u_2 = k_0 a_2 \sin\theta \end{matrix}\right\}$ and $\frac{C_2}{C_1}$ is the excitation ratio (TM_{21} to TM_{11}) and it is a complex number in general, $C_1 = |C_1| \angle \alpha_1$ and $C_2 = |C_2| \angle \alpha_2$.

In ϕ=0 plane, the E_θ pattern is the contribution of both TM_{11} and TM_{21} modes, while the E_ϕ is zero. Therefore, we have considered the E_θ for this case. Now, by changing the excitation ratio $\frac{C_2}{C_1}$ (both magnitude and phase) we can change the main beam direction and phase centre location. Figures 3.2 and 3.3 show the magnitude and phase of the E_θ at ϕ=0 plane, respectively, when the excitation ratio is in-phase, i.e. $\alpha_1 - \alpha_2 = 0$, and the antenna is located at the coordinate origin. It illustrates that, by increasing the absolute value of the excitation ratio, the peak radiation direction moves toward the main beam direction of the pure TM_{21} mode and the phase pattern becomes that of the pure TM_{21}. It also shows that for the in-phase excitations, phase patterns for non-zero excitation ratios are no longer constant, which imply that, the location of the antenna phase centre has been changed. In order to have a constant phase distribution around the main beam, we must add a negative-slope phase term to the initial phase pattern.

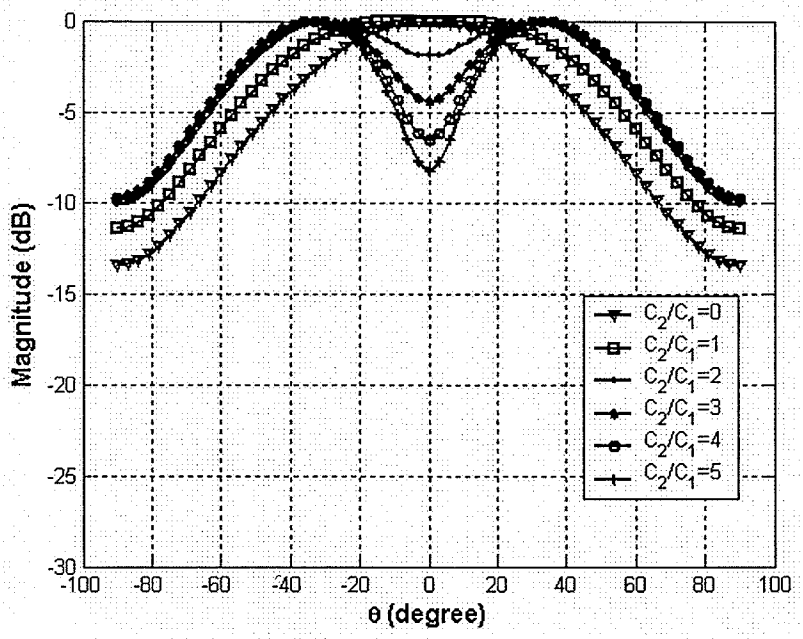

Fig. 3.2 Magnitude patterns of E_θ for combined TM_{11} and TM_{21} modes at ϕ=0 plane for different in-phase, $\alpha_1=\alpha_2$, amplitude ratios for the antenna shown in Fig. 3.1, when it is located at the origin and both patches are fed along x-axis.

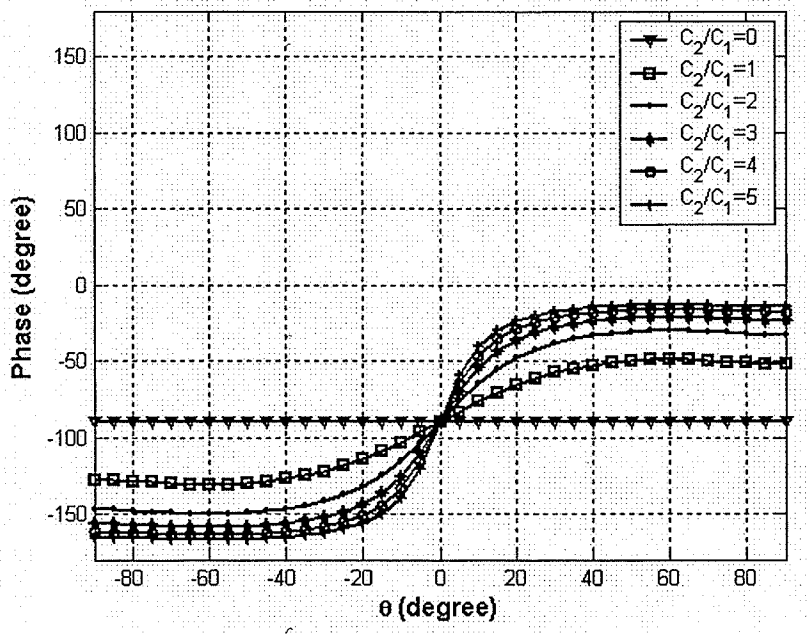

Fig. 3.3 Phase patterns of E_θ at ϕ=0 plane for different in-phase amplitude ratios for the antenna shown in Fig. 3.1, when it is located at the origin and both patches are fed along x-axis.

Now, let us consider the out of phase excitations, $|\alpha_1 - \alpha_2| \leq 90^o$, of these two modes by assuming that α_1 and α_2 are the excitation phase for TM_{11} and TM_{21} modes, respectively. As shown in Fig. 3.2, for non-zero and in-phase excitations, there is a symmetric radiation pattern with two peaks, one at ϕ=0 side and the other at ϕ=180° side (in the above figures, they have been illustrated by positive θ and negative θ, respectively). The out of phase excitation makes the radiation pattern to have only one peak, which depends on the sign of the phase difference in such a way that for positive $\alpha_1 - \alpha_2$, the main beam moves to positive θ, or ϕ=0 side, and for negative $\alpha_1 - \alpha_2$, the main beam moves to negative θ, or ϕ=180° side.

Figures 3.4 to 3.7 show the magnitude and phase of the E-plane patterns at ϕ=0 plane, when the two modes have an out of phase excitation, but equal amplitude, while the antennas are located at the coordinate origin. It is important to note that a quadrature phase difference, $|\alpha_1 - \alpha_2| = 90^o$, makes the far field phase pattern flat over the entire observation angle range, which in turn pushes the phase centre location to the center of the antenna. The reason is that, a 90° phase shift neutralizes the effect of j coefficient for the TM_{11} mode, as shown in equations 3.1 and 3.2. More details on phase centre location and the main beam tilt angle will be discussed in the next section.

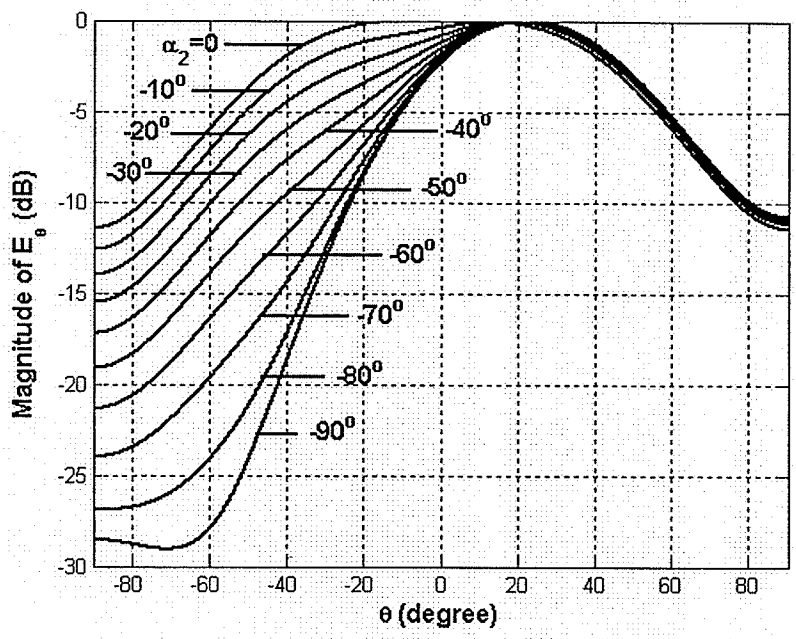

Fig. 3.4 Magnitude patterns of E_θ for combined TM_{11} and TM_{21} modes at $\phi = 0$ plane for different negative values of α_2 phase excitations, $\alpha_1 = 0$ and $|C_1| = |C_2| = 1$ for the antenna shown in Fig. 3.1, when it is located at the origin and both patches are fed along x-axis.

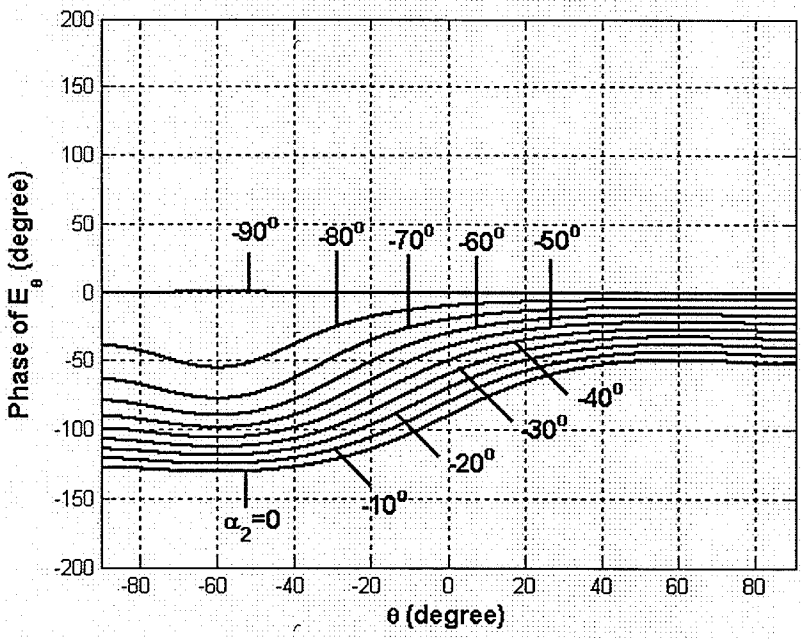

Fig. 3.5 Phase patterns of E_θ at $\phi = 0$ plane for different negative values of α_2 phase excitations, $\alpha_1 = 0$ and $|C_1| = |C_2| = 1$ for the antenna shown in Fig. 3.1, when it is located at the origin and both patches are fed along x-axis.

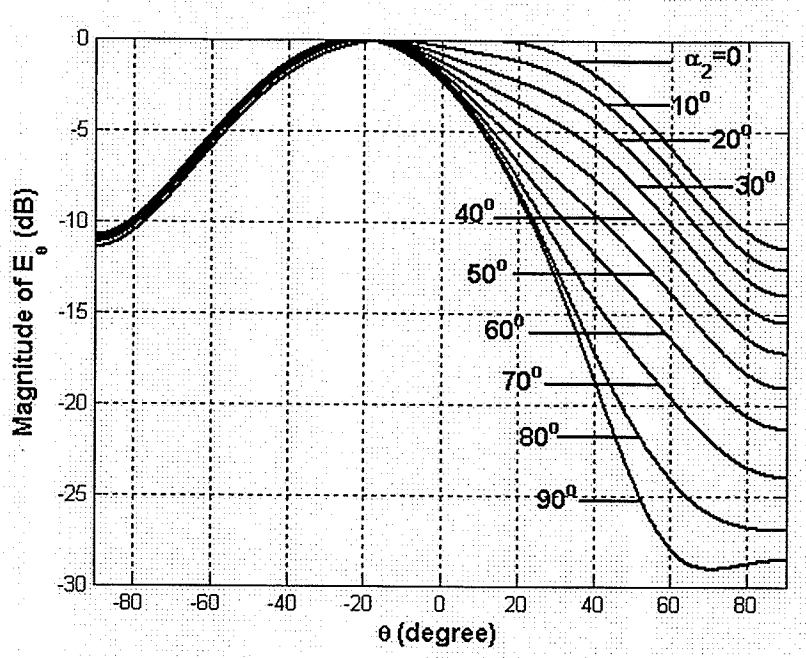

Fig. 3.6 Magnitude patterns of E_θ for combined TM_{11} and TM_{21} modes at $\phi = 0$ plane for different positive values of α_2 phase excitation, $\alpha_1 = 0$ and $|C_1| = |C_2| = 1$ for the antenna shown in Fig. 3.1, when it is located at the origin and both patches are fed along x-axis.

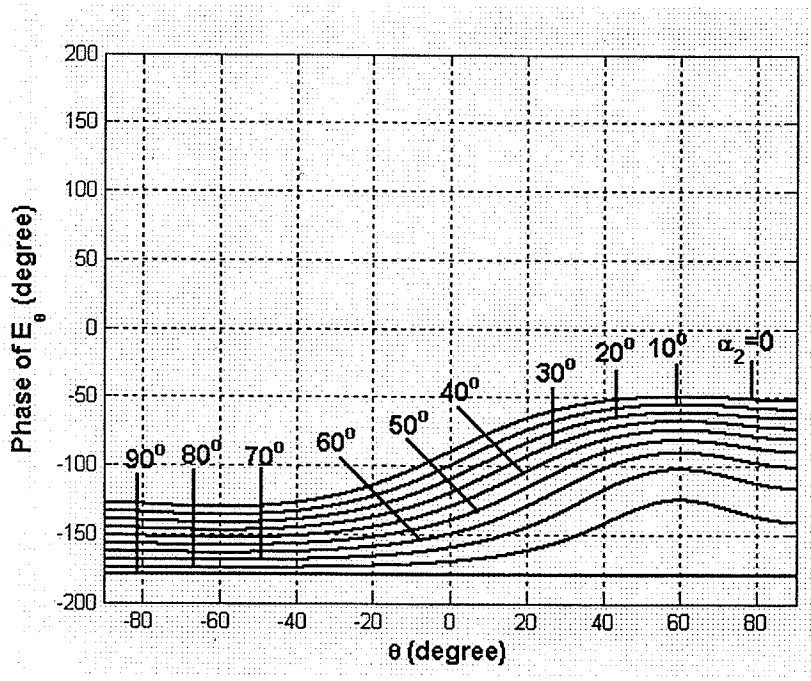

Fig. 3.7 Phase patterns of E_θ at $\phi = 0$ plane for different positive values of α_2 phase excitations, $\alpha_1 = 0$ and $|C_1| = |C_2| = 1$ for the antenna shown in Fig. 3.1, when it is located at the origin and both patches are fed along x-axis.

3.2.1.2 Phase centre location and main beam tilt angle

As shown in the preceding section, by adding the TM_{21} mode to the dominant mode, which has a constant phase pattern, the far-field phase patterns change over the angles of the main beam axis, and are not constant, except with a quadrature phase excitation. This means, the signals are not emanating from the center of the antenna or, in other words, the antenna phase centre has moved. In order to find the new phase centre location, one may displace the antenna from the coordinate origin, so that a new phase term can be introduced to the antenna function, which will be dependent on the displacement. Enforcing the constant phase values over the main beam will allow determination of the displacement coordinates, (r_0, ϕ_0). For all non-zero amplitude excitations and phase differences less than 90 degrees, the slope of the phase patterns are positive versus the angle off axis θ, implying that one should add negative slope to the phase pattern to obtain a constant phase. As discussed earlier, the term $e^{jk_0 r_0 \sin\theta\cos(\phi-\phi_0)}$ accounts for the phase shift due to the displacement, which depends on the location of the antenna (r_0, ϕ_0). For a given ϕ_0, there is a unique r_0 that can make the phase distribution constant. Therefore, there will be a locus for the phase centre of the antenna instead of a single point. This is because of the fact that the slope of the additive phase due to the antenna displacement is basically governed by the term $2\pi\frac{r_o}{\lambda_0}\cos(\phi-\phi_0)$, which needs to be constant with opposite sign of the initial phase pattern's slope over the range of interest.

$$2\pi\frac{r_0}{\lambda_0}\cos(\phi-\phi_0) = -constant \Rightarrow \quad \frac{r_0}{\lambda_0}\cos(\phi-\phi_0) = -K \quad (3.7)$$

Thus, for a given ϕ, the locus of the phase centre, in the cylindrical coordinates, will be a line perpendicular to the ϕ-direction in the x-y plane, passing through the point $(r_0, \phi_0 = \phi + \pi)$.

As an example, let us consider the case with in-phase, $\alpha_1 = \alpha_2$, and equal amplitude excitation. The phase centre of the E_θ pattern of the antenna is located on the solid line shown in Fig. 3.8 while it is passing though the point $(r_0 = 0.21\lambda, \phi_0 = \pi)$.

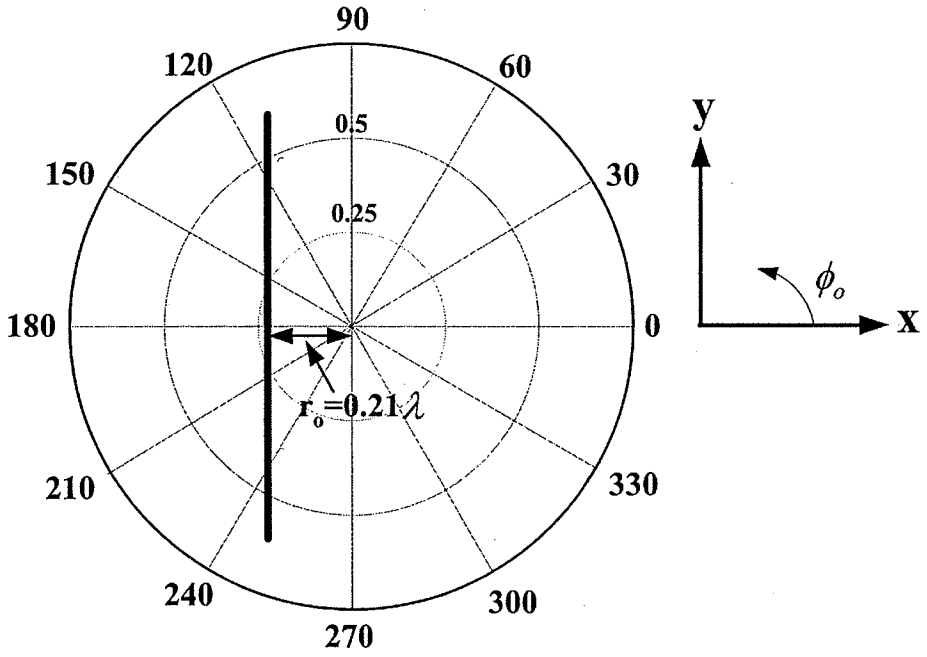

Fig. 3.8 The locus of phase centre of the E-plane patterns of the antenna shown in Fig. 3.1, for equal amplitude and in-phase excitation $\alpha_1 = \alpha_2$, when both patches are fed along x-axis.

In this section, the results for phase centre location of the E-plane patterns are presented. The effects of amplitude excitation ratio on the phase centre location and main beam tilt angle are shown in Fig. 3.9 and 3.10, respectively, for different excitation phases. As can be seen, for all excitation phases, except $\alpha_1 - \alpha_2 = \pm 90^o$ that keeps the

phase centre at the coordinate origin, the phase centre moves from the center. The distance of the phase centre from origin increases until the mode amplitude ratio C_2/C_1 of unity, beyond which it decreases. That is, the phase centre moves back to origin as the amplitude of TM_{21} mode increases, and in the limit of pure TM_{21} mode, it returns to the coordinate origin. The main beam tilt also moves toward the TM_{21} mode peak. It is interesting to note that, for the in-phase excitation, $\alpha_1 = \alpha_2$, with amplitude ratio C_2/C_1 up to unity, the main beam remains at the boresight angle, while the antenna phase centre moves away from the antenna physical center leading to the virtual antenna concept.

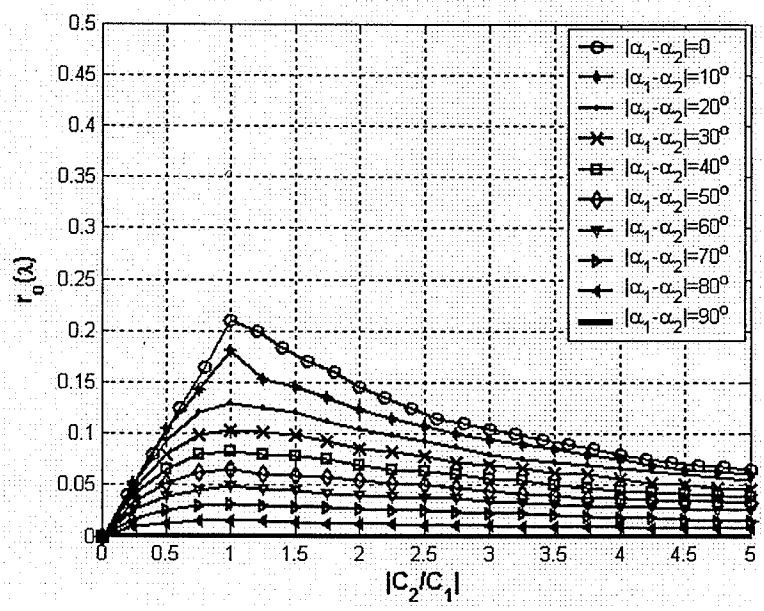

Fig. 3.9 Effect of $\left|\frac{C_2}{C_1}\right|$ *on phase centre location of* E_θ *at* $\phi = 0^\circ$ *plane for different excitation phases over main beam, for the antenna shown in Fig. 3.1, when both patches are fed along x-axis while* $\phi_0 = 180^\circ$.

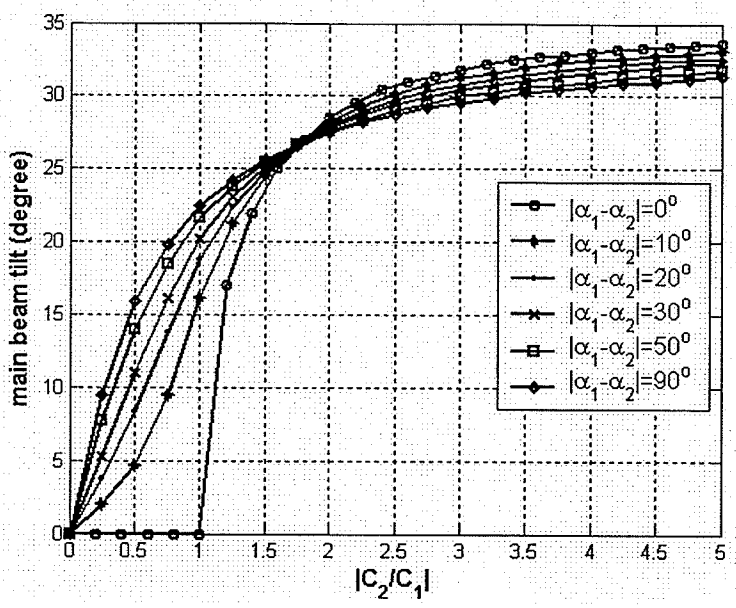

Fig. 3.10 Effect of $\left|\frac{C_2}{C_1}\right|$ *on main beam tilt angle for* E_θ *at* $\phi = 0^o$ *plane for different excitation phases of the antenna shown in Fig. 3.1, when both patches are fed along x-axis while* $\phi_0 = 180^o$.

The effects of the excitation phase difference on the phase centre location and main beam tilt angle were also studied, which are shown in Fig 3.11 and 3.12, respectively, for certain selected amplitude excitation ratios. They show that, the phase centre converges to the center of the antenna for the quadrature phase difference, $|\alpha_1 - \alpha_2| = 90^o$. The main beam direction remains almost constant, over all excitation phases, when the amplitude ratio exceeds two, $C_2/C_1 \geq 2$, while the phase centre location changes. This is due the fact that, at higher amplitude ratios, the TM_{21} mode has more profound impact on the antenna function. For $C_2/C_1 \leq 1$ and $\alpha_1 = \alpha_2$, all main beams are along the boresight, and the peak radiation direction moves away from the boresight as the excitation phases increase.

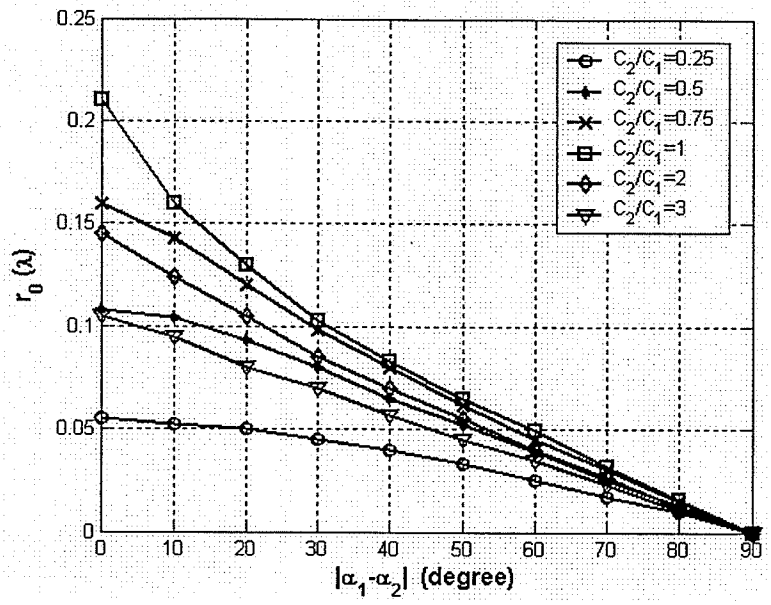

Fig. 3.11 Phase centre location of E_θ at $\phi = 0$ plane versus excitation phases for different $\left|\frac{C_2}{C_1}\right|$, over main beam, for the antenna shown in Fig. 3.1, when both patches are fed along x-axis while $\phi_0 = 180^o$.

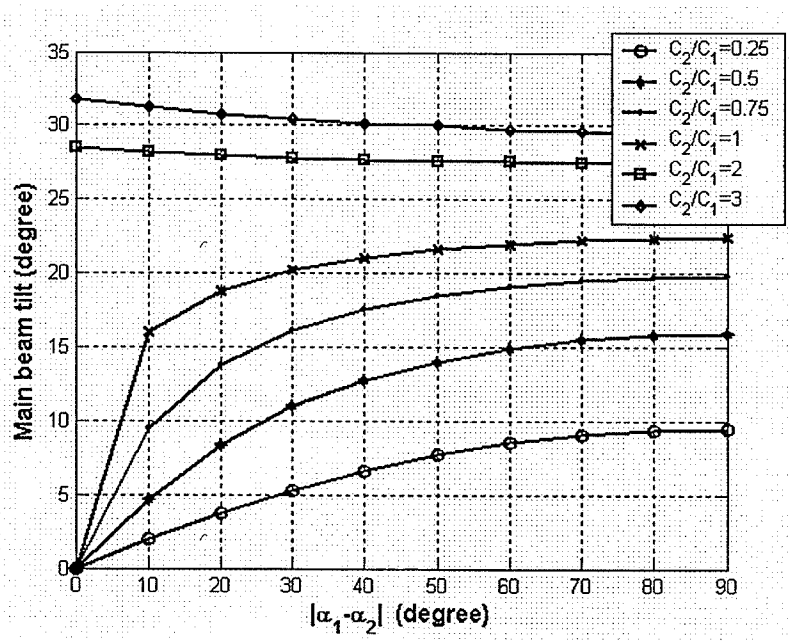

Fig. 3.12 Main beam tilt angle of E_θ at $\phi = 0$ plane versus excitation phases for different $\left|\frac{C_2}{C_1}\right|$, for the antenna shown in Fig. 3.1, when both patches are fed along x-axis while $\phi_0 = 180^o$.

3.2.1.3 Polarization properties

The polarization of a radiated wave at a single frequency describes the shape and orientation of the locus of the extremities of the electric field vector as a function of time [9]. The polarization of a wave may be linear, circular or elliptical. In this thesis, we are dealing with linearly polarized wave. The field with linear polarization is described by copolar and crosspolar components. Based on Ludwig's third definition [20], the copolar and crosspolar components of the electric field of an x-polarized wave are defined as:

$$\begin{Bmatrix} E_{co}(\theta,\phi) = \cos\phi E_\theta - \sin\phi E_\phi \\ E_X(\theta,\phi) = \sin\phi E_\theta + \cos\phi E_\phi \end{Bmatrix} \tag{3.8}$$

If the electric field is aligned along the y-direction, we have:

$$\begin{Bmatrix} E_{co}(\theta,\phi) = \sin\phi E_\theta + \cos\phi E_\phi \\ E_X(\theta,\phi) = \cos\phi E_\theta - \sin\phi E_\phi \end{Bmatrix} \tag{3.9}$$

The antenna under study in this section, which is operating at the TM_{11} and TM_{21} modes, when both patches are fed along the x-direction, generates an x-polarized field. Its copolar and crosspolar patterns can then be found using equation 3.8, where E_θ and E_ϕ are already expressed by equations 3.5 and 3.6.

As shown in the previous section, the phase centre of E_θ at $\phi = 0^o$ plane is a line as discussed before. Generally, microstrip antennas have asymmetric E- and H-plane radiation patterns, which cause different phase centre locations at different ϕ-planes. In order to find a global phase centre, the copolar radiation pattern may be considered. To clarify how the phase centre of copolar radiation pattern will be independent of ϕ, an example of equal amplitude ratio, $C_2/C_1=1$, and in-phase excitation, $\alpha_1=\alpha_2$ is considered

for the antenna shown in Fig. 3.1. The phase patterns of copolar radiation pattern, at different ϕ-planes, are shown in Figs. 3.13 and 3.14, when the antenna is located at the coordinate origin and at the point (r_o=0.21λ, ϕ_o=180°), respectively. As shown in Fig. 3.14, the phase patterns are constant around the boresight angle for all ϕ-planes. This means that, the point (r_o=0.21λ, ϕ_o=180°) is a global phase centre.

The effect of amplitude excitation ratio on the phase centre location of the copolar radiation pattern is shown in Fig. 3.15, when the antenna works at the TM_{11} and TM_{21} modes and both patches are fed along the x-axis, as shown in Fig. 3.1. These phase centre locations are found to be global for any excitation phase and amplitude ratio less than unity, at all ϕ-planes. For excitation amplitude ratios more than unity, there will be multiple phase centres, since the peak radiation directions of the E- and H-plane patterns will not be the same.

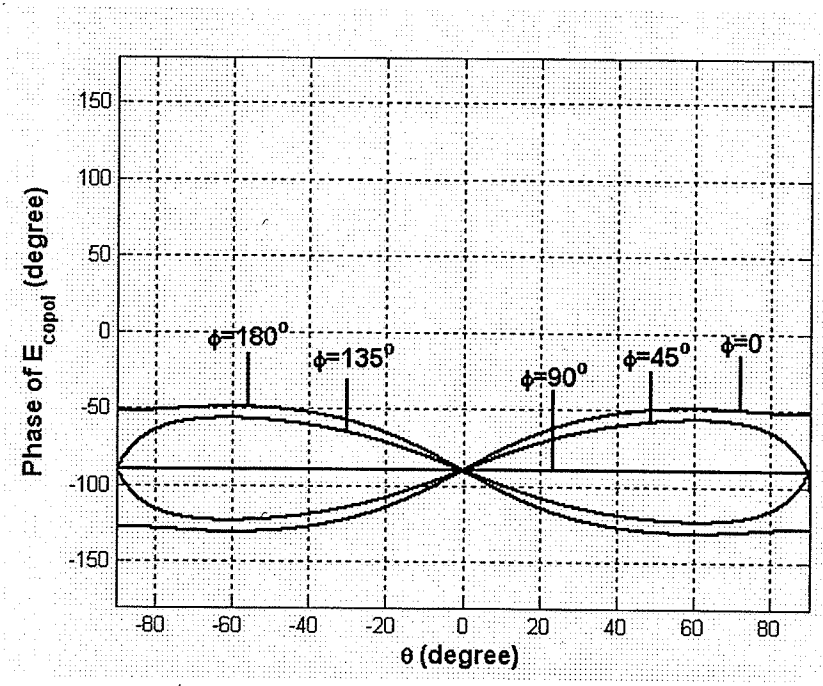

Fig. 3.13 Phase patterns of copolar radiation pattern at different ϕ-planes, when C_2/C_1=1 and $\alpha_1=\alpha_2$ for the antenna shown in Fig. 3.1, when it is located at the origin and both patches are fed along x-axis.

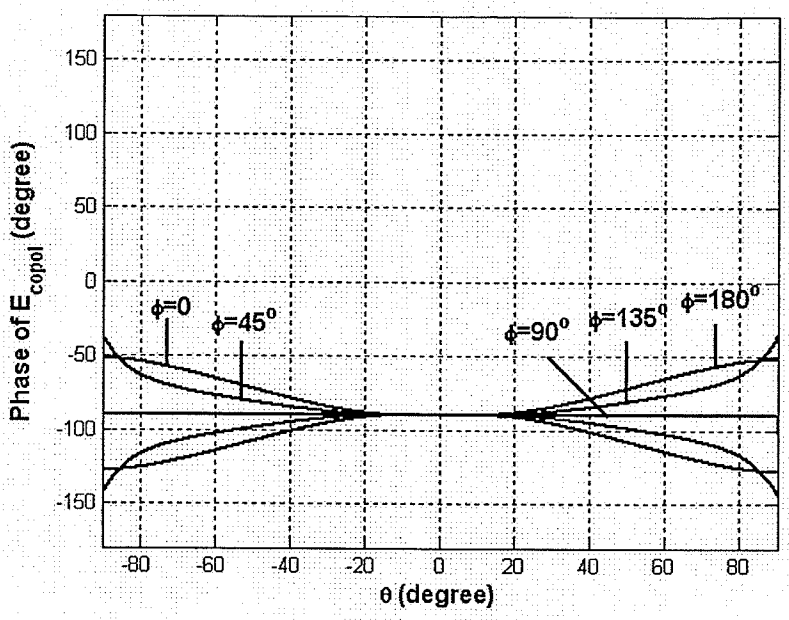

Fig. 3.14 Phase patterns of copolar radiation pattern at different ϕ-planes, when $C_2/C_1=1$ and $\alpha_1=\alpha_2$ for the antenna shown in Fig. 3.1, when both patches are fed along x-axis and the antenna is located at ($r_o=0.21\lambda$, $\phi_o=180^o$).

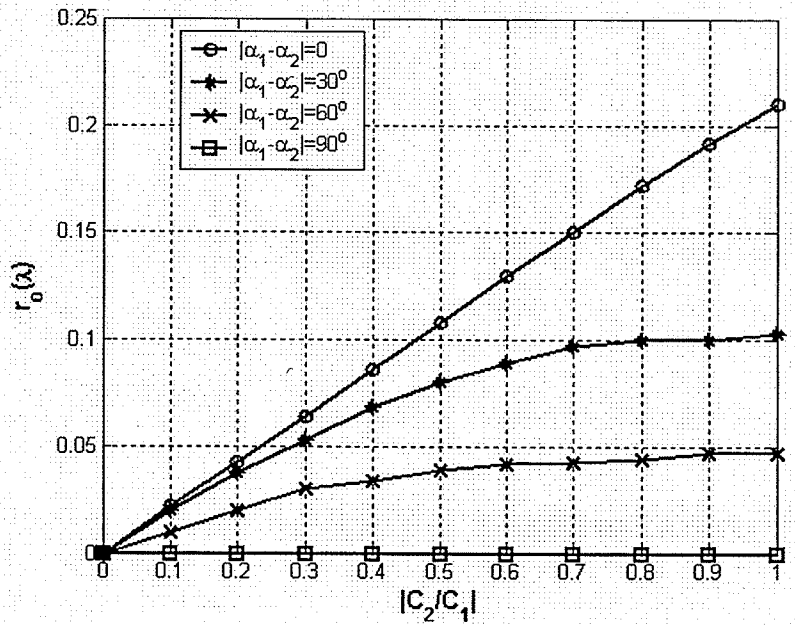

Fig. 3.15 Effect of $\left|\frac{C_2}{C_1}\right|$ on phase centre of copolar radiation pattern of the antenna shown in Fig. 3.1, when $\phi_0 = 180^o$ over main beam.

The copolar and crosspolar patterns at different ϕ-planes are as below:

- At $\phi = 0$ plane:

$$\left\{ \begin{aligned} E_{co}\,|_{\phi=0} &= E_\theta\,|_{\phi=0} \\ E_{xpol}\,|_{\phi=0} &= E_\phi\,|_{\phi=0} = 0 \end{aligned} \right\} \tag{3.10}$$

- At $\phi = 90^o$ plane:

$$\left\{ \begin{aligned} E_{co}\,|_{\phi=90^o} &= -E_\phi\,|_{\phi=90^o} \\ E_{xpol}\,|_{\phi=90^o} &= E_\theta\,|_{\phi=90^o} \end{aligned} \right\} \tag{3.11}$$

- At $\phi = 45^o$ plane:

$$\left\{ \begin{aligned} E_{co}\,|_{\phi=45^o} &= \left(\cos\phi\, E_\theta - \sin\phi\, E_\phi\right)|_{\phi=45^o} \\ E_{xpol}\,|_{\phi=45^o} &= \left(\sin\phi\, E_\theta + \cos\phi\, E_\phi\right)|_{\phi=45^o} \end{aligned} \right\} \tag{3.12}$$

As can be seen, at $\phi = 0$ plane, the crosspolarization is zero since E_ϕ for both modes vanishes on this plane. Figure 3.16 shows the copolar and crosspolar patterns at $\phi = 90^o$ plane for different mode excitation ratios.

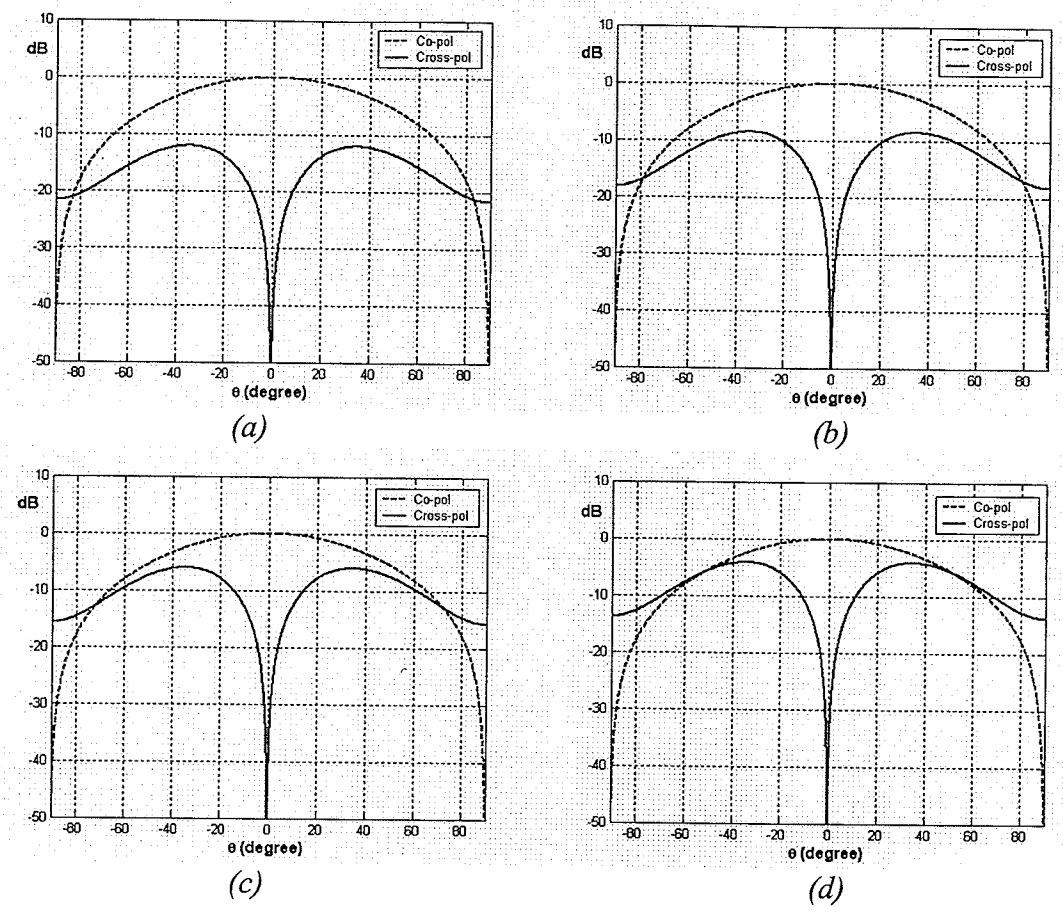

Fig. 3.16 Normalized copolar and crosspolar components at $\phi = 90^o$ plane of the antenna shown in Fig. 3.1, when both patches are fed along x-axis

(a) $\frac{C_2}{C_1} = 0.5\angle 0$, *(b)* $\frac{C_2}{C_1} = 0.75\angle 0$, *(c)* $\frac{C_2}{C_1} = 1\angle 0$, *(d)* $\frac{C_2}{C_1} = 1.25\angle 0$

Crosspolarization at $\phi = 90^o$ plane is mainly due to E_θ of the TM_{21} mode and it increases with higher mode ratio, as illustrated at Fig. 3.16. At $\phi = 45^o$ plane, both TM_{11} and TM_{21} modes contribute to the crosspolarization patterns, as shown in Fig. 3.17. The normalized crosspolar to copolar levels versus excitation amplitude ratio, are plotted in Fig. 3.18 and 3.19 at $\phi = 90^o$ and $\phi = 45^o$ planes, respectively. They show that, at both planes, the crosspolarization is lower for small excitation amplitude ratios, since by

increasing this ratio, the effect of TM_{21} mode increases and crosspolarization level increases.

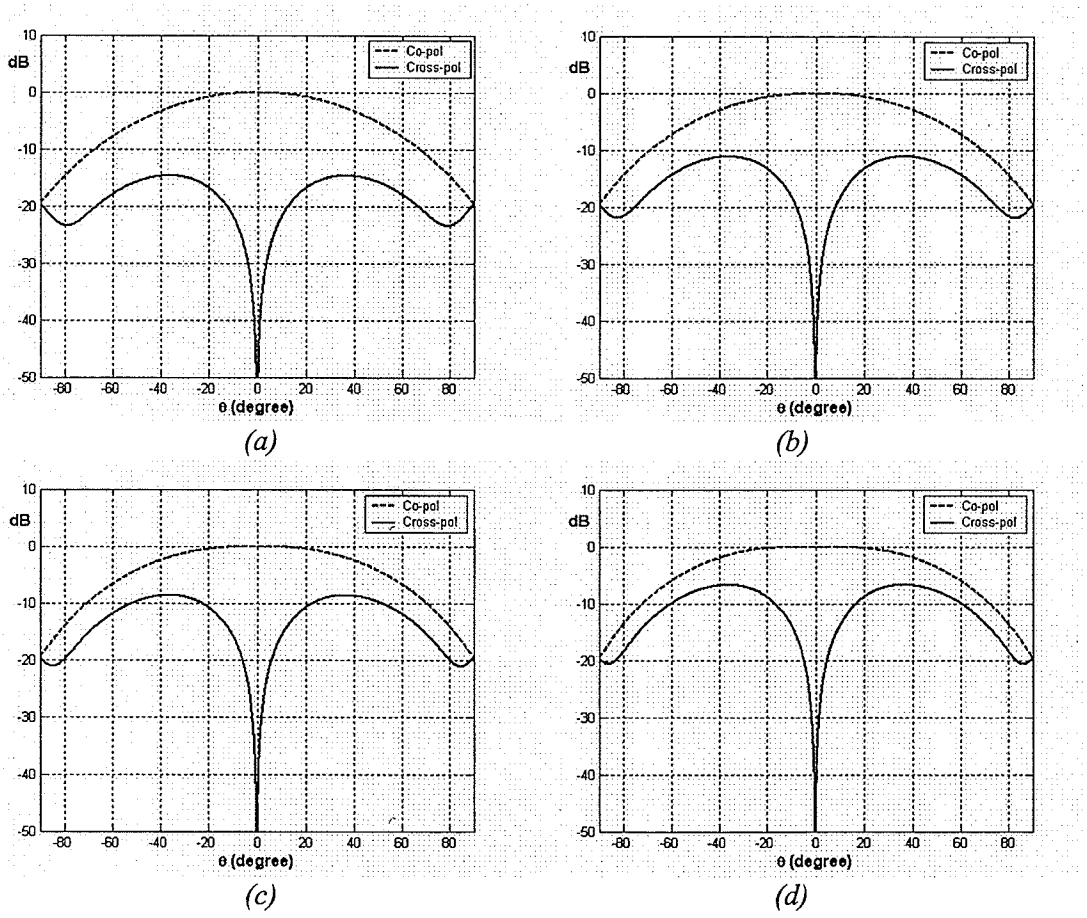

Fig. 3.17 Normalized copolar and crosspolar components at $\phi = 45^{o}$ plane of the antenna shown in Fig. 3.1, when both patches are fed along x-axis

(a) $\frac{C_2}{C_1} = 0.5\angle 0$, *(b)* $\frac{C_2}{C_1} = 0.75\angle 0$, *(c)* $\frac{C_2}{C_1} = 1\angle 0$, *(d)* $\frac{C_2}{C_1} = 1.25\angle 0$

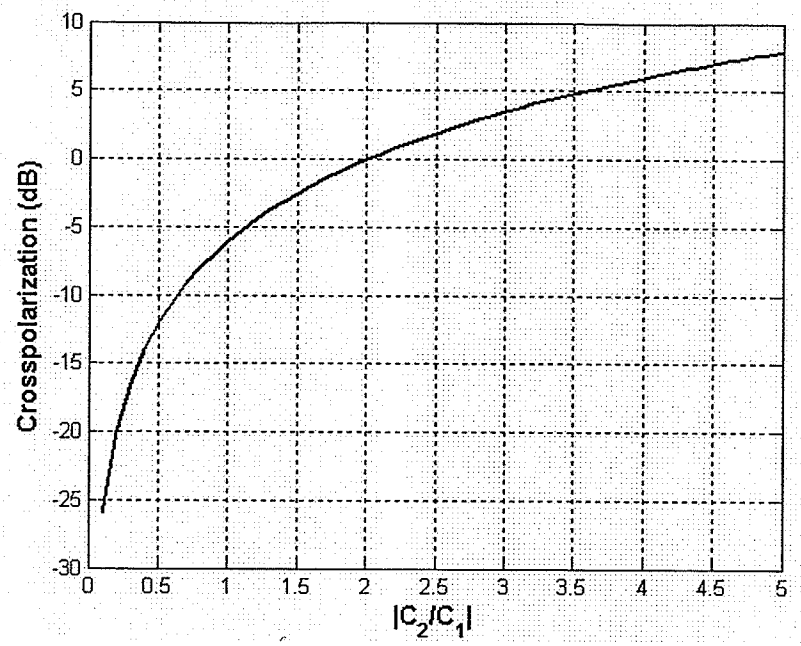

Fig. 3.18 Crosspolarization versus excitation amplitude ratio, $\left|\frac{C_2}{C_1}\right|$, *at* $\phi = 90^\circ$ *plane of the antenna shown in Fig. 3.1, when both patches are fed along x-axis and* $\alpha_1 = \alpha_2$.

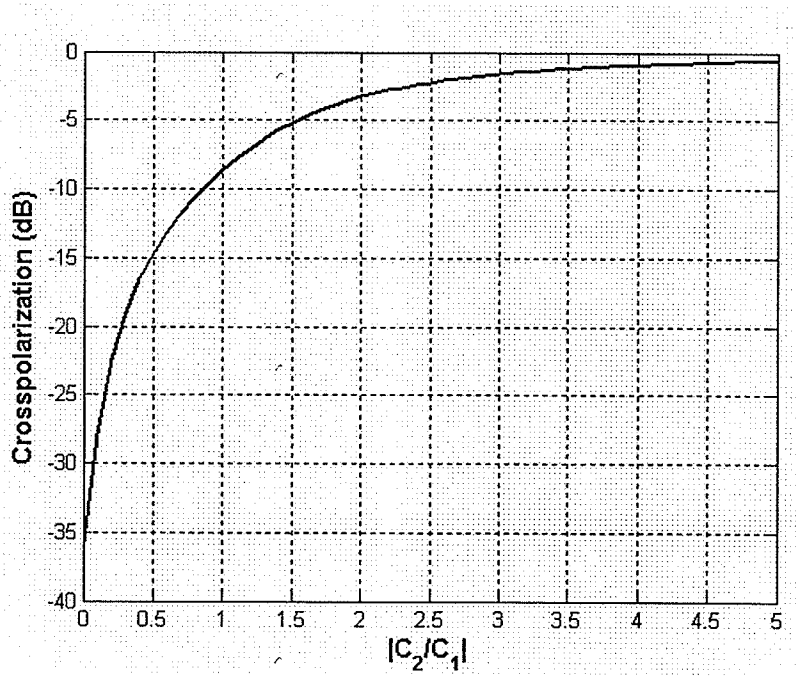

Fig. 3.19 Crosspolarization versus excitation amplitude ratios, $\left|\frac{C_2}{C_1}\right|$, *at* $\phi = 45^\circ$ *plane of the antenna shown in Fig. 3.1, when both patches are fed along x-axis and* $\alpha_1 = \alpha_2$.

3.2.2 Design Example

In order to verify the above analytical results, a two-layer antenna was simulated by Ansoft Designer package version 2 which is based on a Method of Moment. The geometry of the antenna is shown in Fig. 3.20. Since the radius of the patch increases with the mode index number, the upper patch is chosen to operate at the TM_{11} mode, and the middle patch at TM_{21} and the lower patch is a finite ground plane. One type substrate was used for both layers, with $\varepsilon_r = 1.15$. The dielectric thickness for both patches is identical and is equal to 1.5mm. The operating frequency is 10GHz. The finite ground plane was considered, since it can be fabricated practically.

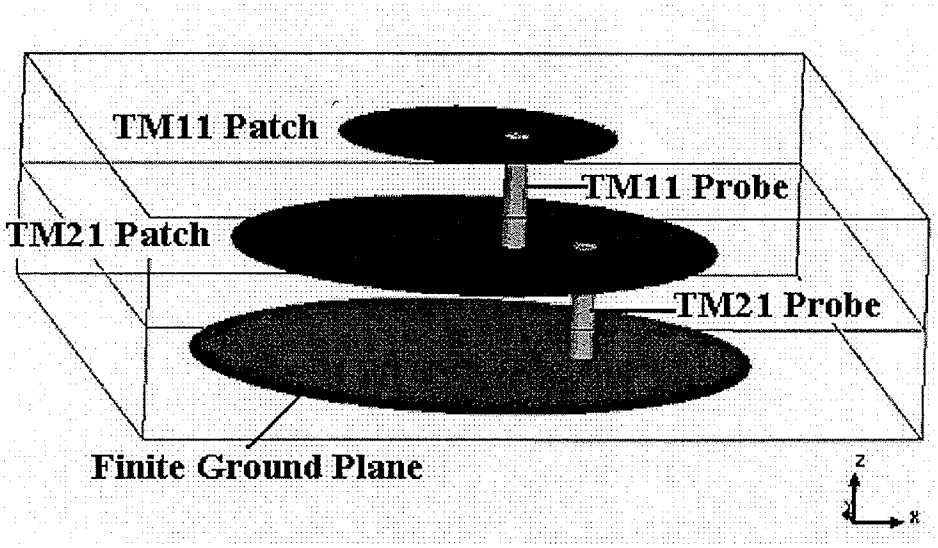

Fig. 3.20 The geometry of stacked patch antenna operating at TM_{11} and TM_{21} modes over a finite ground plane

$$a_{TM11} = 7.485mm,\ a_{TM21} = 13.02mm,\ a_{ground} = 15mm$$

$$\rho_f^{TM11} = 2.12mm,\ \phi_m^{TM11} = 0$$

$$\rho_f^{TM21} = 6mm,\ \phi_m^{TM21} = 0$$

$$h_1 = h_2 = 1.5mm,\ \varepsilon_r = 1.15$$

Two individual probes were used to excite the antenna, one for the TM_{11} mode and the another for TM_{21} mode. The feed location was optimized in order to excite each

mode properly, based on the discussion in chapter 2, section 2.2.3, and to have a good impedance match condition at 10GHz. The scattering parameters of the antenna are shown in Fig. 3.21. As can be seen, the return losses for both ports are well below -10dB at 10GHz, which provide good impedance match, while the coupling between the two ports, is about -24dB at the frequency of operation.

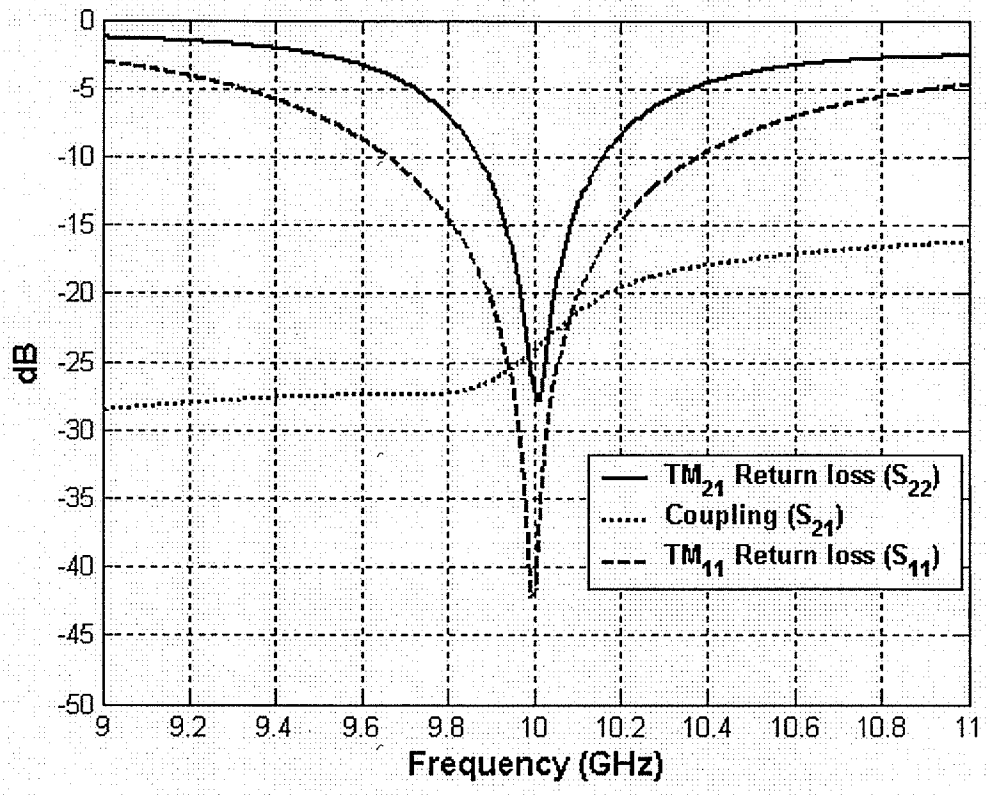

Fig. 3.21 Scattering parameters of stacked patch antenna in Fig. 3.20 operating at TM_{11} and TM_{21} modes over a finite ground plane.

As is known, a probe feed has a reactance and adds phase shift to the input signal. In the present simulations such phase shifts will be automatically included in the results and will alter the required phase shift between the two modes, in investigation of the phase centre locations. In order to compare the current simulation results with previous

analytical ones, in equation 3.5, we must determine the relationship between the mode constants, C_n, and V_n, as well as the phase shift values for each probe.

Based on equation 2.14, $V_n = \frac{2C_n}{a_n k_0}$, thus if $C_1 = C_2$:

$$\frac{V_1}{V_2} = \frac{a_2}{a_1} = \frac{\chi'_{21}}{\chi'_{11}} = \frac{3.054}{1.841} = 1.6589 \quad (3.13)$$

The numerical simulator, Ansoft Designer version 2, can only excite the antenna in currents. Therefore, the above voltages must be converted into currents. If there is a good impedance match condition at each port, one can assume that the input impedance of each port is 50 ohms. Therefore, there will be a linear relationship between voltage and current based on the Ohms law, $V = ZI$. By this assumption, the amplitude of currents for each mode will be $|I_{TM11}| = 82.94mA$, $|I_{TM21}| = 50mA$. Now, we have to choose the proper phase for each mode to cancel the probe introduced phase shift. These values are $\angle I_{TM11} = 45^o$, $\angle I_{TM21} = -90^o$. They were chosen to make the analytical and numerical phase distributions identical as shown in Fig. 3.23 and Fig. 3.26. This means, the identical mode coefficients, C_1=C_2 and $\alpha_1 = \alpha_2$, in the analytical approach correspond to the following current excitations in numerical simulations, as shown in table 3.1:

$$I_{TM11} = 83mA\angle 45^o, I_{TM21} = 50mA\angle -90^o, \Delta\phi = -135^o \quad (3.14)$$

Excitation Ratio	Amplitude	Phase (degrees)
Analytical $(\frac{C_2}{C_1})$	1	0
Numerical $(\frac{I_{TM21}}{I_{TM11}})$	0.6024	-135°

Table 3.1 Relation between excitation ratios C_2/C_1 in analytical method (Fig. 3.1) and current excitation ratios I_2/I_1 in numerical method (Fig. 3.20) for the stacked patch antenna operating at TM_{11} and TM_{21} modes, when both patches are fed along x-axis.

As we are interested in having antennas with broadside radiation patterns, with the phase centre displacement from the origin, we present two cases, for excitation amplitude ratios of 0.5 and 1. Figures 3.22 and 3.23 show the magnitude and phase of the E_θ pattern of the antenna when the antenna is located at the coordinate origin, with $C_2/C_1 = 1.0\angle 0$. Figure 3.24 shows the phase pattern of the same antenna, after displacing the entire antenna to the point $\left(r_o = 0.2\lambda, \phi_o = 180^o\right)$. Figures 3.25 to 3.27 compare the same properties as above for $C_2/C_1 = 0.5\angle 0$. This time, the phase centre moves to an intermediate point $\left(r_o = 0.1\lambda, \phi_o = 180^o\right)$.

These results confirm that after displacing the experimental antenna of Fig. 3.20 by a distance of $r_o = 0.2\lambda$ in Fig. 3.24, and $r_o = 0.1\lambda$ in Fig. 3.27, the phase patterns become uniform. These indicate that the antenna phase centre has moved along the negative x-direction by the excitation of the TM_{21} mode, exactly by the same distances as predicted by the analytical method.

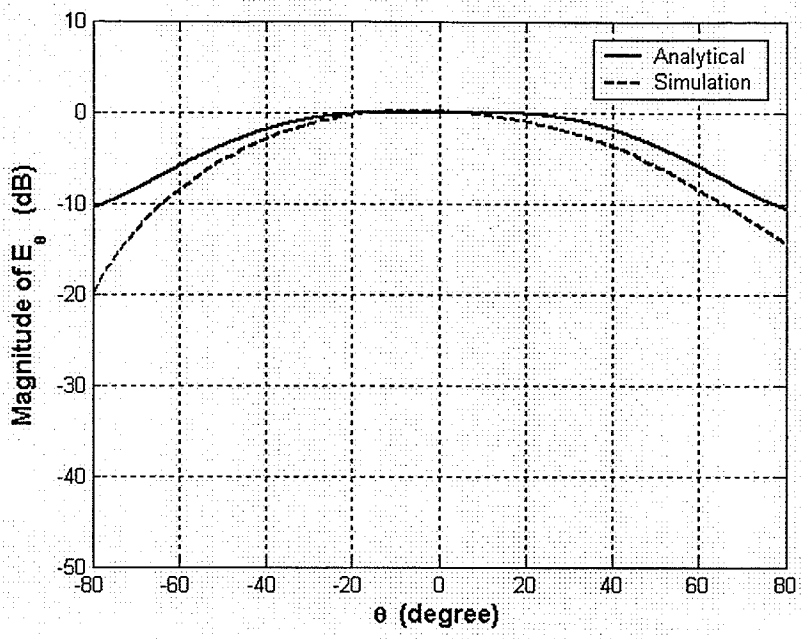

Fig. 3.22 Magnitude pattern of E_θ at $\phi = 0$ plane for the antenna shown in Fig. 3.20, when both patches are fed along x-axis, antenna is located at the origin, $(C_2 / C_1 = 1\angle 0)$.

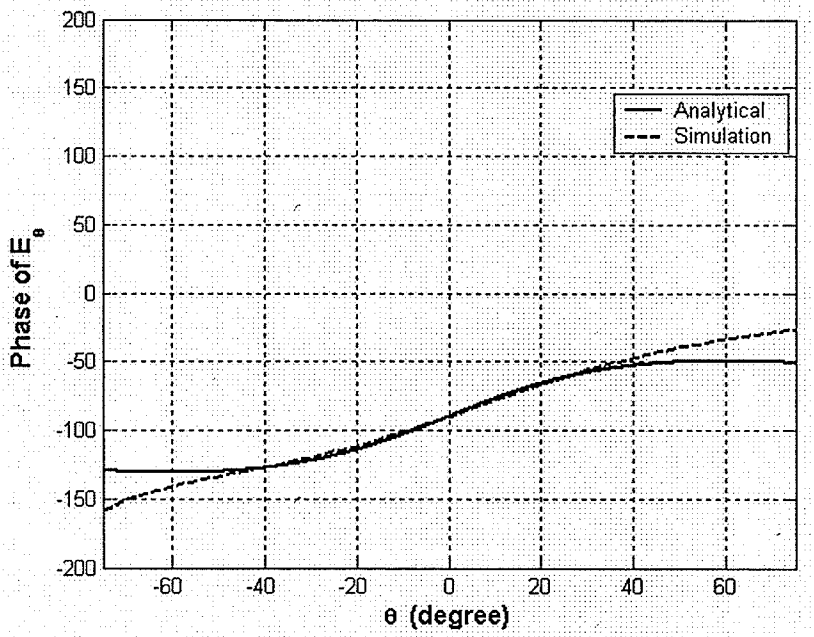

Fig. 3.23 Phase pattern of E_θ at $\phi = 0$ plane for the antenna shown in Fig. 3.20, when both patches are fed along x-axis, antenna is located at the origin, $(C_2 / C_1 = 1\angle 0)$.

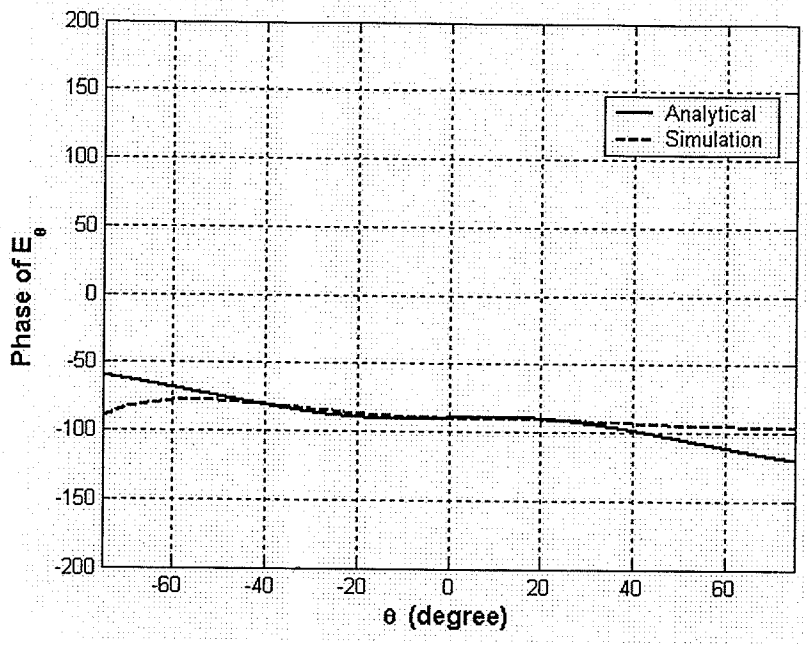

Fig. 3.24 Phase pattern of E_θ at $\phi = 0$ plane for the antenna shown in Fig. 3.20, when both patches are fed along x-axis and the antenna center moved to $(r_0 = 0.2\lambda, \phi_0 = 180^o)$ with $(C_2 / C_1 = 1\angle 0)$.

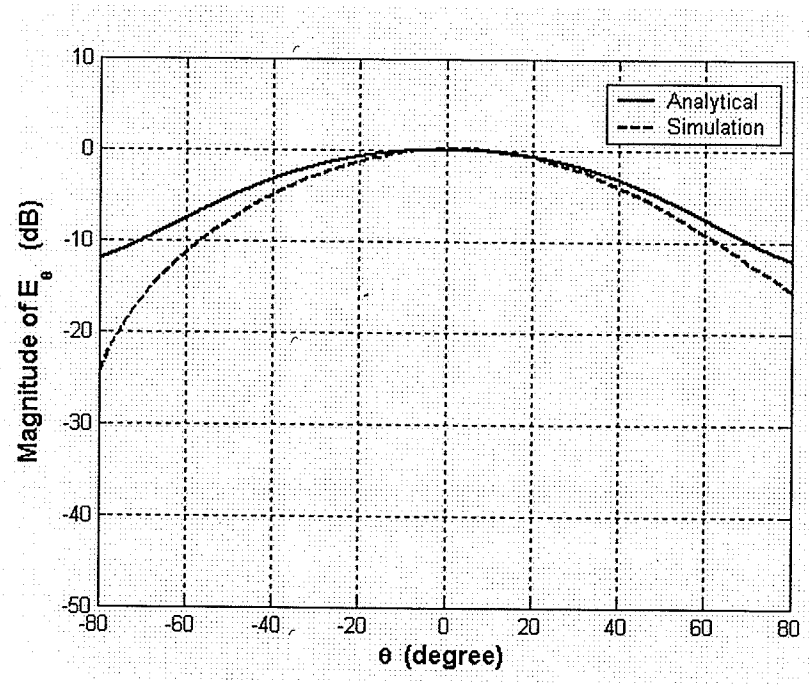

Fig. 3.25 Magnitude pattern of E_θ at $\phi = 0$ plane for the antenna shown in Fig. 3.20, when both patches are fed along x-axis, antenna is located at the origin, $(C_2 / C_1 = 0.5\angle 0)$.

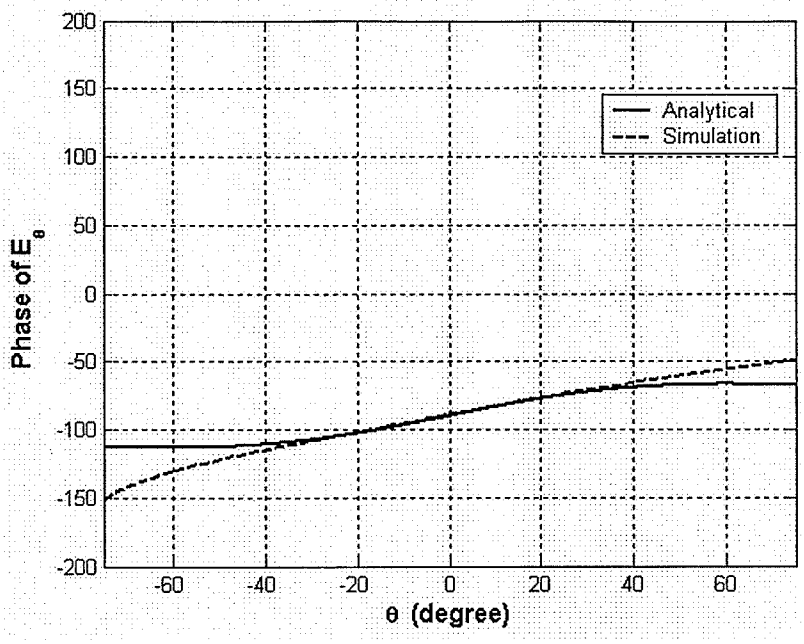

Fig. 3.26 Phase pattern of E_θ at $\phi = 0$ plane for the antenna shown in Fig. 3.20, when both patches are fed along x-axis, antenna is located at the origin, $(C_2 / C_1 = 0.5\angle 0)$.

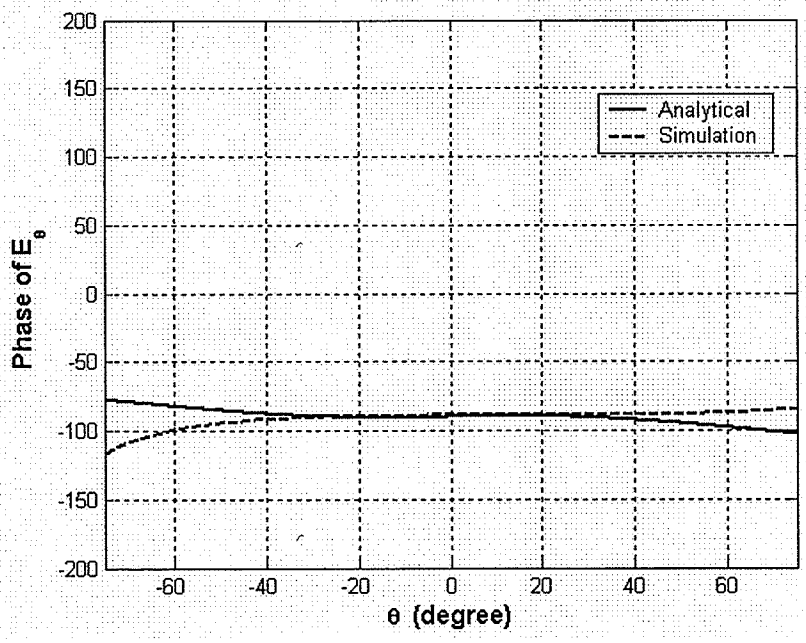

Fig. 3.27 Phase pattern of E_θ at $\phi = 0$ plane for the antenna shown in Fig. 3.20, when both patches are fed along x-axis and antenna center moved to $(r_0 = 0.1\lambda, \phi_0 = 180^o)$ with $(C_2 / C_1 = 0.5\angle 0)$.

Figure 3.28 and 3.29 show the copolar and crosspolar radiation patterns at $\phi = 45^0$ and $\phi = 90^0$ planes, for the above two different amplitude ratios. As can be seen, the crosspolarization at $\phi = 45^0$ plane does not have a symmetric pattern. The reason is that, due to the finite size of the ground plane, the peaks of the E-plane and H-plane may not be at the same directions, which lead to asymmetric crosspolarizations. By reducing the ground plane size to less than 0.8λ [10] (the antenna under study has a ground plane with diameter λ) one may obtain symmetric copolar radiation patterns, which in turn will give symmetric crosspolarization. This may be achieved by increasing the dielectric constant of the substrate, which reduces the size of each patch and, thus, the ground plane size can be reduced.

The normalized crosspolarization levels in the simulation results are slightly lower than what was obtained from the analytical ones in Figs. 3.18 and 3.19. This is due to the fact that, the analytical results of Figs. 3.18 and 3.19 were obtained when the antennas had an infinite ground plane. The case with a higher dielectric constant, which makes the crosspolar pattern symmetric, will be further discussed in chapter 5.

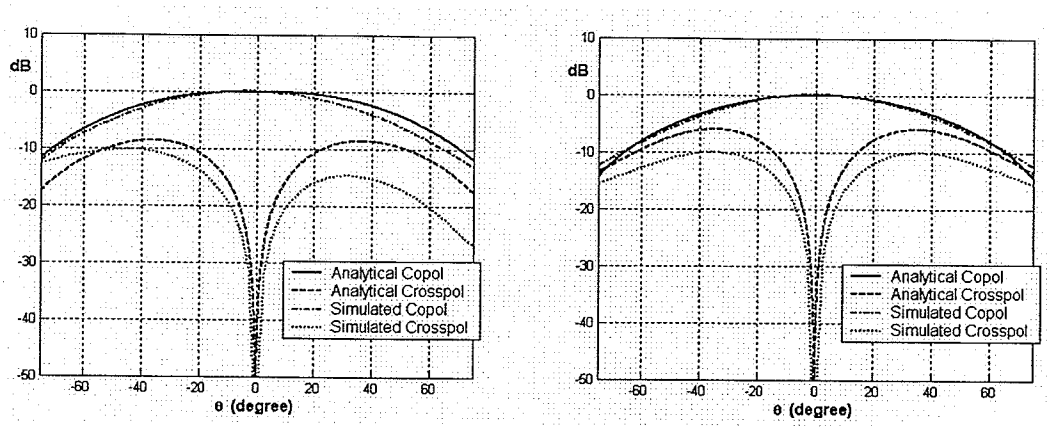

(a) *(b)*

Fig. 3.28 Normalized copolar and crosspolar radiation patterns of the antenna shown in Fig. 3.20, when both patches are fed along x-axis, $(C_2 / C_1 = 1\angle 0)$ *at (a)* $\phi = 45^\circ$, *(b)* $\phi = 90^\circ$

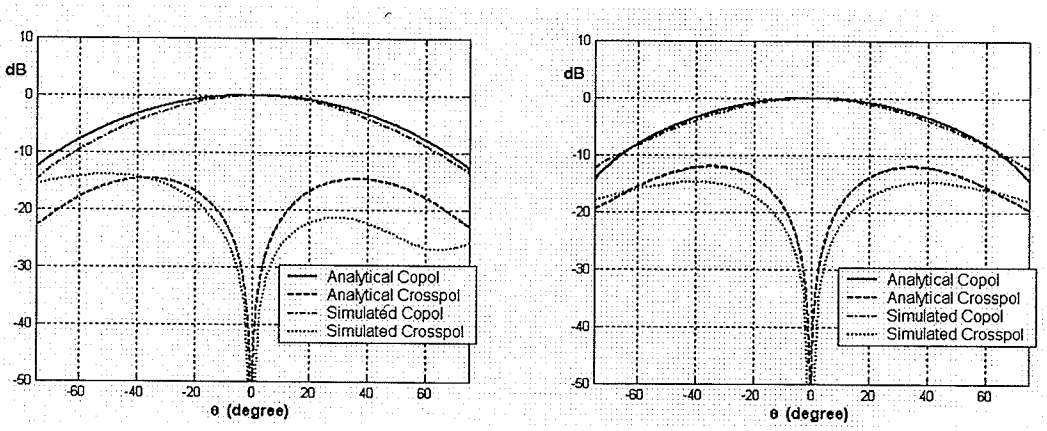

(a) *(b)*

Fig. 3.29 Normalized copolar and crosspolar radiation patterns of the antenna shown in Fig. 3.20, when both patches are fed along x-axis, $(C_2 / C_1 = 0.5\angle 0)$ *at (a)* $\phi = 45^\circ$, *(b)* $\phi = 90^\circ$

3.3 Case II, patches fed 45 degrees apart

3.3.1 Analytical Model

3.3.1.1 Radiation amplitude and phase patterns

In this section, we study the same antenna as in section 3.2, except that the feeds for the TM_{11} and TM_{21} patches are placed 45° away from each other, as shown in Fig. 3.30. The TM_{11} patch is fed at $\phi_m = 0$ and the TM_{21} patch is fed at $\phi_m = 45^o$. Using equations 2.12 and 2.13, the total far fields become:

$$E_\theta = -jC_1 e^{jk_0 r_o \sin\theta\cos(\phi-\phi_0)}\left\{[J_0(u_1)-J_2(u_1)]\cos\phi + j\frac{C_2}{C_1}[J_1(u_2)-J_3(u_2)]\sin 2\phi\right\}\frac{e^{-jk_0 r}}{r} \quad (3.15)$$

$$E_\phi = jC_1 e^{jk_0 r_o \sin\theta\cos(\phi-\phi_0)}\left\{[J_0(u_1)+J_2(u_1)]\sin\phi - j\frac{C_2}{C_1}[J_1(u_2)+J_3(u_2)]\cos 2\phi\right\}\cos\theta\frac{e^{-jk_0 r}}{r} \quad (3.16)$$

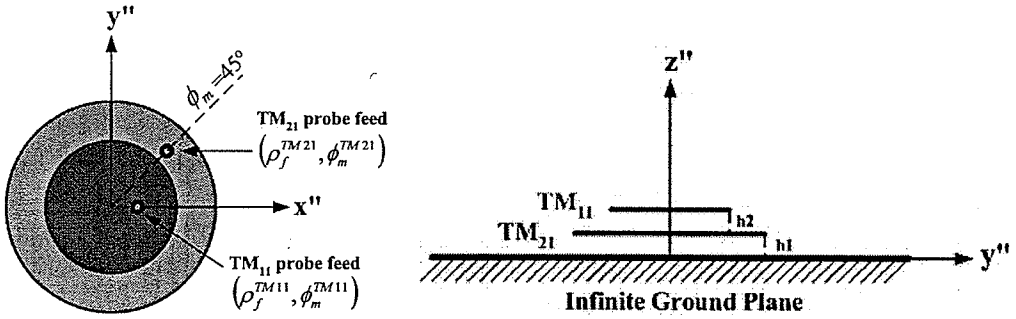

Fig. 3.30 (a)Top view (b) cross-section view of a stacked patch microstrip antenna operating at TM_{11} and TM_{21} modes over an infinite ground plane, when the TM_{11} and TM_{21} patches are fed at $\phi_m = 0$ and $\phi_m = 45^o$, respectively, $\varepsilon_r = 1.15$, $h_1 = h_2 = 1.5mm$, $a_{TM11} = 6.8mm$, $a_{TM21} = 12.42mm$, f=10GHz.

In this case, E_θ at $\phi = 0$ plane is due to only the TM_{11} mode, which has a constant phase pattern. The E_ϕ pattern, however is due to both TM_{11} and TM_{21} modes,

and is considered for studying the effect of both modes for this structure. Figures 3.31 and 3.32 show the magnitude and phase patterns of the E_ϕ at $\phi = 90^o$ plane, respectively, when the excitations are in-phase, $\alpha_1 = \alpha_2$, and the antenna is located at the coordinate origin. They illustrate that, by increasing the absolute value of the excitation ratio, the amplitude and phase patterns move towards those of the TM_{21} mode. It also shows that for the in-phase excitations, there is a null at the boresight, when $C_2/C_1 >> 1$. In addition, the phase patterns for non-zero excitation ratios are not constant implying that, the phase centre of the antenna has moved from the origin. In order to have a constant phase distribution around the main beam, we must add a phase term with a negative-slope to compensate for the initial phase radiation.

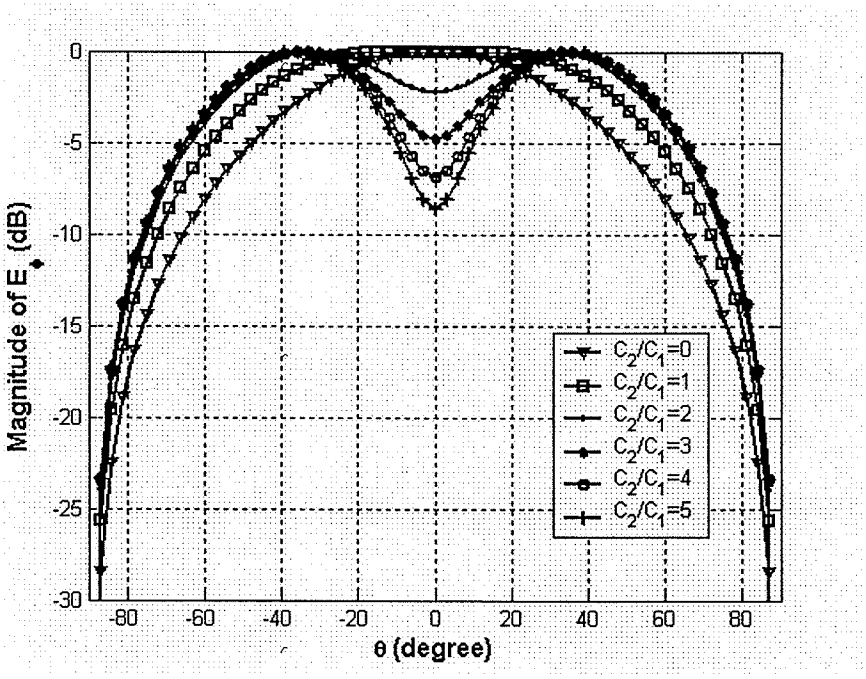

Fig. 3.31 Magnitude patterns of E_ϕ for combined TM_{11} and TM_{21} modes at $\phi = 90^o$ plane for different amplitude ratios and in-phase excitations, $\alpha_1 = \alpha_2$, for the antenna shown in Fig. 3.30, when $(r_0 = 0, \phi_0 = 0)$ and two patches are fed 45° apart.

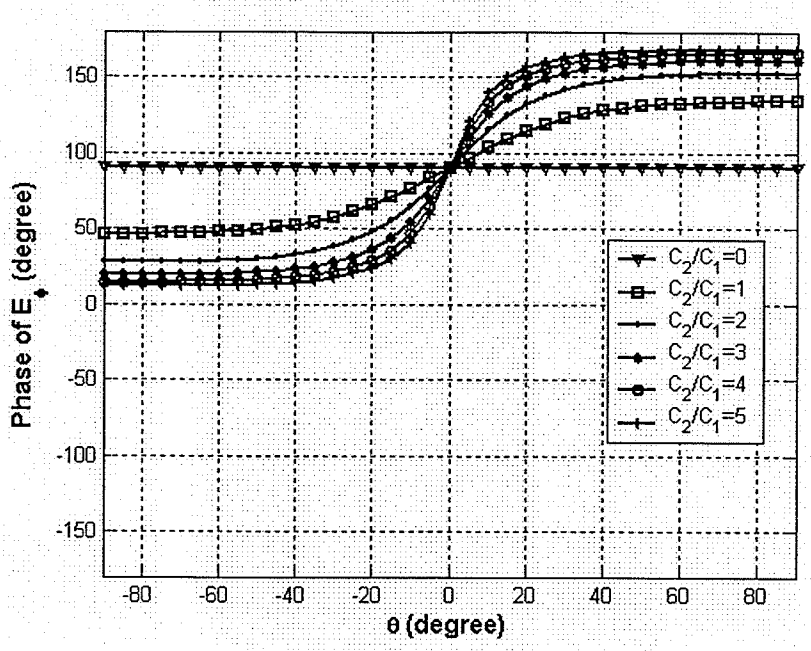

Fig. 3.32 Phase patterns of E_ϕ at $\phi = 90^o$ plane for different amplitude ratios and in-phase excitations, $\alpha_1 = \alpha_2$, for the antenna shown in Fig. 3.30, when $(r_0 = 0, \phi_0 = 0)$ and two patches are fed 45° apart.

Now, let us consider out of phase excitations, $|\alpha_1 - \alpha_2| \leq 90^o$, of these two modes by assuming that α_1 and α_2 are the excitation phases for TM_{11} and TM_{21} modes, respectively. Again, out of phase excitation makes the radiation pattern to have only one peak, which depends on the sign of the phase difference in such a way that for positive $\alpha_1 - \alpha_2$, the main beam moves to positive θ, or $\phi = 0$ side, and for negative $\alpha_1 - \alpha_2$, the main beam moves to negative θ, or $\phi = 180^o$ side.

Figures 3.33 to 3.36 show the magnitudes and phases of the E_ϕ patterns at $\phi = 90^o$ plane, when the two modes have an out of phase excitation, but equal amplitude, while the antenna is located at the coordinate origin.

It is important to note that a quadrature phase difference, $|\alpha_1 - \alpha_2| = 90^o$, makes the far field phase pattern flat over the entire observation angle range, which in turn pushes the phase centre location to the physical center of the antenna. The reason is that, a 90° phase shift cancels the effect of j coefficient in the expression for the TM_{11} mode, as shown in equations 3.16.

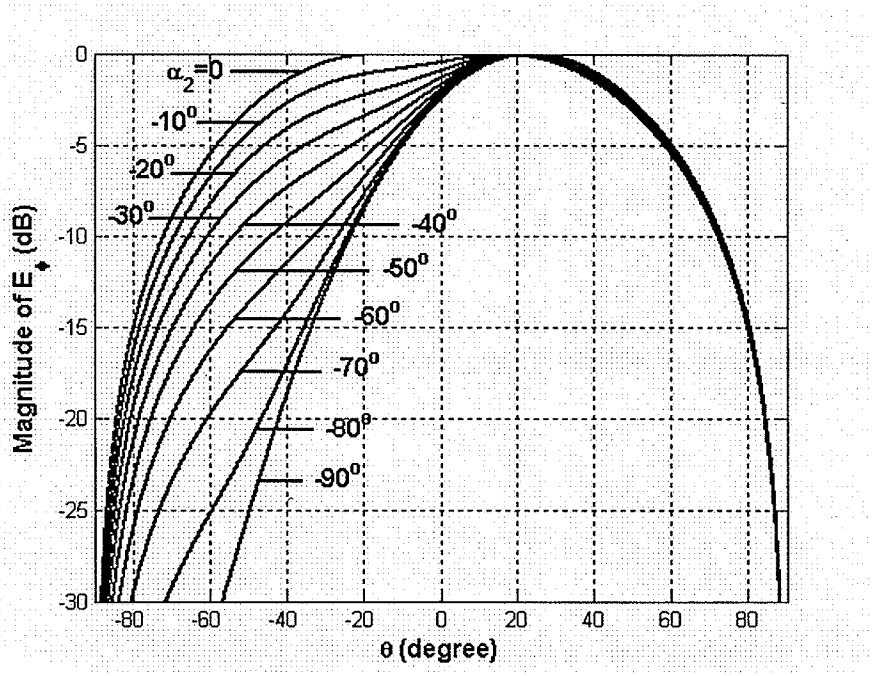

Fig. 3.33 Magnitude patterns of E_ϕ at $\phi = 90^o$ plane for different negative values of α_2 phase excitations, $\alpha_1 = 0$ and $|C_1| = |C_2| = 1$ (Antennas located at the origin and two patches are fed 45° apart as shown in Fig. 3.30).

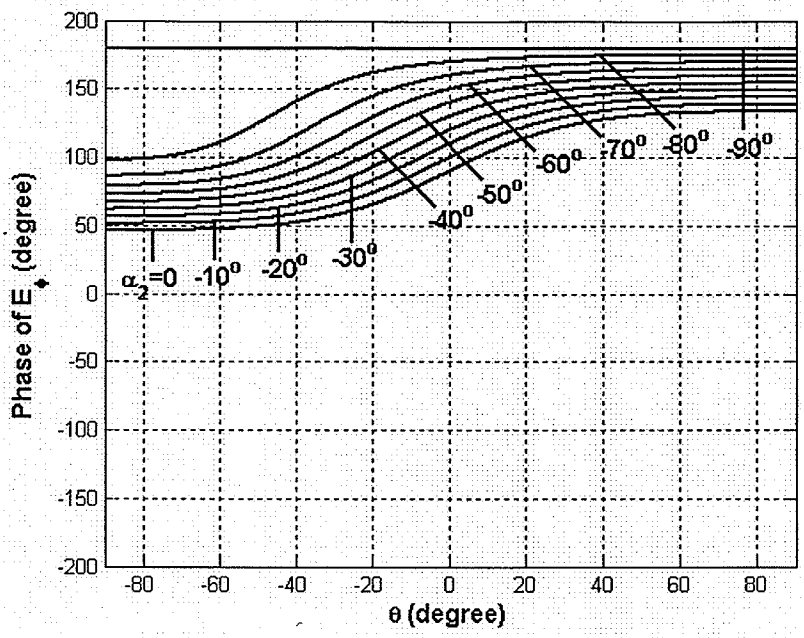

Fig. 3.34 Phase patterns of E_ϕ at $\phi = 90^o$ plane for different negative values of α_2 phase excitations, $\alpha_1 = 0$ and $|C_1| = |C_2| = 1$ (Antennas located at the origin and two patches are fed 45° apart as shown in Fig. 3.30).

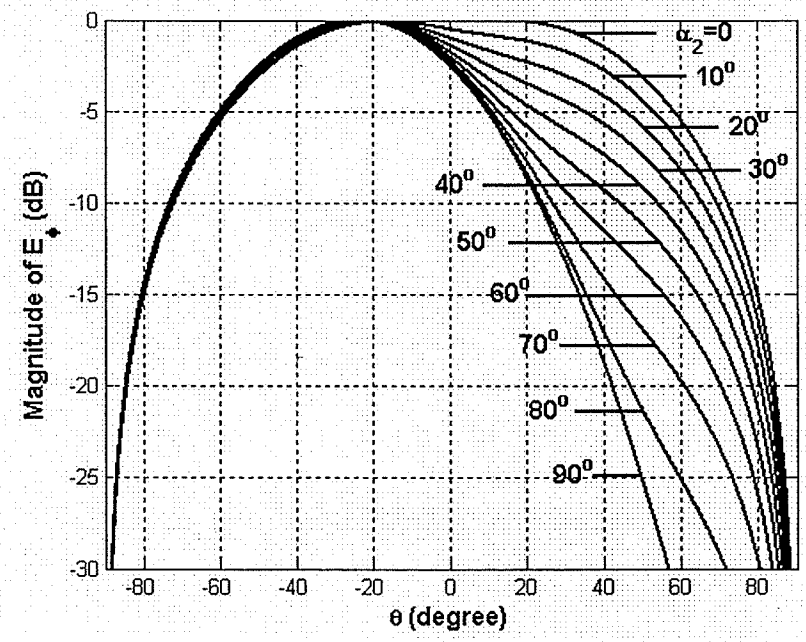

Fig. 3.35 Magnitude patterns of E_ϕ at $\phi = 90^o$ plane for different positive values of α_2 phase excitations, $\alpha_1 = 0$ and $|C_1| = |C_2| = 1$ (Antennas located at the origin and two patches are fed 45° apart as shown in Fig. 3.30).

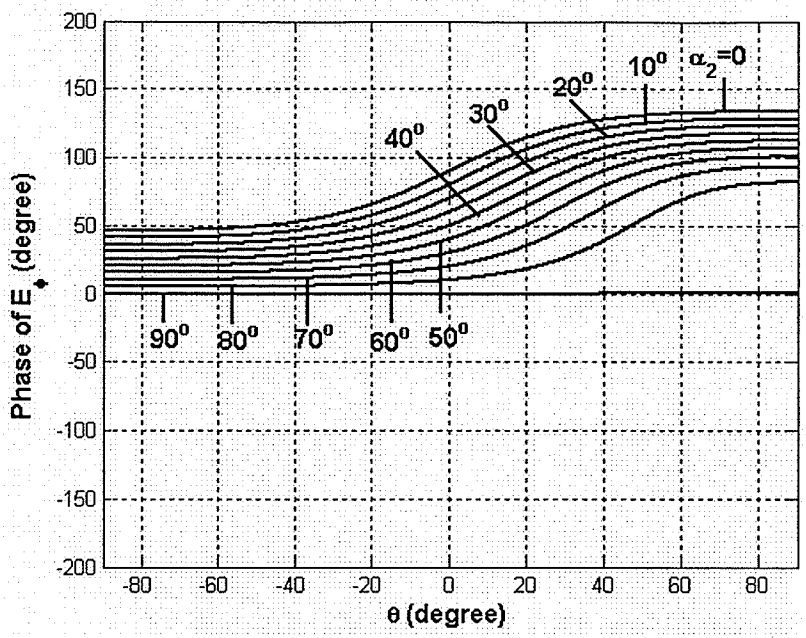

Fig. 3.36 Phase patterns of E_ϕ at $\phi = 90^\circ$ plane for different positive values of α_2 phase excitations, $\alpha_1 = 0$ and $|C_1| = |C_2| = 1$ (Antennas located at the origin and two patches are fed 45° apart as shown in Fig. 3.30).

3.3.1.2 Phase centre location and main beam tilt angle

The locus of the E_ϕ pattern phase centre is a line passing through the point $(r_0, \phi_0 = 270^\circ)$ and perpendicular to $\phi = 90^\circ$ direction as illustrated in Fig. 3.37, based on the discussion in section 3.2.1.2.

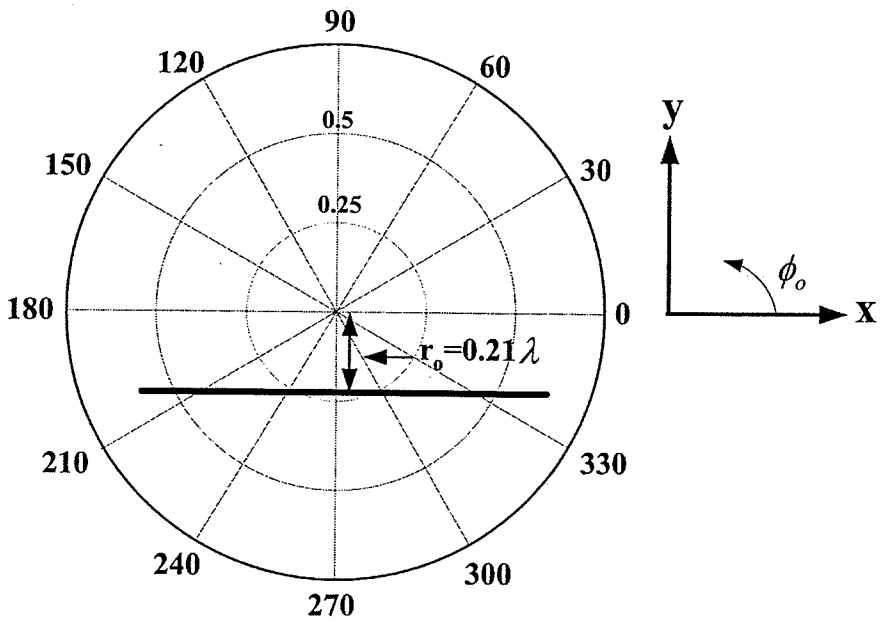

Fig. 3.37 The locus of the E_ϕ pattern phase centre at $\phi = 90^o$ plane of the antenna shown in Fig. 3.30, when $\phi_{m_{TM11}} = 0$, $\phi_{m_{TM21}} = 45^o$ and $\frac{C_2}{C_1} = 1\angle 0$

In this section, the results for phase centre location of the E_ϕ patterns are presented. The effects of excitation amplitude ratio on the phase centre location and main beam direction are shown in Figs. 3.38 and 3.39, respectively, for different excitation phases. As can be seen, for all excitation phases except for 90° phase difference, that keeps the phase centre at the coordinate origin, the phase centre moves from the center until the excitation amplitude ratio becomes unity. Beyond that, it returns to the antenna center, since in the limit we have only the TM_{21} mode, and the phase centre must be at the coordinate origin. The main beam also moves to that of the TM_{21} mode. It is interesting to note that, for the in-phase excitation, with amplitude ratios of up to unity, the main beam remains at the boresight direction, while the antenna phase centre moves away from the antenna center, leading to a virtual antenna concept.

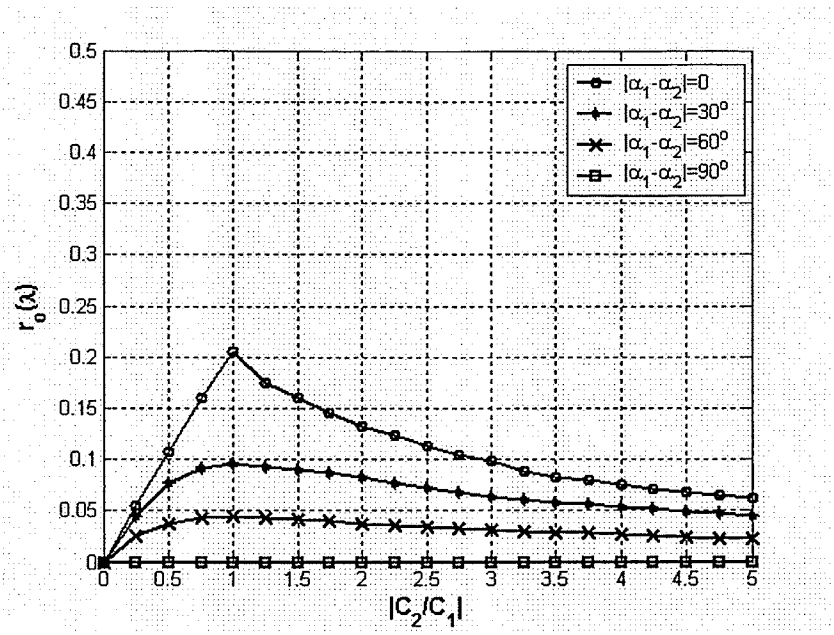

Fig. 3.38 Effect of $\left|\frac{C_2}{C_1}\right|$ *on phase centre location of* E_ϕ *at* $\phi = 90^o$ *plane for different excitation phases over main beam, for the antenna shown in Fig. 3.30, when two patches are fed 45° apart, while* $\phi_0 = 270^o$.

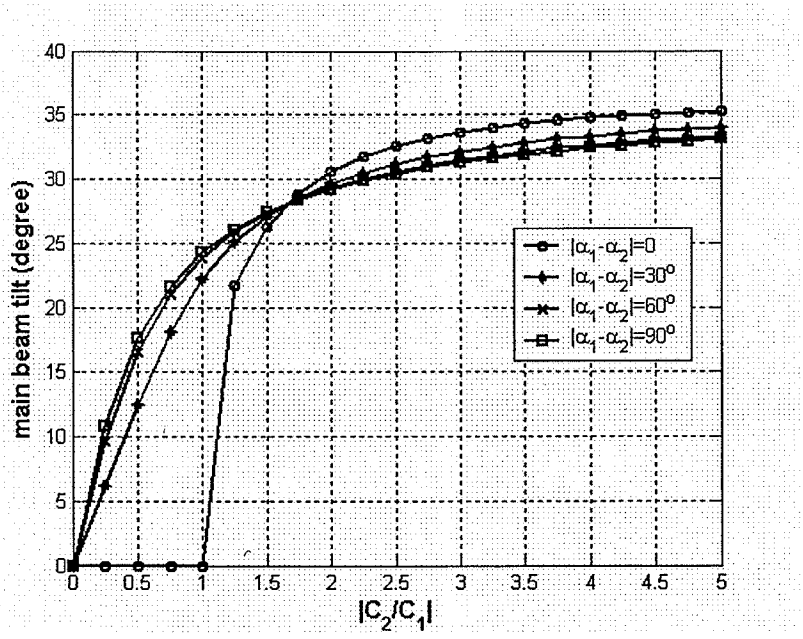

Fig. 3.39 Effect of $\left|\frac{C_2}{C_1}\right|$ *on main beam tilt angle for* E_ϕ *at* $\phi = 90^o$ *plane for different excitation phases of the antenna shown in Fig. 3.30, when two patches are fed 45° apart, while* $\phi_0 = 270^o$.

The effects of the excitation phase difference on the phase centre location and main beam direction were also studied and are shown in Figs. 3.40 and 3.41, respectively, for different excitation amplitude ratios. They show that, the phase centre converges to the antenna center for the quadrature phase difference, $|\alpha_1 - \alpha_2| = 90^o$. The main beam direction is almost constant, over all excitation phases, when the amplitude ratio, $\frac{C_2}{C_1} \geq 2$, while the phase centre location changes, which are the interesting cases. For the amplitude ratios $\frac{C_2}{C_1} \leq 1$, all main beams originate from the boresight, and their tilt increases with higher excitation phases.

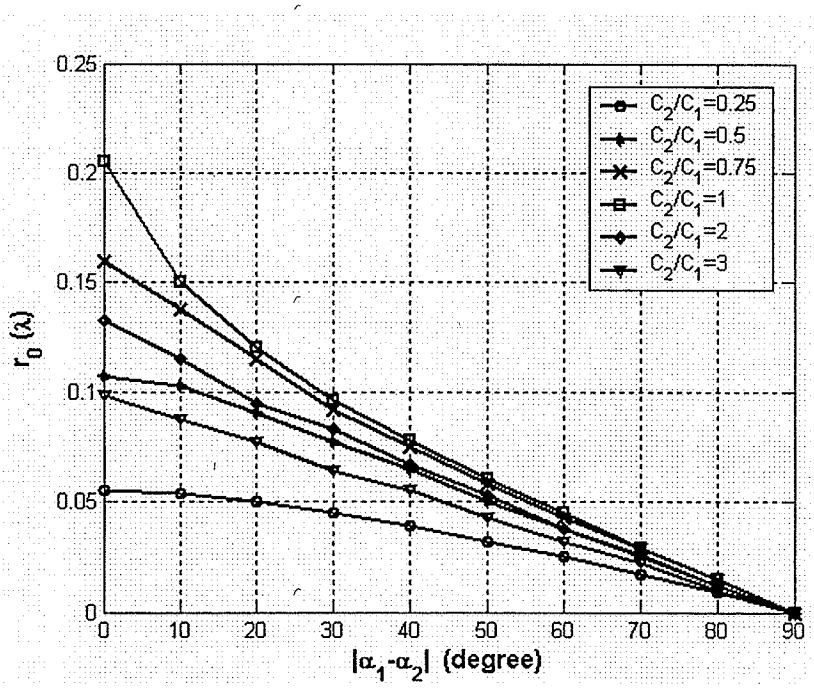

Fig. 3.40 Phase centre location of E_ϕ at $\phi = 90^o$ plane versus phase difference excitations for different $\left|\frac{C_2}{C_1}\right|$, over main beam, of the antenna shown in Fig. 3.30, when two patches are fed 45° apart, while $\phi_0 = 270^o$.

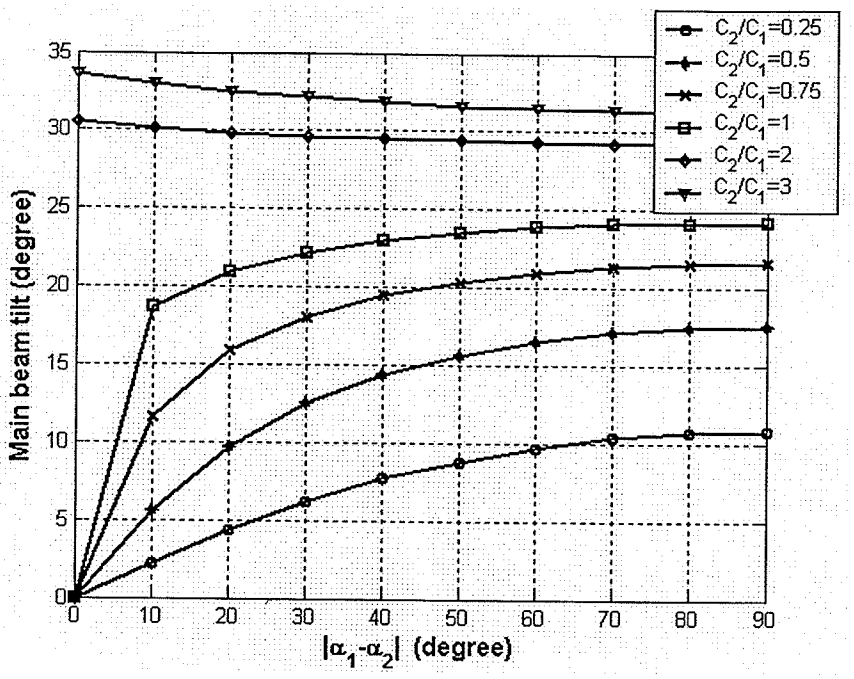

Fig. 3.41 Main beam tilt of E_ϕ at $\phi = 90^o$ plane versus phase difference excitations for different $\left|\frac{C_2}{C_1}\right|$, of the antenna shown in Fig. 3.30, when two patches are fed 45° apart, while $\phi_0 = 270^o$.

3.3.1.3 Polarization properties

The antenna under study in this section operates at TM_{11} and TM_{21} modes, when patches are fed 45 degree away. It is an x-polarized antenna and the copolar and crosspolar patterns can then be calculated, using equation 3.8, where E_θ and E_ϕ are given in equations 3.15 and 3.16.

Similarly, as discussed in section 3.2.1.3, there is a global phase centre location, when the copolar radiation pattern is considered. Figure 3.42 shows the effect of amplitude excitation ratio on this phase centre location. This time, the phase centre is at $\phi_0 = 270^o$.

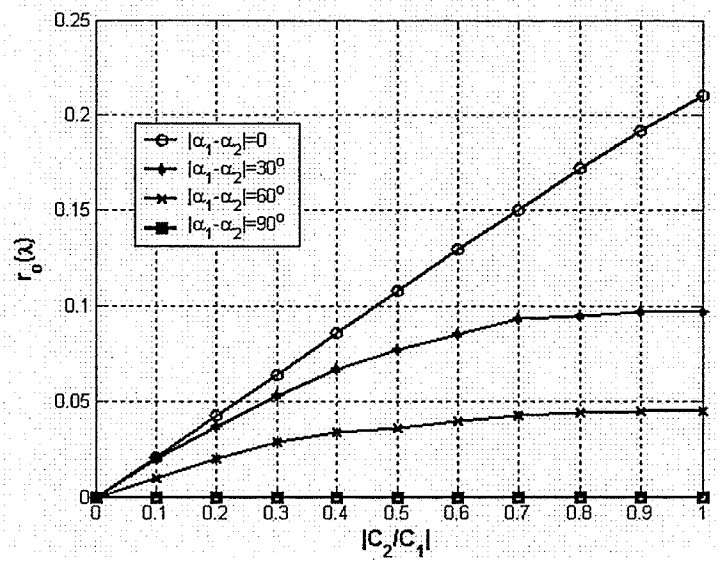

Fig. 3.42 Effect of $\left|\frac{C_2}{C_1}\right|$ *on phase centre of copolar radiation pattern of the antenna shown in Fig. 3.30, when* $\phi_0 = 270^o$ *over main beam.*

The expressions for the copolar and crosspolar patterns at different ϕ-planes are given as below:

- At $\phi = 0$ plane:
$$\left\{\begin{matrix} E_{co}\,|_{\phi=0} = E_\theta\,|_{\phi=0} \\ E_{xpol}\,|_{\phi=0} = E_\phi\,|_{\phi=0} \end{matrix}\right\} \qquad (3.17)$$

- At $\phi = 90^o$ plane:
$$\left\{\begin{matrix} E_{co}\,|_{\phi=90^o} = -E_\phi\,|_{\phi=90^o} \\ E_{xpol}\,|_{\phi=90^o} = E_\theta\,|_{\phi=90^o} = 0 \end{matrix}\right\} \qquad (3.18)$$

- At $\phi = 45^o$ plane:

$$\left\{\begin{matrix} E_{co}\,|_{\phi=45^o} = \left(\cos\phi\, E_\theta - \sin\phi\, E_\phi\right)|_{\phi=45^o} \\ E_{xpol}\,|_{\phi=45^o} = \left(\sin\phi\, E_\theta + \cos\phi\, E_\phi\right)|_{\phi=45^o} \end{matrix}\right\} \qquad (3.19)$$

As can be seen, at $\phi = 90^o$ plane, the crosspolarization is zero, since E_θ for both modes vanishes on this plane. Figure 3.43 shows the copolar and crosspolar patterns at $\phi = 0^o$

plane, for different mode excitation ratios. The crosspolarization, at $\phi = 0^o$ plane, is mainly due to the E_ϕ component of the TM_{21} mode and it increases with higher mode ratios.

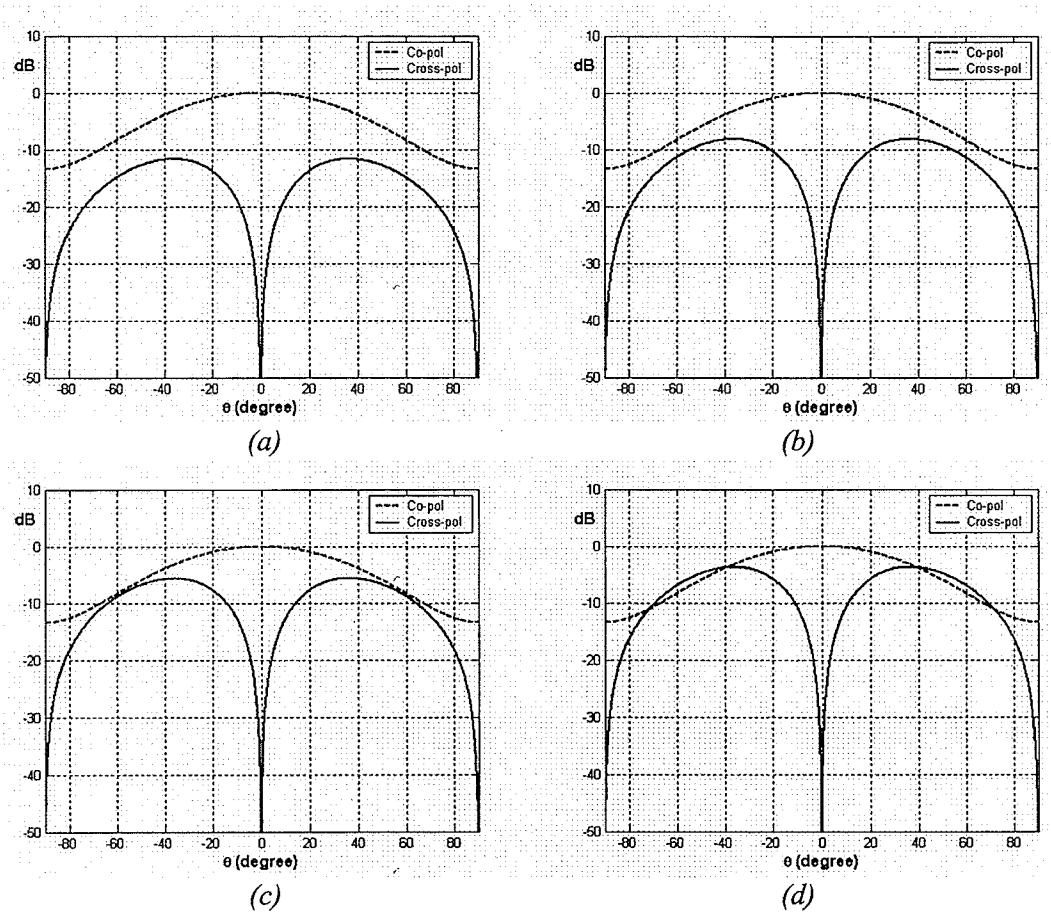

Fig. 3.43 Normalized copolar and crosspolar components at $\phi = 0^o$ plane of the antenna shown in Fig. 3.30, when two patches are fed 45° apart

(a) $\frac{C_2}{C_1} = 0.5\angle 0$, *(b)* $\frac{C_2}{C_1} = 0.75\angle 0$, *(c)* $\frac{C_2}{C_1} = 1\angle 0$, *(d)* $\frac{C_2}{C_1} = 1.25\angle 0$

At $\phi = 45^o$ plane, both TM_{11} and TM_{21} modes contribute to the crosspolarization patterns, as shown in Fig. 3.44. The normalized crosspolarizations versus the excitation amplitude ratio are plotted in Figs. 3.45 and 3.46, at $\phi = 0^o$ and $\phi = 45^o$ planes,

respectively. They show that, at both planes, the crosspolarization is lower for the small excitation amplitude ratios, since by increasing this ratio, the contribution of the TM_{21} mode increases and the crosspolarization level increases.

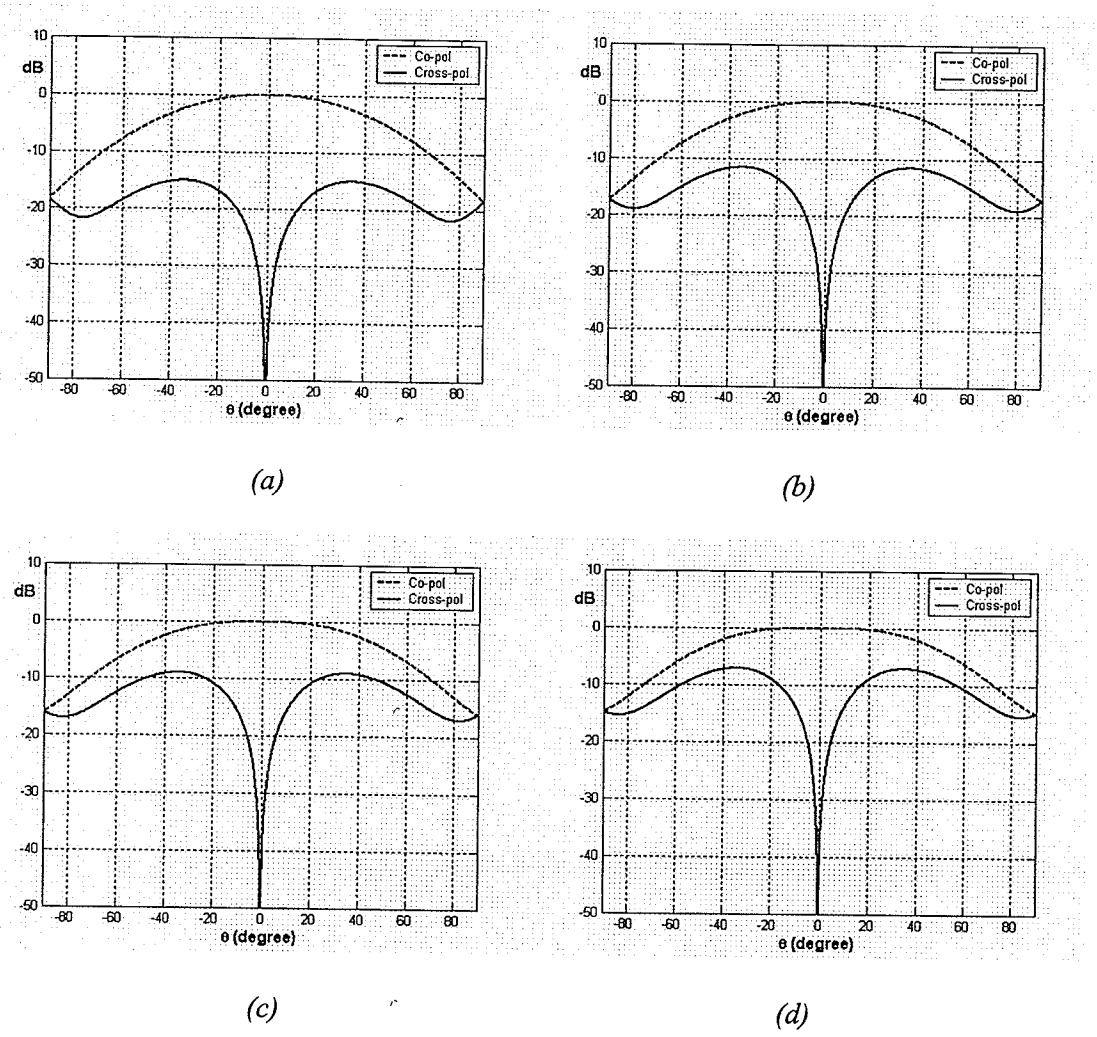

Fig. 3.44 Normalized copolar and crosspolar components at $\phi = 45^{o}$ plane of the antenna shown in Fig. 3.30, when two patches are fed 45° apart

(a) $\frac{C_2}{C_1} = 0.5\angle 0$, *(b)* $\frac{C_2}{C_1} = 0.75\angle 0$, *(c)* $\frac{C_2}{C_1} = 1\angle 0$, *(d)* $\frac{C_2}{C_1} = 1.25\angle 0$

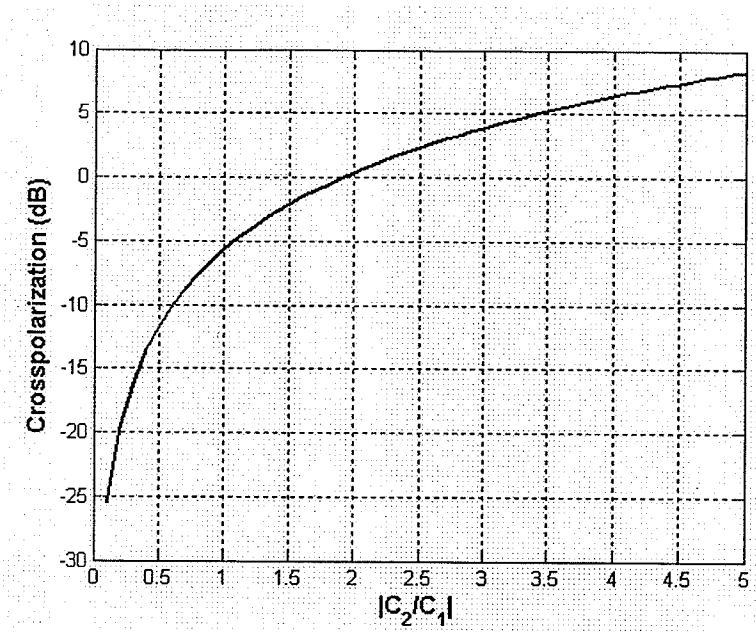

Fig. 3.45 Crosspolarization versus excitation amplitude ratio, $\left|\frac{C_2}{C_1}\right|$, *at* $\phi = 0^\circ$ *plane of the antenna shown in Fig. 3.30, when two patches are fed 45° apart and* $\alpha_1 = \alpha_2$.

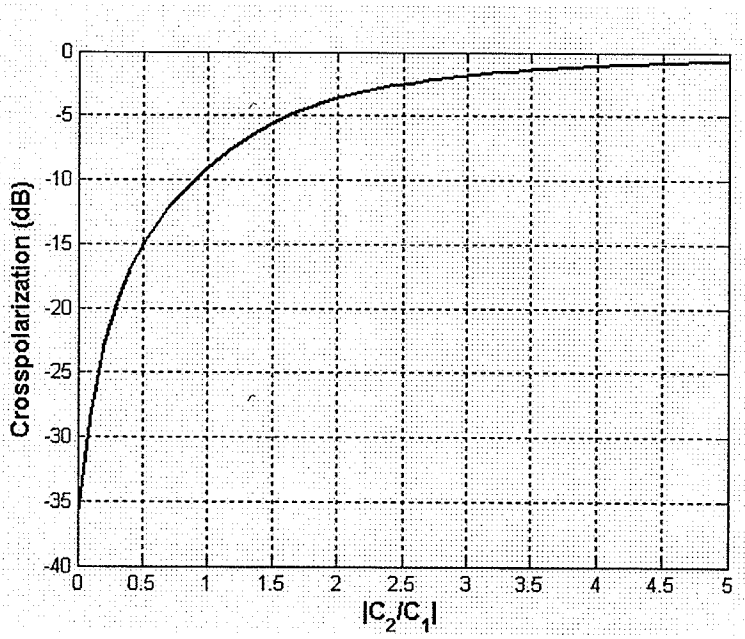

Fig. 3.46 Crosspolarization versus excitation amplitude ratio, $\left|\frac{C_2}{C_1}\right|$, *at* $\phi = 45^\circ$ *plane of the antenna shown in Fig. 3.30, when two patches are fed 45° apart and* $\alpha_1 = \alpha_2$.

3.3.2 Design Example

The geometry of the antenna is the same as Fig. 3.20 except that, the feeds are 45 degree away from each other. The phase centre of the E_ϕ pattern for equal amplitude ratio, is located at $(r_o = 0.2\lambda, \phi_o = 270^o)$ and for $\frac{C_2}{C_1} = 0.5\angle 0$ it is at $(r_o = 0.1\lambda, \phi_o = 270^o)$, the same as the phase centre of the E_θ patterns, when both patches are fed along the x-axis, except ϕ_o is different. Therefore, we don't repeat them here. But we have a symmetric crosspolarization patterns at $\phi = 45^o$ plane as shown in Figs. 3.47 and 3.48. As can be seen, the crosspolarization level is almost the same as the numerical results. The small difference is due to the finite ground plane size, mutual coupling between the two ports, and infinite size of dielectric substrate in the numerical simulation.

Here, by placing the feeds 45 degree away from each other, the phase relationship between the two ports changes to $\angle I_{TM11} = 60^o$, $\angle I_{TM21} = -100^o$, based on the discussion in section 3.2.2. It means, the identical mode coefficients, C_1=C_2 and $\alpha_1 = \alpha_2$, in the analytical approach correspond to the following current excitations in numerical simulations, as shown in table 3.2:

$$I_{TM11} = 83mA\angle 60^o, I_{TM21} = 50mA\angle -100^o, \Delta\phi = -160^o \quad (3.20)$$

Excitation Ratio	Amplitude	Phase (degrees)
Analytical $(\frac{C_2}{C_1})$	1	0
Numerical $(\frac{I_{TM21}}{I_{TM11}})$	0.6024	-160°

Table 3.2 Relation between excitation ratios C_2/C_1 in analytical method (Fig. 3.30) and current excitation ratios I_2/I_1 in numerical method for the stacked patch antenna operating at TM_{11} and TM_{21} modes, when two patches are fed 45° apart.

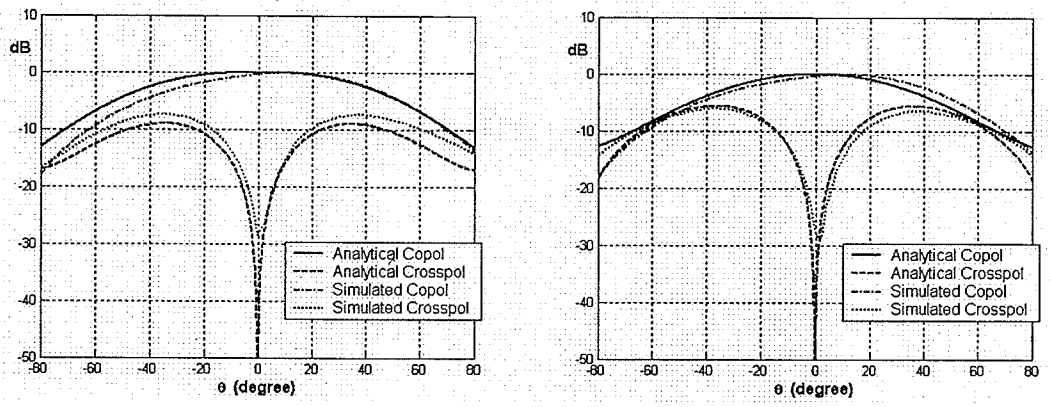

Fig. 3.47 Normalized copolar and crosspolar radiation patterns of the stacked patch antenna shown in Fig. 3.20, when two patches are fed 45° away, $(C_2 / C_1 = 1\angle 0)$ at (a) $\phi = 45°$, (b) $\phi = 0°$

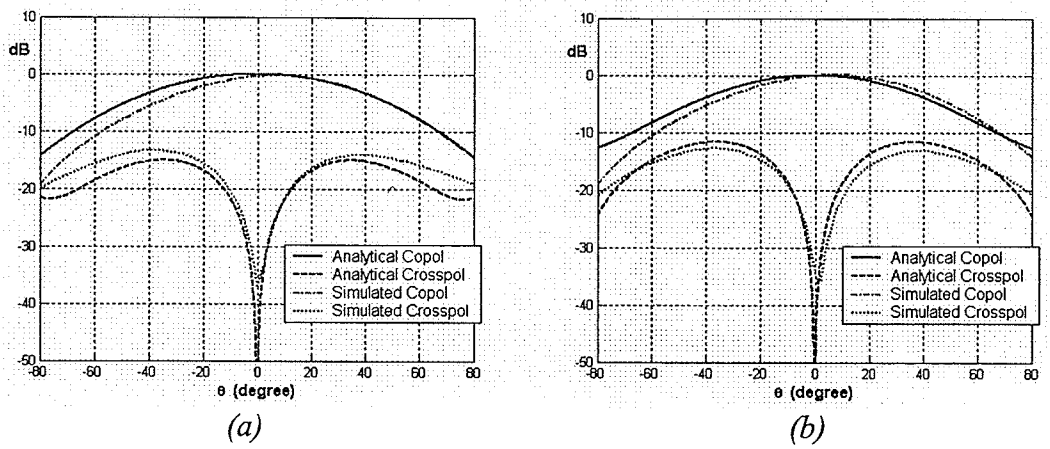

Fig. 3.48 Normalized copolar and crosspolar radiation patterns of the stacked patch antenna shown in Fig. 3.20,when two patches are fed 45° away, $(C_2 / C_1 = 0.5\angle 0)$ at (a) $\phi = 45°$, (b) $\phi = 0°$

3.4 Summary

In this chapter, the phase centre location, main beam tilt angle and polarization of the antenna with a combined TM_{11} and TM_{21} mode excitations, when used as a stacked antenna, were studied both analytically and numerically. Two cases were considered in terms of the feed location for the TM_{21} mode, one at $\phi_m = 0$, and the other at $\phi_m = 45^o$ plane. That is, the patches were fed along the x-axis or 45° apart. There was a good agreement between analytical results using the cavity model, and numerical results using the Method of Moment for the two design examples in sections 3.2.2 and 3.3.2. In these design examples a finite ground plane was assumed, which affected the crosspolarization. Thus, the crosspolarization results of these examples with the analytical ones were not completely the same. Moreover, adding the TM_{21} mode to the dominant mode resulted in increased crosspolarization levels.

It was shown that, there is a global phase centre location when the copolar radiation pattern is considered. When both TM_{11} and TM_{21} patches were fed along the x-axis, the antenna (case I) was x-polarized. This antenna was found to have a global phase centre location at $(r_0, \phi_0 = 180^o)$, for excitation amplitude ratio less than unity. Similarly, the antenna of case II was also x-polarized. This antenna had also a global phase centre location for excitation amplitude ratio less than unity. But, its global phase centre was located at $(r_0, \phi_0 = 270^o)$. It means that the phase centre location of such an antenna is perpendicular to its polarization direction.

Chapter 4

Stacked Patch Circular Microstrip Antenna operating at TM_{11} and TM_{02} modes

4.1 Introduction

In this chapter, a two-layer circular microstrip patch antenna is studied, when the lower patch generates the TM_{02} mode, which has a circularly symmetric radiation pattern with a null at the boresight. The upper patch produces the TM_{11} mode and has a broadside radiation pattern. Again, this structure is first treated analytically, using the cavity model, to better understand the problem. For simplicity, the ground plane of the antenna is assumed to be infinite in size and the mutual coupling between the two ports is neglected. The analysis is based on the cavity model. In order to verify the results, the same structure with a finite ground plane is investigated by Ansoft Designer version 2, which uses a Method of Moment for the antenna analysis. The phase centre location, main beam tilt angle, and crosspolarization properties are studied in terms of the amplitude ratio and phase difference between the two modes.

4.2 Analytical model

4.2.1 Radiation amplitude and phase patterns

In this section, we develop a Matlab program to calculate the far field radiation patterns based on the cavity model, which was formulated in chapter 2. The entire antenna is over an infinite ground plane and the mutual coupling between the two modes

is neglected. Due to the fact that, the TM_{02} mode can be excited by a probe at its center, where the electric field is the strongest, we considered just one case when both probes are aligned along the x-axis as shown in Fig. 4.1.

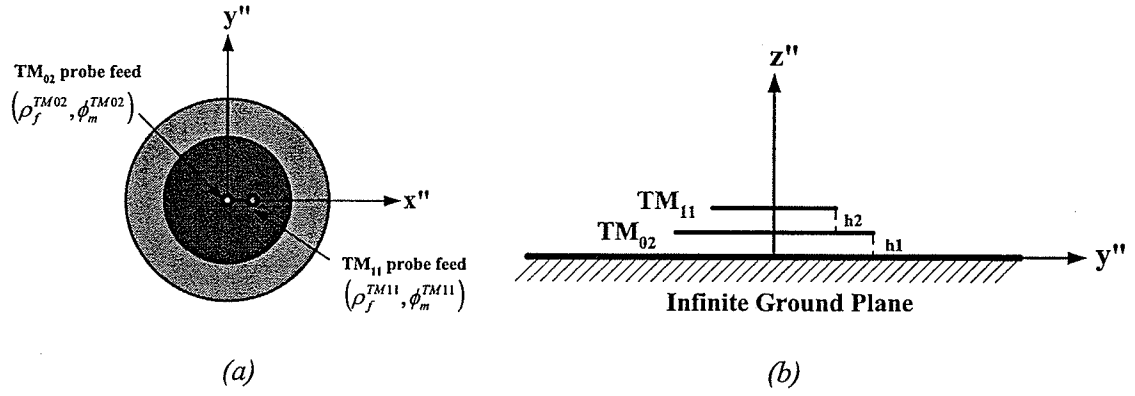

Fig. 4.1 (a) Top view (b) cross-section view of a stacked patch microstrip antenna operating at TM_{11} and TM_{02} modes over an infinite ground plane, when both patches are fed along x-direction $\varepsilon_r = 1.15, h_1 = h_2 = 1.5mm$, $a_{TM11} = 6.8mm$, $a_{TM02} = 15.27mm$ *, f=10GHz.*

The antenna was designed to resonate at 10GHz. The patch sizes were determined using equations 2.8 to 2.11, where the eigenvalues for the TM_{11} and TM_{02} modes are 1.841 and 3.8317, respectively. Both layers have the same thickness of 1.5mm, and are etched on the same type substrate with $\varepsilon_r = 1.15$. Similarly, the effect of dielectric thickness on the phase distribution is ignored, as discussed in chapter 2, section 2.2.2. For the TM_{11} and TM_{02} modes and using equations 2.12, 2.13 and 2.14, the far fields in spherical coordinates, with the patch centers at (r_o, ϕ_o, 0) according to Fig. 2.2, can be expressed as,

TM_{11} Mode:

$$E_\theta = -jC_1 \frac{e^{-jk_0 r}}{r} e^{jk_0 r_o \sin\theta\cos(\phi-\phi_0)} \left[J_0(k_0 a_1 \sin\theta) - J_2(k_0 a_1 \sin\theta)\right]\cos\phi \qquad (4.1)$$

$$E_\phi = jC_1 \frac{e^{-jk_0 r}}{r} e^{jk_0 r_o \sin\theta\cos(\phi-\phi_0)} \left[J_0(k_0 a_1 \sin\theta) + J_2(k_0 a_1 \sin\theta)\right]\cos\theta\sin\phi \qquad (4.2)$$

TM_{02} Mode:

$$E_\theta = +2C_0 \frac{e^{-jk_0 r}}{r} e^{jk_0 r_o \sin\theta\cos(\phi-\phi_0)} J_1(k_0 a_0 \sin\theta) \qquad (4.3)$$

$$E_\phi = 0 \qquad (4.4)$$

Where a_1 and a_0 are the radii of the TM_{11} and TM_{02} mode patches, respectively, and $(r_0, \phi_0, 0)$ is the location of the antenna center, as the two patches are concentric.

The combined far fields are:

$$E_\theta = -jC_1 e^{jk_0 r_o \sin\theta\cos(\phi-\phi_0)} \left\{ [J_0(u_1) - J_2(u_1)]\cos\phi + 2j\frac{C_0}{C_1} J_1(u_0) \right\} \frac{e^{-jk_0 r}}{r} \qquad (4.5)$$

$$E_\phi = jC_1 e^{jk_0 r_o \sin\theta\cos(\phi-\phi_0)} [J_0(u_1) + J_2(u_1)]\cos\theta\sin\phi \frac{e^{-jk_0 r}}{r} \qquad (4.6)$$

Where $\begin{Bmatrix} u_1 = k_0 a_1 \sin\theta \\ u_0 = k_0 a_0 \sin\theta \end{Bmatrix}$ and $\frac{C_0}{C_1}$ is the excitation ratio (TM_{02} to TM_{11}) and can be a complex number in general, $C_1 = |C_1| \angle \alpha_1$ and $C_0 = |C_0| \angle \alpha_0$.

If we look at the far fields at the $\phi = 0$ plane, the E_θ pattern will be due to the contributions of both TM_{11} and TM_{02} modes, while the E_ϕ pattern is zero. Therefore, we have considered the E_θ pattern for this study. Now, by changing the excitation ratio $\frac{C_0}{C_1}$ (both magnitude and phase), we can change the main beam direction and phase centre location. Figures 4.2 and 4.3 show the magnitude and phase of the E_θ pattern at the $\phi = 0$ plane, respectively, when the excitations are in-phase, $\alpha_1 - \alpha_0 = 0$, and the

antenna is located at the coordinate origin. They illustrate that, by increasing the absolute value of the excitation ratio, the peak radiation direction moves toward that of the pure TM_{02} mode, and the phase pattern is like that of the pure TM_{02} mode. They also show that for in-phase excitations, $\alpha_1 = \alpha_0$, the phase pattern for non-zero excitation ratios is no longer constant, implying that the location of the antenna phase centre has been moved. In order to have a constant phase distribution around the main beam, we must add a negative-slope phase term to the initial phase pattern as we did in chapter 3.

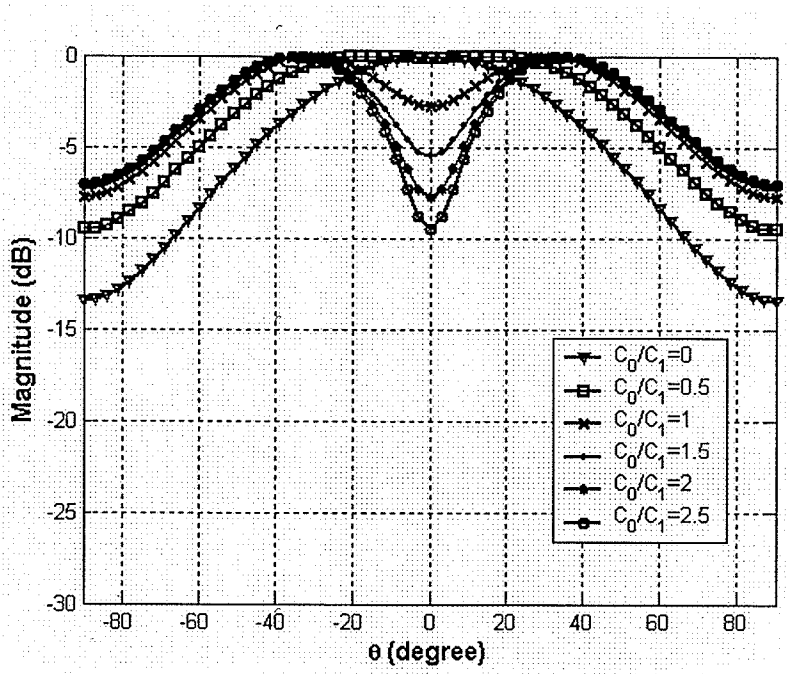

Fig. 4.2 Magnitude patterns of E_θ for combined TM_{11} and TM_{02} modes at $\phi = 0$ plane for different in-phase, $\alpha_1 = \alpha_0$, amplitude ratios for the antenna shown in Fig. 4.1, when it is located at the origin and both patches are fed along x-axis.

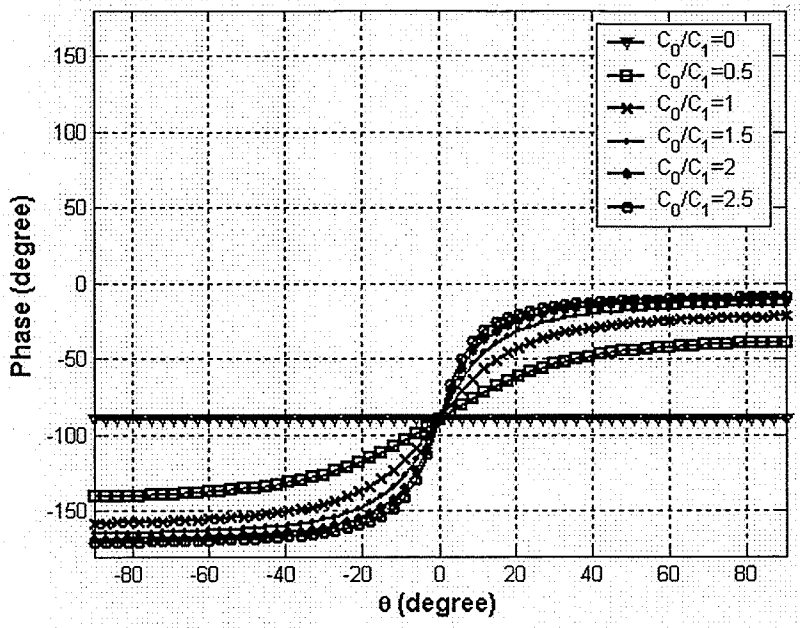

Fig. 4.3 Phase patterns of E_θ at $\phi = 0$ plane for different in-phase amplitude ratios for the antenna shown in Fig. 4.1, when it is located at the origin and both patches are fed along x-axis.

Now, let us consider out of phase excitations, $|\alpha_1 - \alpha_0| \leq 90^o$, of these two modes by assuming that α_1 and α_0 are the excitation phases for the TM_{11} and TM_{02} modes, respectively. As can be seen in Fig. 4.2, for the in-phase, $\alpha_1 = \alpha_0$, and non-zero amplitude excitations, there is a symmetric radiation pattern with two peaks one at $\phi = 0$ side and the other at $\phi = 180^o$ side (in the above figures, they have been illustrated by positive θ and negative θ, respectively). The out of phase excitation, $\alpha_1 \neq \alpha_0$, makes the radiation pattern to have only one peak, which depends on the sign of the phase difference in such a way that for positive $\alpha_1 - \alpha_0$, the main beam moves to positive θ, or $\phi = 0$ side, and for negative $\alpha_1 - \alpha_0$, the main beam moves to negative θ, or $\phi = 180^o$ side.

Figures 4.4 to 4.7 show the magnitude and phase of the E-plane patterns at $\phi = 0$ plane, when the two modes have an out of phase excitation and the excitation amplitude ratio is $\left(\frac{C_0}{C_1} = 0.5\right)$, while antennas are located at the coordinate origin. Again, the quadrature phase difference, $|\alpha_1 - \alpha_0| = 90^o$, makes the far field phase pattern uniform over the main beam, which pushes the phase centre location to the antenna center. The reason is that, for a 90° phase shift, the factor j for the TM_{11} mode is cancelled, as shown in equations 4.1 and 4.2. More details of the phase centre location and the main beam tilt angle will be discussed in the next section.

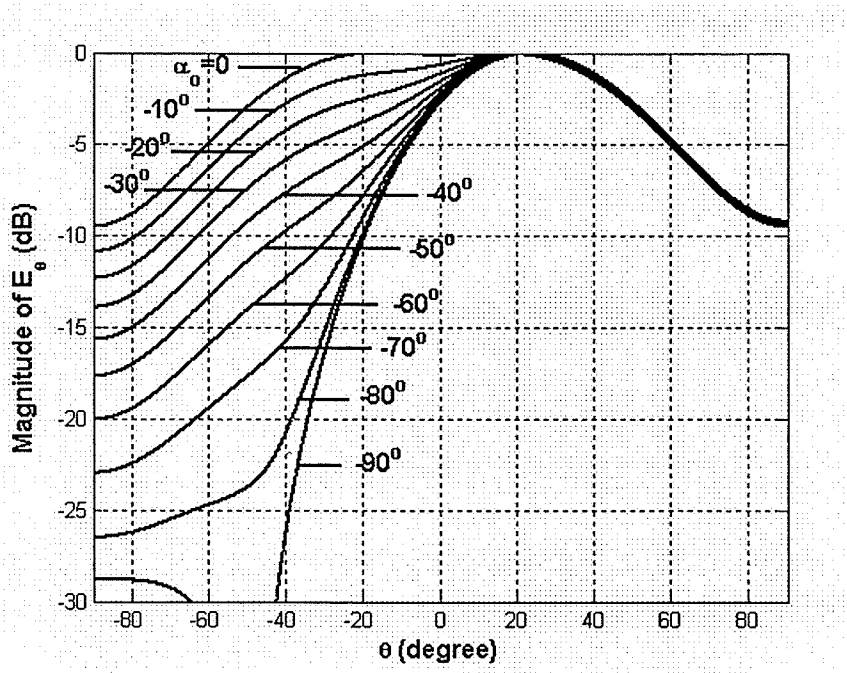

Fig. 4.4 Magnitude patterns of E_θ at $\phi = 0$ plane for different negative values of α_0 phase excitations, $\alpha_1 = 0$ and $\left|\frac{C_0}{C_1}\right| = 0.5$ for the antenna shown in Fig. 4.1, when it is located at the origin and both patches are fed along x-axis.

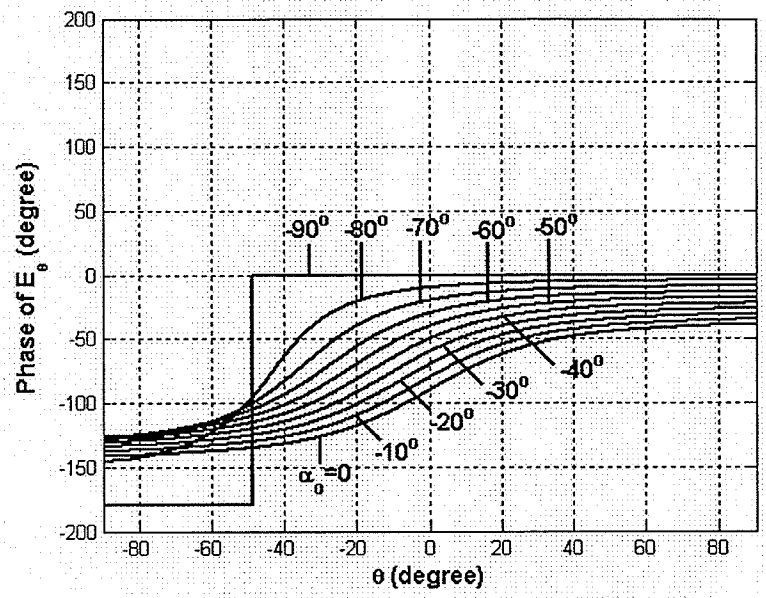

Fig. 4.5 Phase patterns of E_θ at $\phi = 0$ plane for different negative values of α_0 phase excitations, $\alpha_1 = 0$ and $\left|\frac{C_0}{C_1}\right| = 0.5$ for the antenna shown in Fig. 4.1, when it is located at the origin and both patches are fed along x-axis.

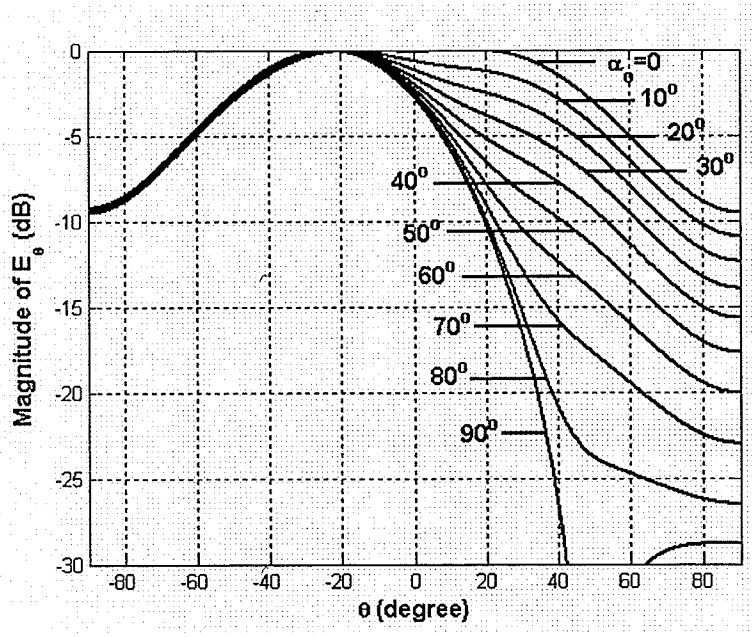

Fig. 4.6 Magnitude patterns of E_θ at $\phi = 0$ plane for different positive values of α_0 phase excitations, $\alpha_1 = 0$ and $\left|\frac{C_0}{C_1}\right| = 0.5$ for the antenna shown in Fig. 4.1, when it is located at the origin and both patches are fed along x-axis.

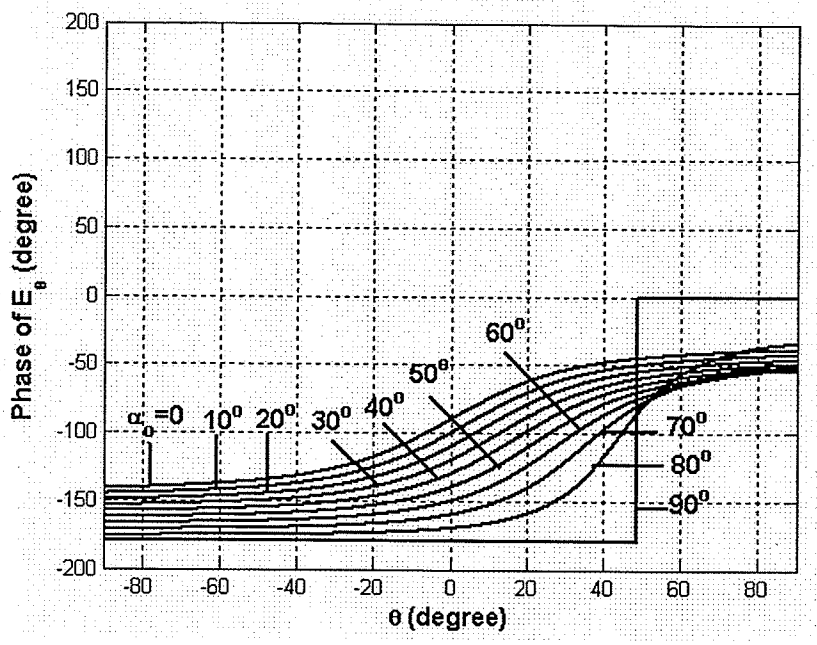

Fig. 4.7 Phase patterns of E_θ at $\phi = 0$ plane for different positive values of α_0 phase excitations, $\alpha_1 = 0$ and $\left|\frac{C_0}{C_1}\right| = 0.5$ for the antenna shown in Fig. 4.1, when it is located at the origin and both patches are fed along x-axis.

4.2.2 Phase centre location and main beam tilt angle

In this section, we study the phase centre of E_θ in the E-plane pattern of the antenna operating at TM_{11} and TM_{02} modes, since this plane shows the effects of both modes. The E_ϕ pattern is just due to the fundamental mode. Based on the discussion in section 3.2.1.2, the phase centre locus is a line passing through the point $(r_0, \phi_o = 180^o)$, and is parallel to the y-axis. As an example, let us consider the case of $\frac{C_0}{C_1} = 0.4\angle 0$. The phase centre of the E_θ patterns of the antenna is located on the solid line shown in Fig. 4.8, while it is passing though the point $(r_0 = 0.19\lambda, \phi_0 = 180^o)$.

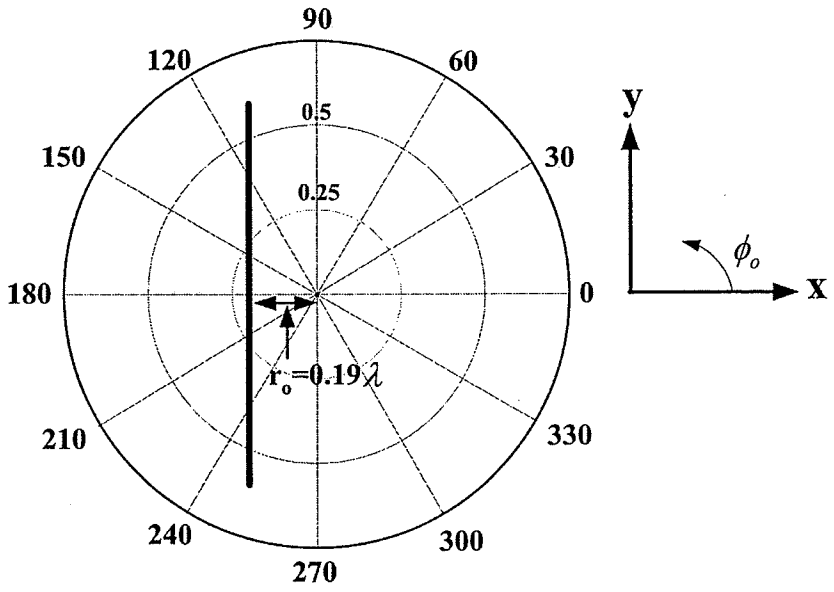

Fig. 4.8 The locus of phase centre of the E_θ patterns of the antenna shown in Fig. 4.1, with $\frac{C_0}{C_1} = 0.4\angle 0$, when both patches are fed along x-axis.

The effects of excitation amplitude ratio on the phase centre location and main beam tilt angle are shown in Figs. 4.9 and 4.10, respectively, for different excitation phases. As can be seen, for all excitation phases except for $|\alpha_1 - \alpha_0| = 90^o$ phase difference that keeps the phase centre at the coordinate origin, the phase centre moves away from the antenna center. The distance of the phase centre from the origin increases until the amplitude ratio of 0.45, beyond which it decreases. That is, the phase centre moves back to the origin as the amplitude of TM_{02} mode increases, and in the limit of pure TM_{02} mode, it returns to the coordinate origin. The main beam tilt also moves toward the TM_{02} mode peak direction. It is interesting to note that, for the in-phase excitation, $\alpha_1 = \alpha_0$, with the amplitude ratio up to 0.45, the main beam remains constant at the boresight angle, while the antenna phase centre moves away from the antenna center, leading to the virtual antenna concept.

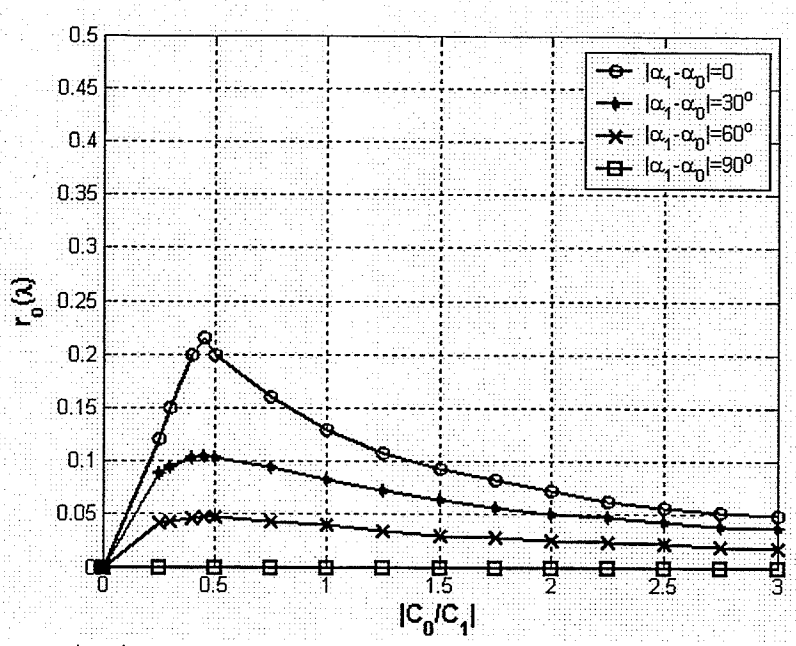

Fig. 4.9 Effect of $\left|\frac{C_0}{C_1}\right|$ *on phase centre location of* E_θ *at* $\phi = 0^o$ *plane for different excitation phases, over main beam, for the antenna shown in Fig. 4.1, when both patches are fed along x-axis while* $\phi_0 = 180^o$.

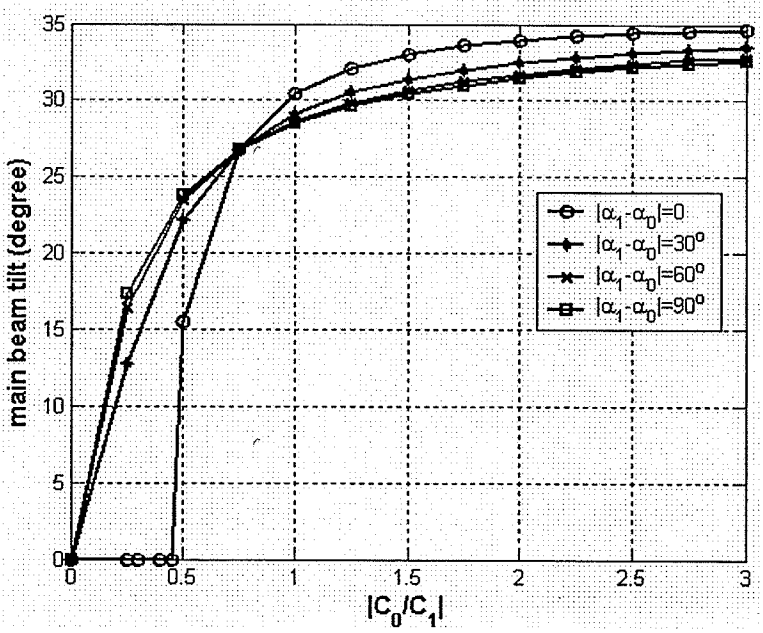

Fig. 4.10 Effect of $\left|\frac{C_0}{C_1}\right|$ *on main beam tilt angle for* E_θ *at* $\phi = 0^o$ *plane for different excitation phases of the antenna shown in Fig. 4.1, when both patches are fed along x-axis while* $\phi_0 = 180^o$.

The effects of the excitation phase difference on the phase centre location and main beam tilt angle were also studied, which are shown in Fig 4.11 and 4.12, respectively, for certain excitation amplitude ratios. They show that, the phase centre converges to the center of the antenna for the quadrature phase difference, $\alpha_1 - \alpha_0 = 90^o$. The main beam direction is almost constant, over all excitation phases, when the amplitude ratio is equal or greater than 0.75, while the phase centre location changes. For the amplitude ratio equal to 0.25, the main beam is along the boresight, and increases with higher excitation phases.

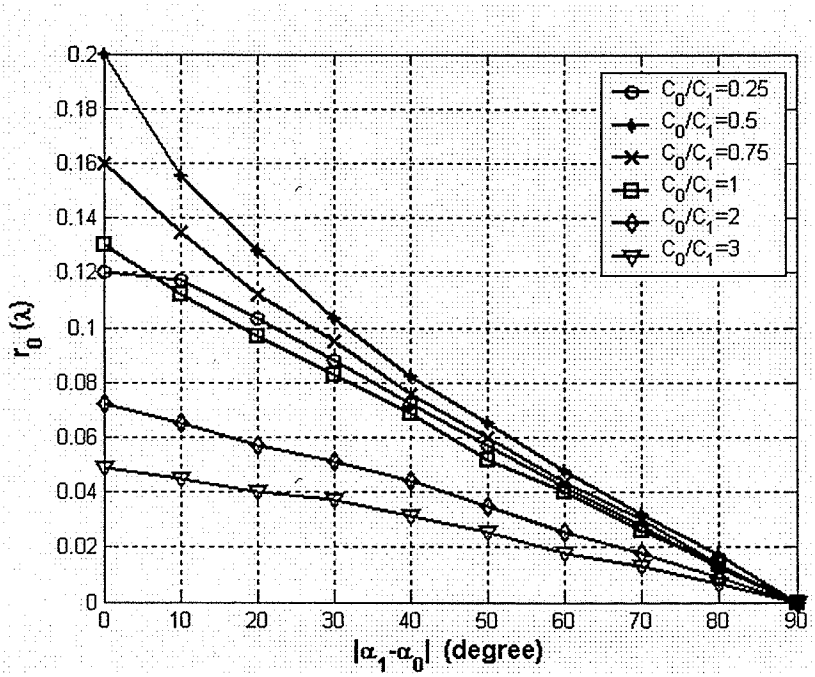

Fig. 4.11 Phase centre location of E_θ at $\phi = 0$ plane versus excitation phases for different $\left|\frac{C_0}{C_1}\right|$, over main beam, for the antenna shown in Fig. 4.1, when both patches are fed along x-axis while $\phi_0 = 180^o$.

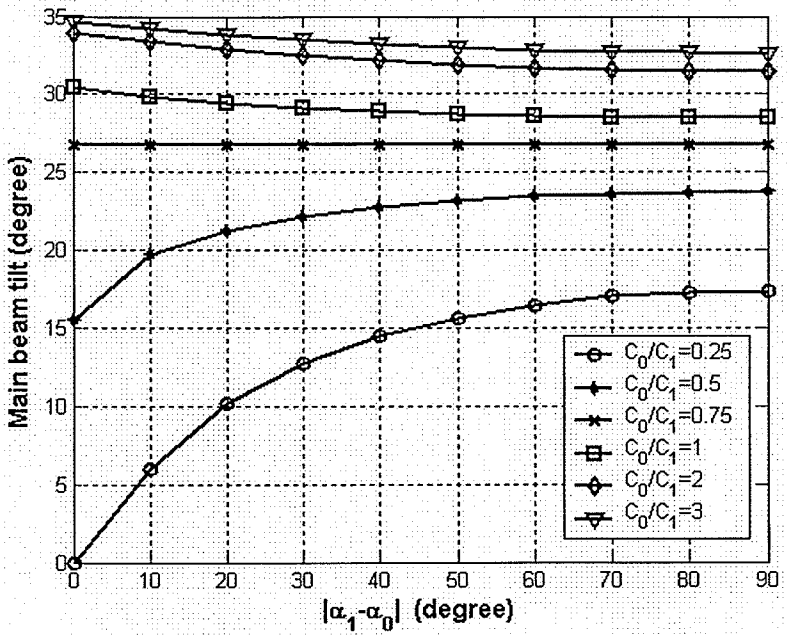

Fig. 4.12 Main beam tilt angle of E_θ at $\phi = 0$ plane versus excitation phases for different $\left|\frac{C_0}{C_1}\right|$*, for the antenna shown in Fig. 4.1, when both patches are fed along x-axis while*

$$\phi_0 = 180^\circ.$$

4.2.3 Polarization properties

Based on equations 4.5 and 4.6, the electric field for the antenna under study is an x-polarized field, so we can use Ludwig's third definition for the x-aligned field as expressed in equation 3.8.

Similarly, there will be a global phase centre for the antenna operating at TM_{11} and TM_{02} modes, as discussed in chapter 3, section 3.2.13. For this antenna, such a phase centre is located at $\phi_0 = 180^\circ$ for excitation amplitude ratio less than 0.45. The effect of amplitude excitation ratio on the phase centre location of the copolar radiation pattern is shown in Fig. 4.13. Again, there will be a multiple phase centres beyond the excitation

amplitude ratios shown in Fig. 4.13. The reason is that, the peak radiation directions of E- and H-plane patterns will not be the same at all ϕ-planes for $C_0/C_1>0.45$.

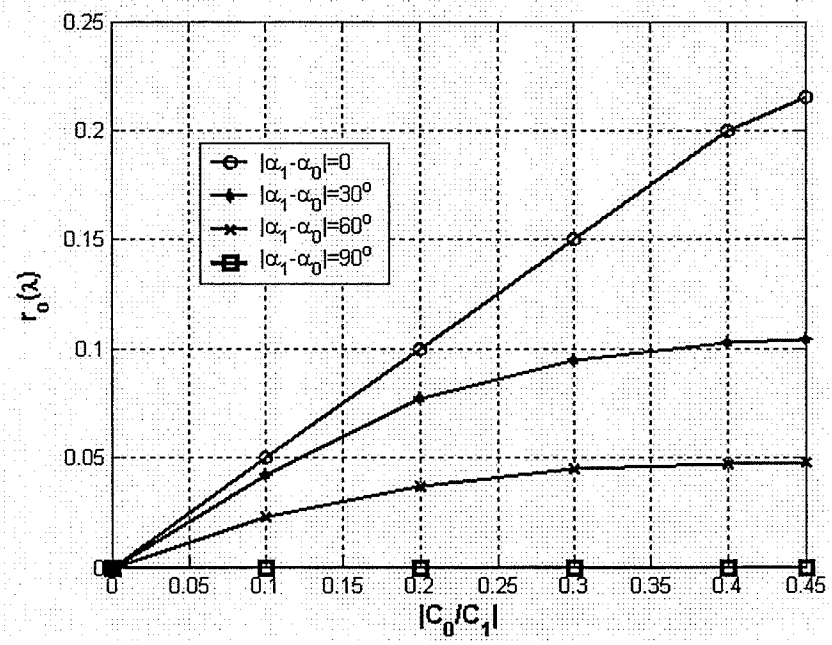

Fig. 4.13 Effect of $\left|\frac{C_0}{C_1}\right|$ *on phase centre of copolar radiation pattern of the antenna shown in Fig. 4.1, when* $\phi_0 = 180^o$ *over main beam.*

The copolar and crosspolar patterns at different ϕ-planes are as below:

- At $\phi = 0$ plane:
$$\left\{\begin{matrix} E_{co}\,|_{\phi=0} = E_\theta\,|_{\phi=0} \\ E_{xpol}\,|_{\phi=0} = E_\phi\,|_{\phi=0} = 0 \end{matrix}\right\} \qquad (4.7)$$

- At $\phi = 90^o$ plane:
$$\left\{\begin{matrix} E_{co}\,|_{\phi=90^o} = -E_\phi\,|_{\phi=90^o} \\ E_{xpol}\,|_{\phi=90^o} = E_\theta\,|_{\phi=90^o} \end{matrix}\right\} \qquad (4.8)$$

- At $\phi = 45^o$ plane:

$$\left\{\begin{matrix} E_{co}\,|_{\phi=45^o} = \left(\cos\phi\, E_\theta - \sin\phi\, E_\phi\right)|_{\phi=45^o} \\ E_{xpol}\,|_{\phi=45^o} = \left(\sin\phi\, E_\theta + \cos\phi\, E_\phi\right)|_{\phi=45^o} \end{matrix}\right\} \qquad (4.9)$$

As can be seen, at $\phi = 0$ plane, the crosspolarization is zero since E_ϕ for both modes vanishes on this plane. Figure 4.14 shows the copolar and crosspolar pattern at $\phi = 90^o$ plane for different mode excitation ratios.

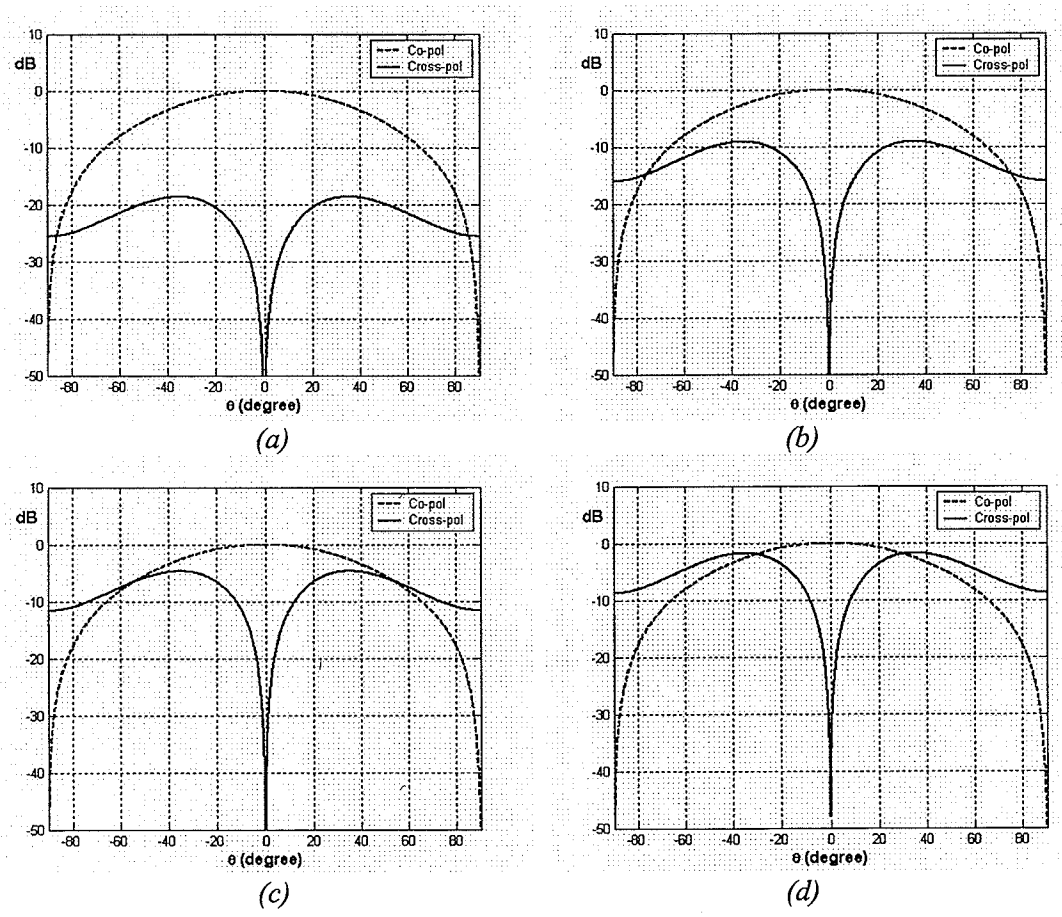

Fig. 4.14 Normalized copolar and crosspolar components at $\phi = 90^o$ plane of the antenna shown in Fig. 4.1, when both patched are fed along x-axis

(a) $\frac{C_0}{C_1} = 0.1\angle 0$, *(b)* $\frac{C_0}{C_1} = 0.3\angle 0$, *(c)* $\frac{C_0}{C_1} = 0.5\angle 0$, *(d)* $\frac{C_0}{C_1} = 0.7\angle 0$

Crosspolarization at $\phi = 90^o$ plane is mainly due to E_θ of TM_{02} mode and it increases with higher mode ratio as illustrated at Fig. 4.14. At $\phi = 45^o$ plane, both TM_{11} and TM_{02} modes contribute to the crosspolarization patterns, as shown in Fig. 4.15. The normalized crosspolar to copolar levels versus excitation amplitude ratio are plotted in Figs. 4.16 and

4.17 at $\phi = 90^o$ and $\phi = 45^o$ planes, respectively. They show that, at both planes, the crosspolarization is lower for small excitation amplitude ratios since by increasing this ratio, the effect of TM_{02} mode increases and the crosspolarization level increases.

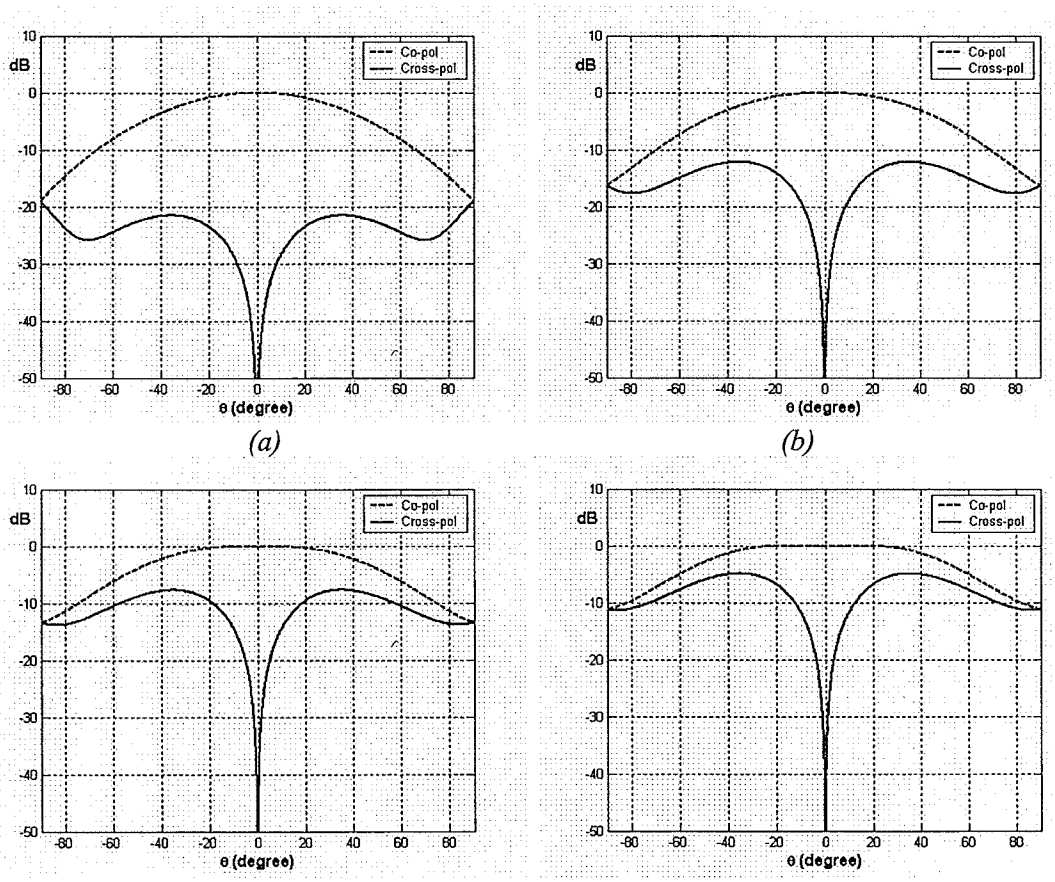

Fig. 4.15 Normalized copolar and crosspolar components at $\phi = 45^o$ plane of the antenna shown in Fig. 4.1, when both patched are fed along x-axis

(a) $\frac{C_0}{C_1} = 0.1\angle 0$, *(b)* $\frac{C_0}{C_1} = 0.3\angle 0$, *(c)* $\frac{C_0}{C_1} = 0.5\angle 0$, *(d)* $\frac{C_0}{C_1} = 0.7\angle 0$

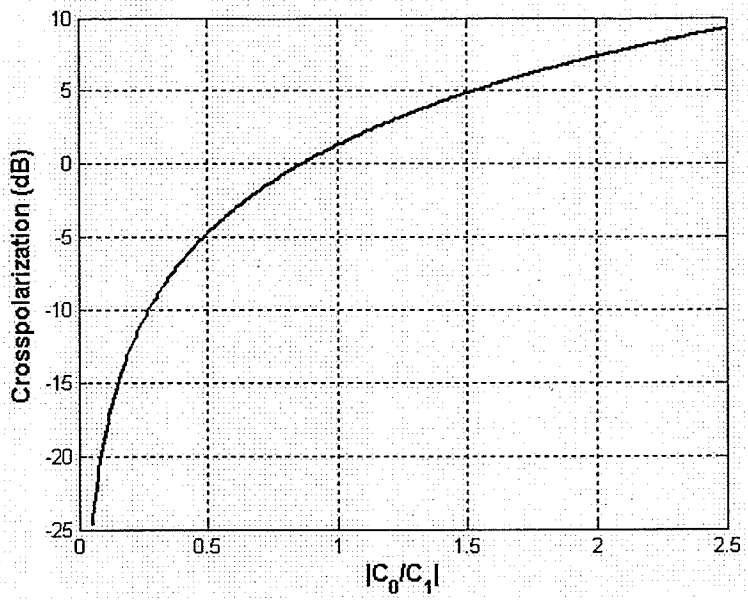

Fig. 4.16 Normalized crosspolar to copolar level versus amplitude excitation $\left|\frac{C_0}{C_1}\right|$ *at* $\phi = 90^o$ *plane of the antenna shown in Fig. 4.1, when both patches are fed along x-axis and* $\alpha_1 = \alpha_0$.

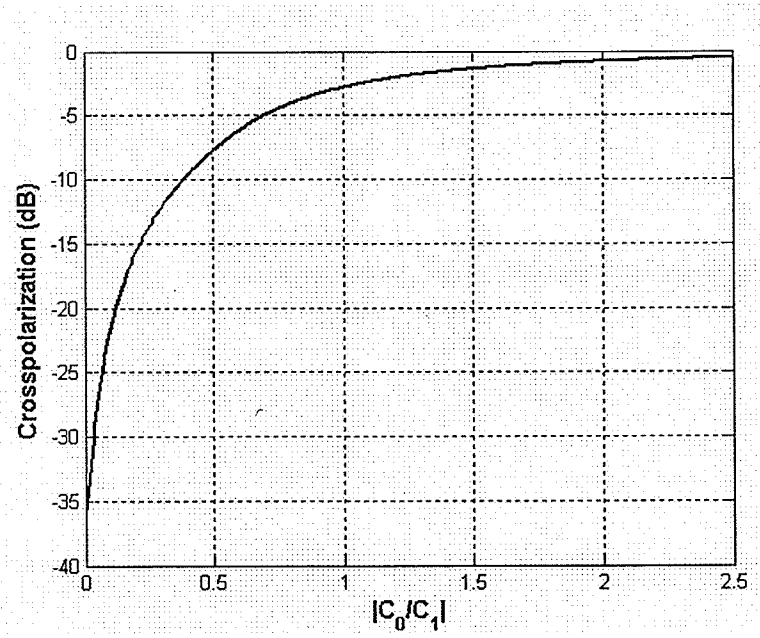

Fig. 4.17 Normalized crosspolar to copolar level versus amplitude excitation $\left|\frac{C_0}{C_1}\right|$ *at* $\phi = 45^o$ *plane of the antenna shown in Fig. 4.1, when both patches are fed along x-axis and* $\alpha_1 = \alpha_0$.

4.3 Design Example

In order to verify the above analytical results, a two-layer antenna was designed by Ansoft Designer package version 2, which is based on a Method of Moment. The geometry of the antenna is shown in Fig. 4.18. A stack configuration of two patches has been used, in an ascending order from TM_{11} to TM_{02} patches, over a finite ground plane to design a practical antenna. One type substrate was used for both layers with $\varepsilon_r = 1.15$. The dielectric thicknesses for TM_{11} and TM_{02} modes are 1.5mm and 3mm, respectively. The operating frequency is 10GHz. The finite ground plane was considered since it can be fabricated practically.

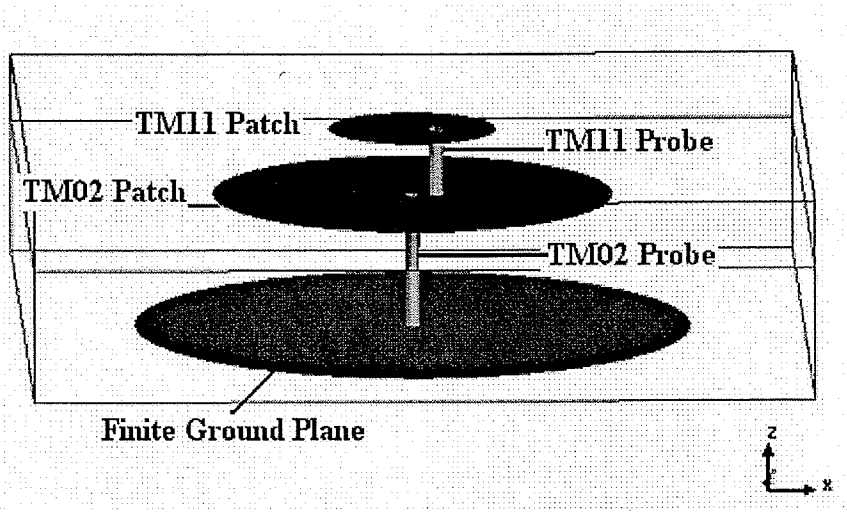

Fig. 4.18 The geometry of stacked patches operating at TM_{11} and TM_{02} modes over a finite ground plane

$$a_{TM11} = 7.52mm,\ a_{TM02} = 18mm,\ a_{ground} = 25mm$$
$$\rho_f^{TM11} = 2.16mm\ ,\quad \phi_m^{TM11} = 0$$
$$\rho_f^{TM02} = 0mm\ ,\quad \phi_m^{TM02} = 0$$
$$h_1 = 1.5mm,\ h_2 = 3mm,\ \varepsilon_r = 1.15$$

Two individual probes were used to excite the antenna, one for the TM_{11} mode and another for TM_{02} mode. The feed location was optimized in order to excite each

mode properly, based on the discussion in chapter 2, section 2.2.3, and to have a good impedance match condition at 10GHz. The scattering parameters of the antenna are shown in Fig. 4.19. As can be seen, the return losses for both ports are well below -10dB at 10GHz, which provides good impedance matches, while the coupling between the two ports is about -18dB at the frequency of operation.

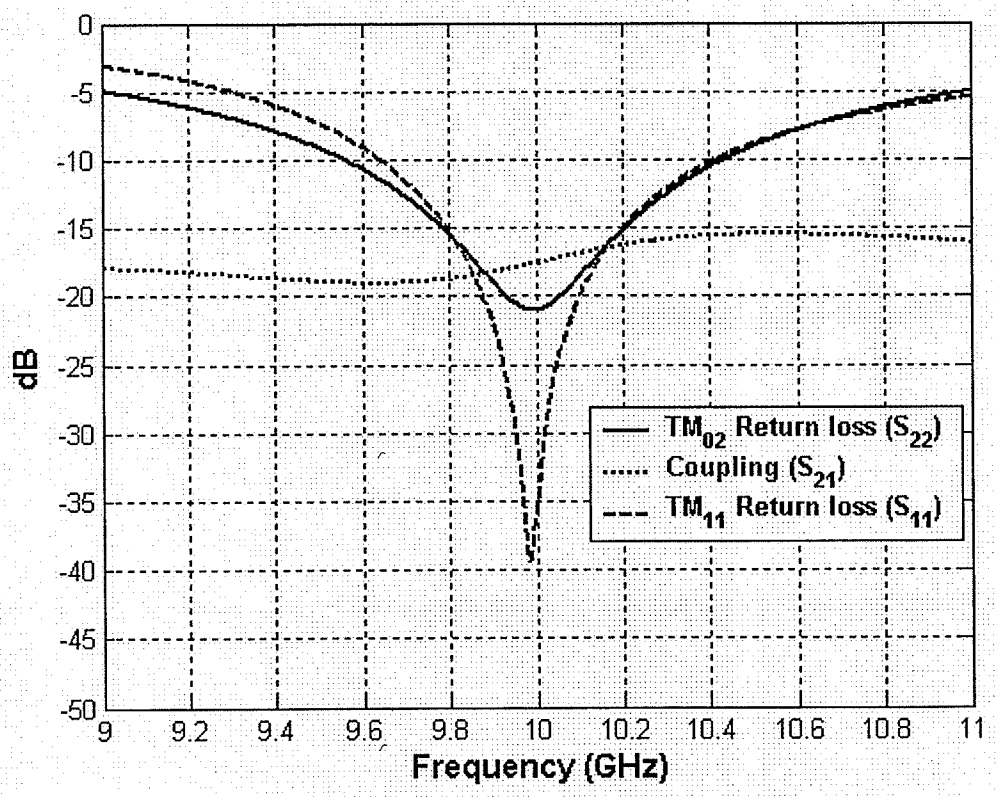

Fig. 4.19 Scattering parameters of stacked patch antenna in Fig.4.18 operating at TM_{11} and TM_{02} modes over a finite ground plane.

As is known, a probe feed introduces phase shift in real situation. In the present simulations such phase shifts will be automatically included in the results and will alter the required phase shift between the two modes in investigation of the phase centre

locations. In order to compare the current numerical results with previous analytical ones in equation 4.5, we must determine the relationship between the mode constants, C_n, and V_n, as well as the phase shift values for each probe. Based on equation 2.14, $V_n = \frac{2C_n}{a_n k_0}$, thus, if $C_1 = C_0$ and $\alpha_1 = \alpha_0$:

$$\frac{V_1}{V_0} = \frac{a_0}{a_1} = \frac{\chi'_{02}}{\chi'_{11}} = \frac{3.8317}{1.841} = 2.0813 \quad (4.10)$$

Under a good impedance match condition, one can easily convert the above voltages into the currents, based on the discussion in section 3.2.2. Therefore, the amplitude of currents for each mode will be $|I_{TM11}| = 104mA, |I_{TM02}| = 50mA$. Now, we have to choose proper phase for each mode to cancel the probe phase shift. These values are $\angle I_{TM11} = 55^o$, $\angle I_{TM02} = 105^o$. They were chosen to make the analytical and numerical phase distributions identical as shown in Fig. 4.21 and Fig. 4.24. It means, the identical mode coefficients, C_1=C_0 and $\alpha_1 = \alpha_0$, in the analytical approach correspond to the following current excitations in numerical simulations, as shown in table 4.1:

$$I_{TM11} = 104mA\angle 55^o, I_{TM02} = 50mA\angle 105^o \quad (4.11)$$

Excitation Ratio	Amplitude	Phase (degrees)
Analytical $(\frac{C_0}{C_1})$	**1**	**0**
Numerical $(\frac{I_{TM02}}{I_{TM11}})$	**0.48**	**+50°**

Table 4.1 Relation between excitation ratios C_0/C_1 in analytical method (Fig. 4.1) and current excitation ratios I_0/I_1 in numerical method (Fig. 4.18) for the stacked patch antenna operating at TM_{11} and TM_{02} modes, when both patches are fed along x-axis.

As we are interested in having antennas with broadside radiation patterns, but phase centres away from the origin, we present two cases, with excitation amplitude ratios of 0.4 and 0.25. The phase centre movement is in good agreement with analytical one. Figures 4.20 and 4.21 show the magnitude and phase of E_θ pattern of the antenna, when located at the coordinate origin and has an amplitude ratio of 0.4. Figure 4.22 gives the phase pattern after displacing the whole antenna to $\left(r_o = 0.19\lambda, \phi_o = 180^o\right)$. Figures 4.23 to 4.25 show the same properties as above for a quarter amplitude ratio. This time, the phase centre goes to $\left(r_o = 0.125\lambda, \phi_o = 180^o\right)$.

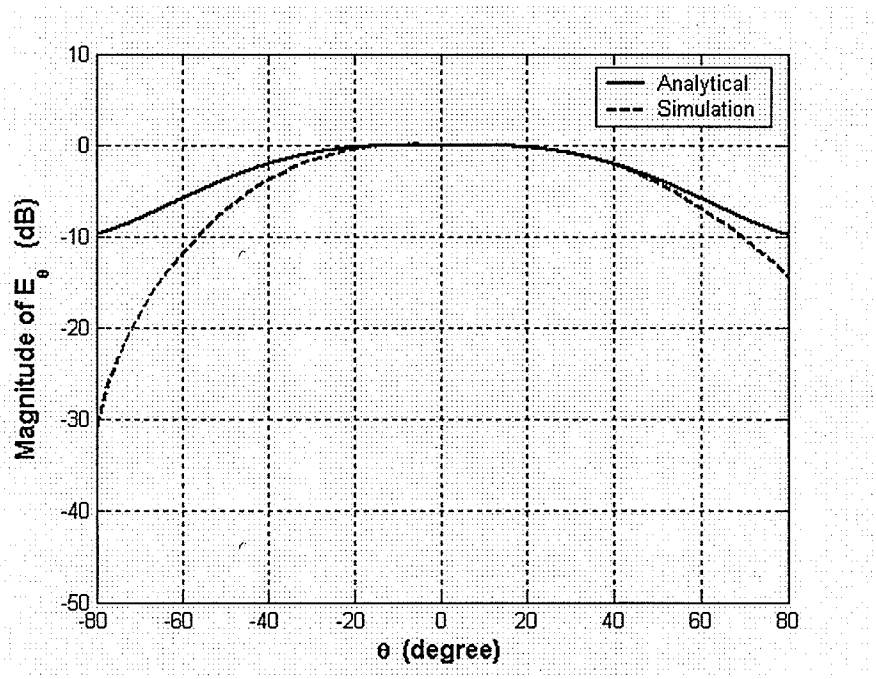

Fig. 4.20 Magnitude pattern of E_θ at $\phi = 0$ plane for the antenna shown in Fig. 4.18, when both patches are fed along x-axis and located at the origin, $\left(C_0 / C_1 = 0.4\angle 0\right)$

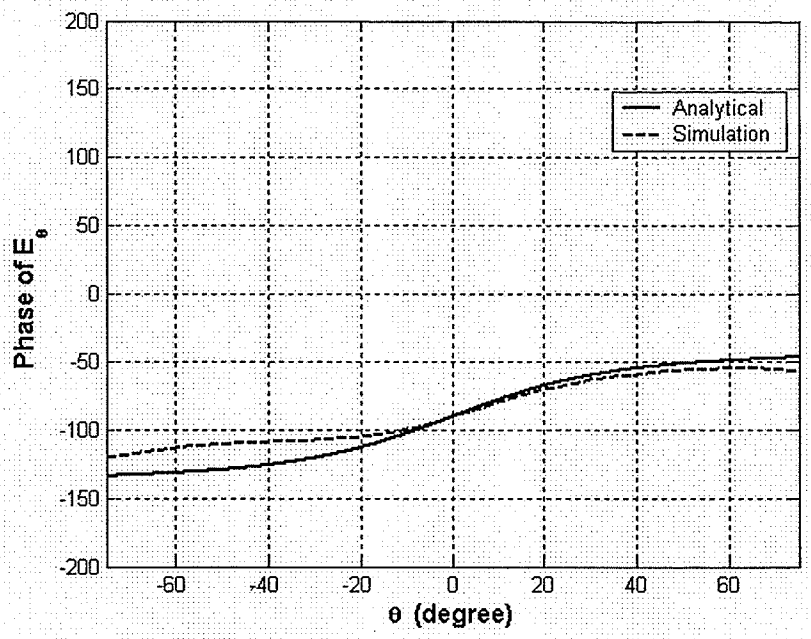

Fig. 4.21 Phase pattern of E_θ at $\phi = 0$ plane for the antenna shown in Fig. 4.18, when both patches are fed along x-axis and located at the origin, $(C_0 / C_1 = 0.4\angle 0)$.

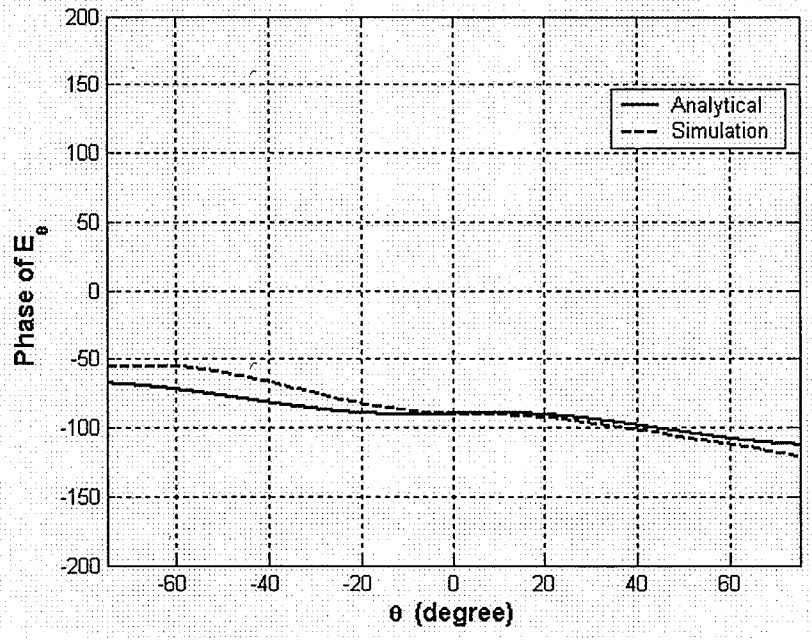

Fig. 4.22 Phase pattern of E_θ at $\phi = 0$ plane for the antenna shown in Fig. 4.18, when both patches are fed along x-axis $(r_0 = 0.19\lambda, \phi_0 = 180^o)$ and $(C_0 / C_1 = 0.4\angle 0)$.

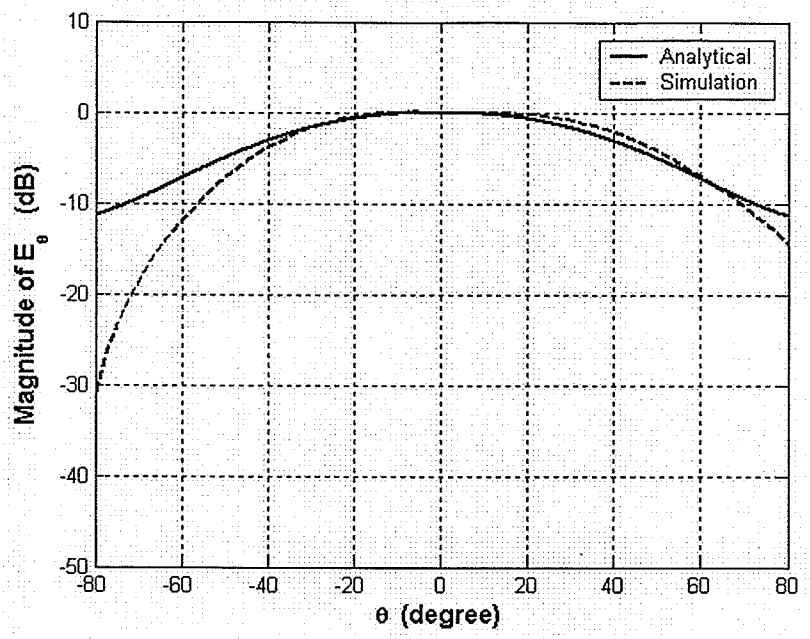

Fig. 4.23 Magnitude pattern of E_θ at $\phi = 0$ plane for the antenna shown in Fig. 4.18, when both patches are fed along x-axis, $(C_0 / C_1 = 0.25\angle 0)$.

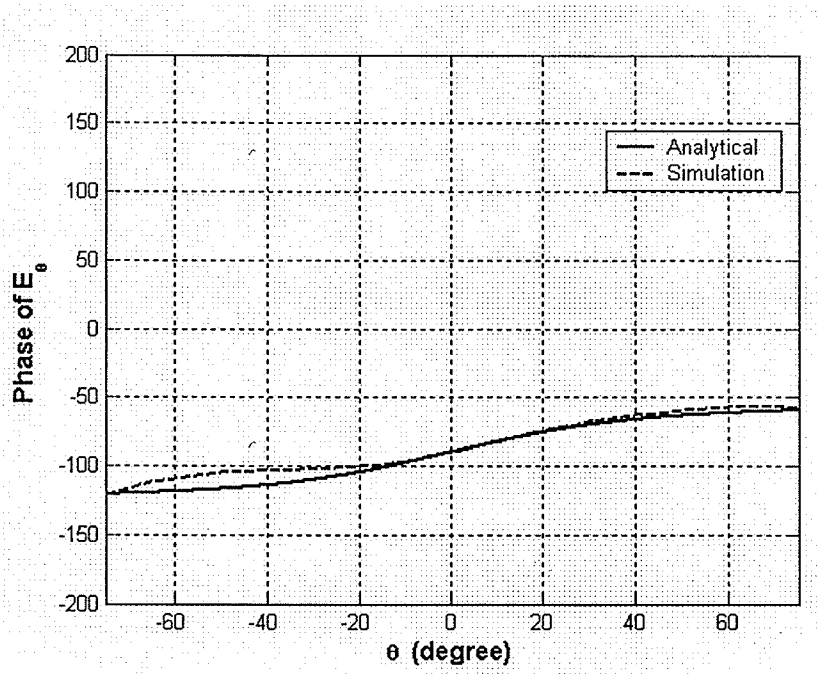

Fig. 4.24 Phase pattern of E_θ at $\phi = 0$ plane for the antenna shown in Fig. 4.18, when both patches are fed along x-axis and located at the origin, $(C_0 / C_1 = 0.25\angle 0)$.

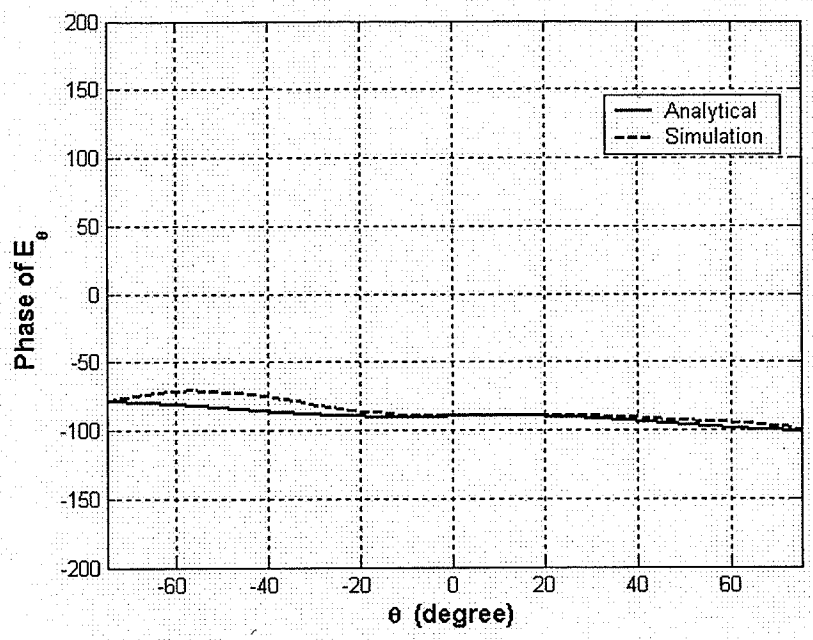

Fig. 4.25 Phase pattern of E_θ at $\phi = 0$ plane for the antenna shown in Fig. 4.18, when both patches are fed along x-axis and the antenna center moved to $(r_0 = 0.12\lambda, \phi_0 = 180^o)$ with $(C_0 / C_1 = 0.25\angle 0)$.

Figure 4.26 and 4.27 show the copolar and crosspolar radiation patterns at $\phi = 45^0$ and $\phi = 90^0$ planes for the above two different amplitude ratios. As can be seen, the crosspolarization at $\phi = 45^0$ plane, does not have a symmetric pattern. The reason is that, due to the finite size of ground plane, the peaks of the E_θ and E_ϕ patterns may happen at the different directions which lead to asymmetric crosspolarizations. By reducing the ground plane size to less than 0.8λ [10] (the antenna under study has a ground plane with diameter 1.67λ) one may obtain symmetric copolar radiation patterns, which in turn will give symmetric crosspolarization. This may be achieved by increasing the dielectric constant of the substrate, which reduces the size of each patch and, thus, the ground plane

size can be reduced. However, the amount of asymmetry comparing to the antenna of case I in chapter 3 is considerably lower.

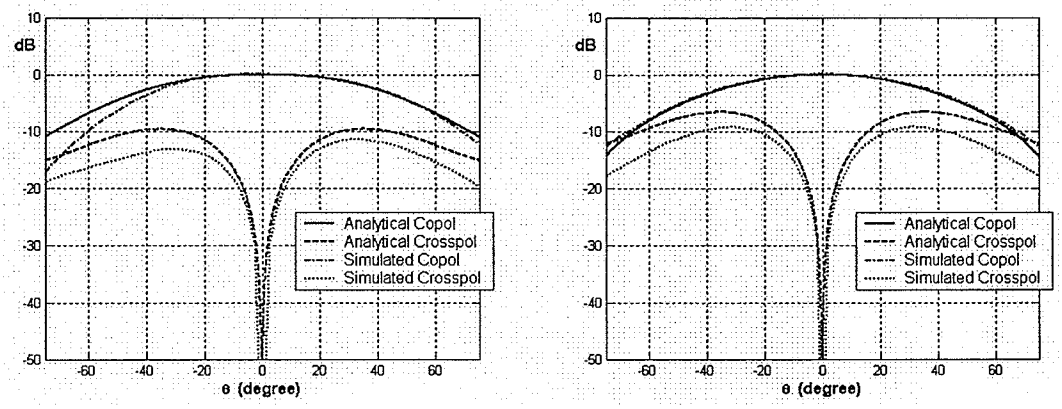

(a) *(b)*

Fig. 4.26 Normalized copolar and crosspolar radiation patterns of the antenna shown in Fig. 4.18, when both patches are fed along x-axis, $(C_0 / C_1 = 0.4\angle 0)$ *at (a)* $\phi = 45^o$, *(b)* $\phi = 90^o$

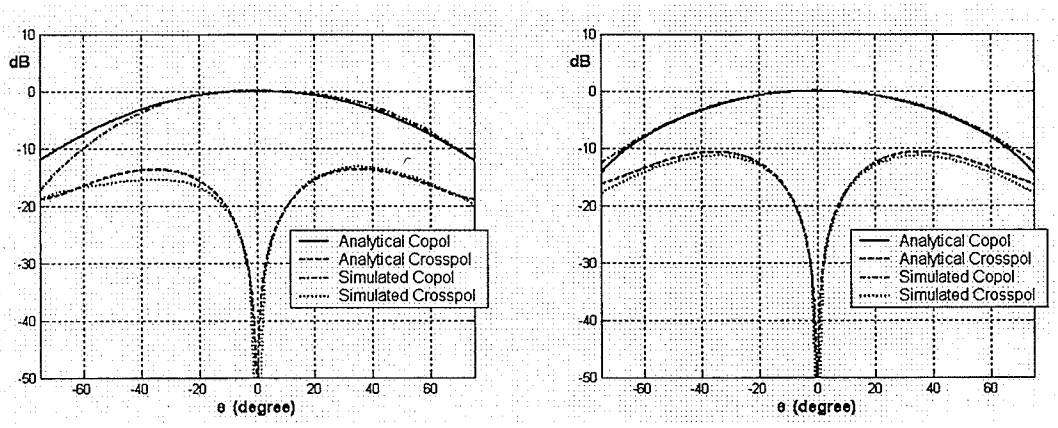

(a) *(b)*

Fig. 4.27 Normalized copolar and crosspolar radiation patterns of the antenna shown in Fig. 4.18, when both patches are fed along x-axis, $(C_0 / C_1 = 0.25\angle 0)$ *at (a)* $\phi = 45^o$, *(b)* $\phi = 90^o$

The normalized crosspolarization level of the designed antenna is almost similar to what was obtained from analytical one. The case with higher dielectric constants, which makes the crosspolar pattern symmetric, will be discussed in the next chapter.

4.4 Summary

In this chapter, the phase centre location, main beam tilt angle and polarization of TM_{11} and TM_{02} modes, when used as a single stacked antenna, were studied both analytically and numerically for a practical design example. Due to the central feeding of the TM_{02} patch, just one case was considered when the feeds are located along the x-axis. There was a good agreement between analytical results, using the cavity model, and numerical results based on the Method of Moment, except due to the finite ground plane size, the crosspolarization pattern at $\phi = 45^{o}$ plane is somewhat asymmetric. Again, adding the higher order TM_{02} mode to the fundamental mode resulted in higher crosspolarization and multiple phase centres.

It was shown that, there is a global phase centre location when the copolar radiation pattern is considered. The antenna can be assumed as an x-polarized field, when both TM_{11} and TM_{02} patches are fed along the x-axis. This antenna was found to have a global phase centre location at $\phi_0 = 180^{o}$, for excitation amplitude ratio less than 0.45.

Chapter 5

Stacked Patch Circular Microstrip Antenna operating at TM_{11}, TM_{21} and TM_{02} modes

5.1 Introduction

In this chapter, a three-layer circular microstrip patch antenna is studied. The lower patch operates at TM_{02} mode, which has a circularly symmetrical pattern with a null at broadside. The middle patch generates TM_{21} mode, and also has a boresight-nulled radiation pattern. And, the upper patch produces TM_{11} mode which has a broadside radiation pattern. This structure is first treated analytically to better understand its properties. For simplicity, the ground plane of the antenna is assumed to be infinite in size and the mutual couplings between its three ports are neglected. The analysis again is based on the cavity model. In order to verify the results, the same structure is then designed with a finite ground plane and simulated by Ansoft Designer version 2, based on a Method of Moment. The case when all feeds are located along the x-axis is considered in which the phase centre location, main beam tilt angle, and crosspolarization properties are studied in terms of the amplitude ratio and phase difference between the three modes. It will be shown that, one can decrease the crosspolarization of the antenna and keep the phase centre location unchanged by properly exciting the TM_{11}, TM_{21}, and TM_{02} modes.

5.2 Analytical model

5.2.1 Radiation amplitude and phase patterns

In this section, we have developed a Matlab program to calculate the far field radiation patterns based on the cavity model, which was formulated in chapter 2. Thus, the entire antenna is over an infinite ground plane and mutual couplings between the three ports are neglected. However, in the design example using numerical simulations, these effects are automatically included. All patches are fed along the x-axis as shown in Fig. 5.1. The antenna was designed to resonate at 10GHz. The patch sizes were determined using equations 2.8 to 2.11.

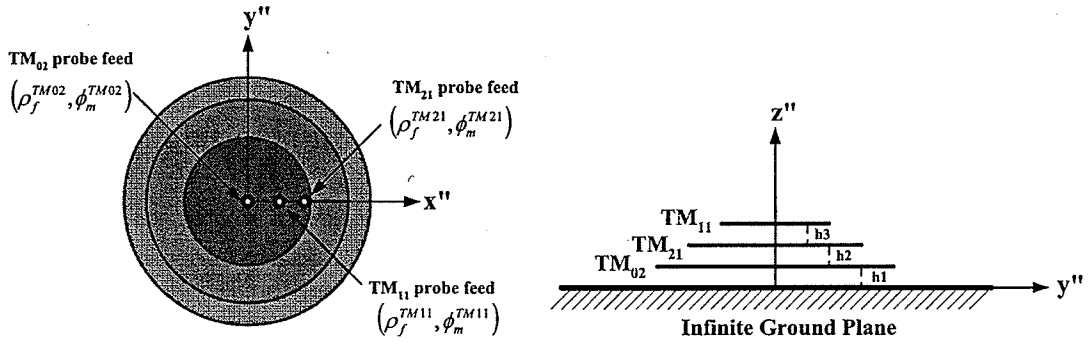

Fig. 5.1 (a) Top view (b) cross-section view of a stacked patch microstrip antenna operating at TM_{11}, TM_{21} and TM_{02} modes when all patches are fed along x-direction $h_1 = h_2 = h_3 = 1.5mm$, $a_{TM11} = 5.1mm$, $a_{TM21} = 9mm$, $a_{TM02} = 11.2mm$, $\varepsilon_r = 2.32$ *and f=10GHz.*

As mentioned earlier, in order to obtain the symmetric patterns, which in turn results in a symmetric crosspolarization patterns, one may decrease the ground plane size. Therefore, we selected a higher dielectric constant for the antenna in this chapter in order to have smaller antenna dimensions. All layers have the same thickness, 1.5mm, and are

etched on a similar substrate with $\varepsilon_r = 2.32$. However, some results will be shown at the lower dielectric constant of 1.15, the same as used in chapters 3 and 4, for the sake of comparison. Again, the effect of substrate thickness on the phase distribution is neglected based on the discussion in chapter 2, section 2.2.2. For the TM_{11}, TM_{21} and TM_{02} modes, using equations 2.12, 2.13 and 2.14, the total far fields in spherical coordinates, with the patch centers at (r_o, ϕ_o,0), can be expressed as,

$$E_\theta = -jC_1 e^{jk_0 r_o \sin\theta\cos(\phi-\phi_0)}\left\{[J_0(u_1) - J_2(u_1)]\cos\phi + j\frac{C_2}{C_1}[J_1(u_2) - J_3(u_2)]\cos 2\phi + 2j\frac{C_0}{C_1}J_1(u_0)\right\}\frac{e^{-jk_0 r}}{r} \quad (5.1)$$

$$E_\phi = jC_1 e^{jk_0 r_o \sin\theta\cos(\phi-\phi_0)}\left\{[J_0(u_1) + J_2(u_1)]\sin\phi + j\frac{C_2}{C_1}[J_1(u_2) + J_3(u_2)]\sin 2\phi\right\}\cos\theta\frac{e^{-jk_0 r}}{r} \quad (5.2)$$

Where $\begin{Bmatrix} u_1 = k_0 a_1 \sin\theta \\ u_2 = k_0 a_2 \sin\theta \\ u_0 = k_0 a_0 \sin\theta \end{Bmatrix}$, C_1, C_2 and C_0 are the excitation coefficients corresponding to the TM_{11}, TM_{21} and TM_{02} modes, respectively and they are complex numbers in general, $C_1 = |C_1|\angle\alpha_1$, $C_2 = |C_2|\angle\alpha_2$ and $C_0 = |C_0|\angle\alpha_0$.

If we look at the far fields at $\phi = 0$ plane, the E_θ pattern will be the contribution of all three modes, while the E_ϕ pattern will be zero. Therefore, we considered E_θ in the E-plane for this case. Now, by changing the excitation coefficients (both magnitude and phase) we can change the main beam direction and phase centre location, as before. Figures 5.2 and 5.3 show the magnitude and phase of the E_θ pattern at $\phi = 0$ plane, respectively, when all excitation coefficients are in-phase, $\alpha_1 = \alpha_2 = \alpha_0$, and the antenna is located at the coordinate origin. It illustrates that, by increasing these factors, the peak radiation direction moves toward the endfire direction and the phase pattern is almost constant over each beam. It also shows that, for in-phase excitations, the phase

pattern, for non-zero excitation ratio, is no longer constant, which implies that, the location of the antenna phase centre is changed. In order to have a constant phase distribution around the main beam, we must add a phase term having appropriate slope to the initial phase pattern. These figures show the amplitude and phase patterns for different TM_{02} excitation coefficient, C_0, at a given TM_{21} to TM_{11} excitation ratio, $\frac{C_2}{C_1}$.

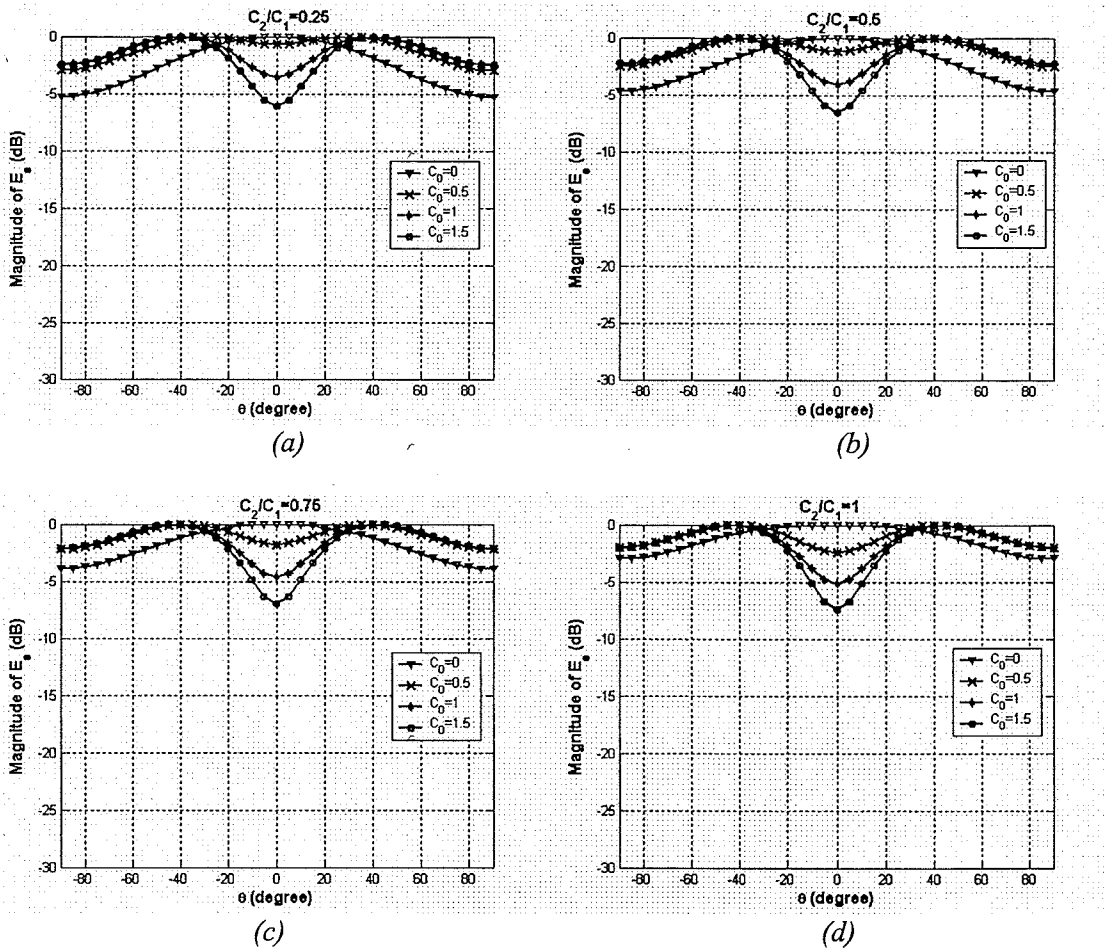

Fig. 5.2 Magnitude patterns of E_θ at $\phi = 0$ plane for different C_0, of the antenna shown in Fig. 5.1, when it is located at the origin and all patches are fed along x-axis with in-phase excitations, $\alpha_1 = \alpha_2 = \alpha_0$.

(a) $\frac{C_2}{C_1} = 0.25$ *(b)* $\frac{C_2}{C_1} = 0.5$

(c) $\frac{C_2}{C_1} = 0.75$ *(d)* $\frac{C_2}{C_1} = 1$

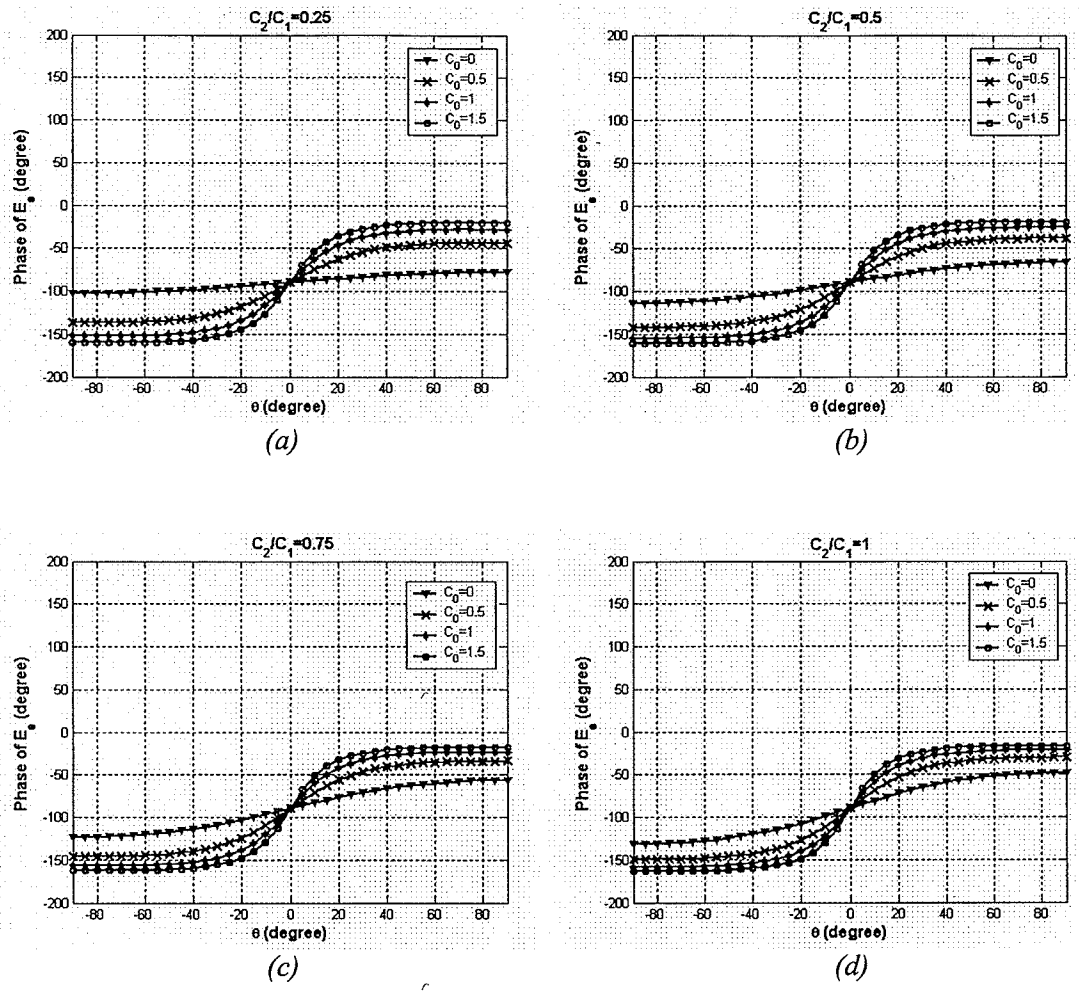

Fig. 5.3 Phase patterns of E_θ at $\phi = 0$ plane for different C_0, of the antenna shown in Fig. 5.1, when it is located at the origin and all patches are fed along x-axis with in-phase excitations,

$$\alpha_1 = \alpha_2 = \alpha_0 .$$

(a) $\frac{C_2}{C_1} = 0.25$ *(b)* $\frac{C_2}{C_1} = 0.5$

(c) $\frac{C_2}{C_1} = 0.75$ *(d)* $\frac{C_2}{C_1} = 1$

Now, let us consider out of phase excitations, $|\alpha_1 - \alpha_2| \leq 90^o$ and $0 \leq \alpha_o \leq 90^o$, of these three modes by assuming that, α_1, α_2 and α_0 are the excitation phases for TM_{11}, TM_{21} and TM_{02} modes, respectively. As shown in Fig. 5.2, for non-zero in-phase excitations, there is a symmetric radiation pattern with two peaks, at $\phi = 0$ and $\phi = 180^o$ (in the above figures, they have been illustrated by positive θ and negative θ, respectively). The out of phase excitation makes the radiation pattern to have only one peak which depends on the sign of the phase difference between these modes.

Figures 5.4 to 5.7 show the magnitudes and phases of the E_θ patterns at $\phi = 0$ plane, when $|C_1| = |C_2| = 1, |C_0| = 0.5$ for different value of α_0 at a given $\alpha_1 - \alpha_2$, while the antennas are located at the coordinate origin. It is important to note that for $\alpha_o = 0$, a quadrature phase difference between the TM_{11} and TM_{21} modes, $|\alpha_1 - \alpha_2| = 90^o$, makes the far field phase pattern flat over the main beam, which in turn pushes the phase centre location to the physical center of the antenna. The reason is that, a 90^o phase shift, cancels the effect of j coefficient for the TM_{11} mode, as shown in equation 5.1. More details on phase centre location and the main beam tilt angle will be discussed in the next section.

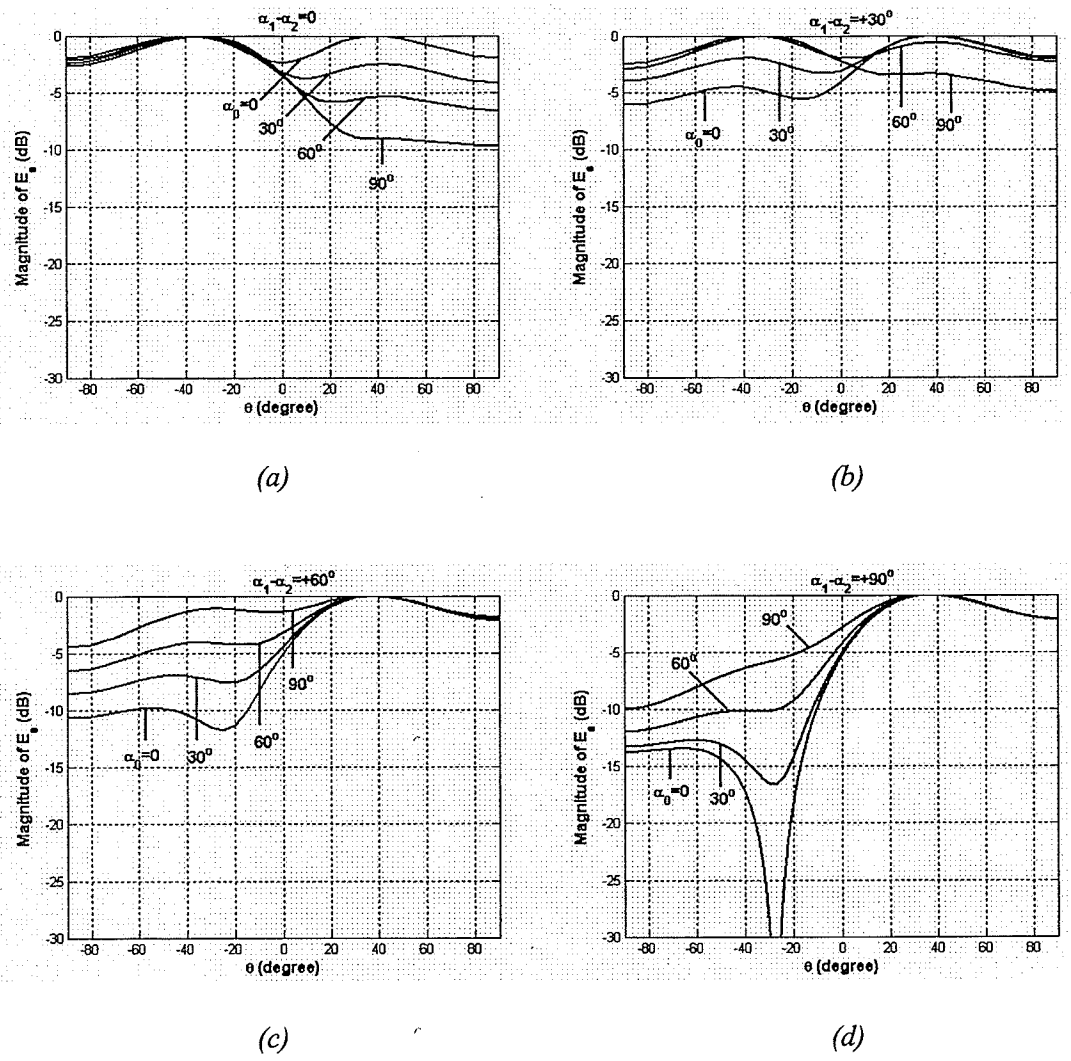

(a) *(b)*

(c) *(d)*

Fig. 5.4 Magnitude patterns of E_θ at $\phi = 0$ plane for different positive values of α_0 and $|C_1| = |C_2| = 1, |C_0| = 0.5$, of the antenna shown in Fig. 5.1, when it is located at the origin and all patches are fed along x-axis

(a) $\alpha_1 - \alpha_2 = 0$ *(b)* $\alpha_1 - \alpha_2 = +30^o$ *(c)* $\alpha_1 - \alpha_2 = +60^o$ *(d)* $\alpha_1 - \alpha_2 = +90^o$

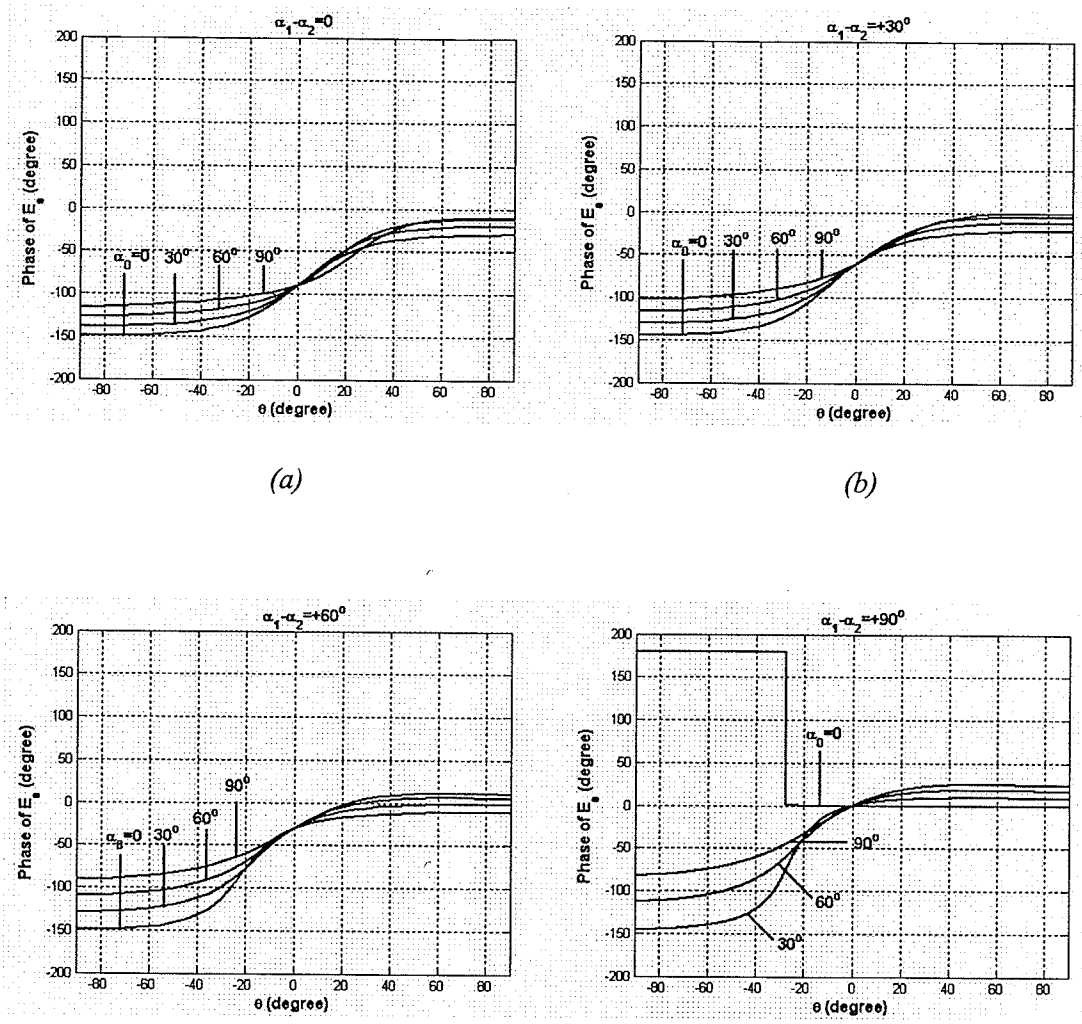

Fig. 5.5 Phase patterns of E_θ at $\phi = 0$ plane for different positive values of α_0 and $|C_1| = |C_2| = 1, |C_0| = 0.5$, of the antenna shown in Fig. 5.1, when it is located at the origin and all patches are fed along x-axis

(a) $\alpha_1 - \alpha_2 = 0$ *(b)* $\alpha_1 - \alpha_2 = +30^o$ *(c)* $\alpha_1 - \alpha_2 = +60^o$ *(d)* $\alpha_1 - \alpha_2 = +90^o$

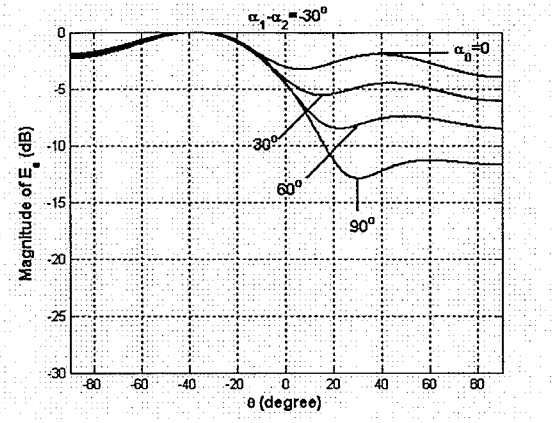

(a)

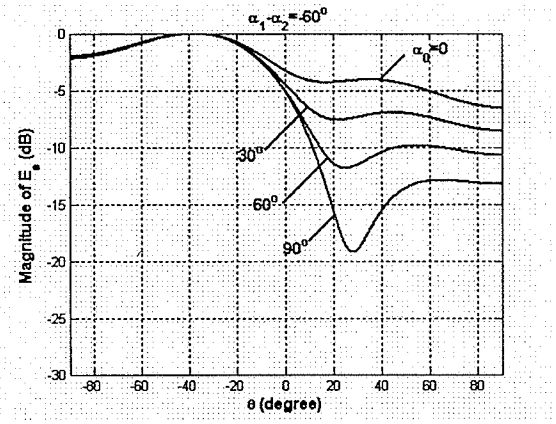

(b)

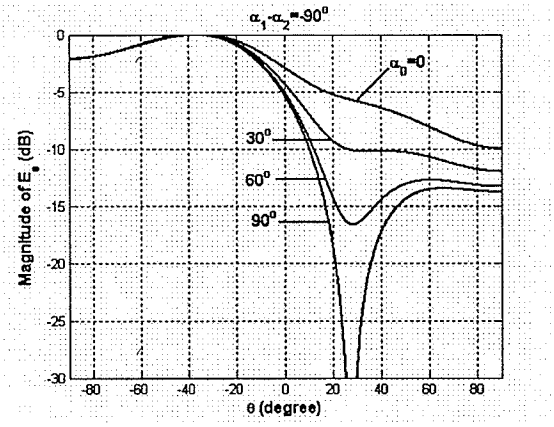

(c)

Fig. 5.6 Magnitude patterns of E_θ at $\phi = 0$ plane for different positive values of α_0 and $|C_1| = |C_2| = 1, |C_0| = 0.5$, of the antenna shown in Fig. 5.1, when it is located at the origin and all patches are fed along x-axis

(a) $\alpha_1 - \alpha_2 = -30^o$ (b) $\alpha_1 - \alpha_2 = -60^o$ (c) $\alpha_1 - \alpha_2 = -90^o$

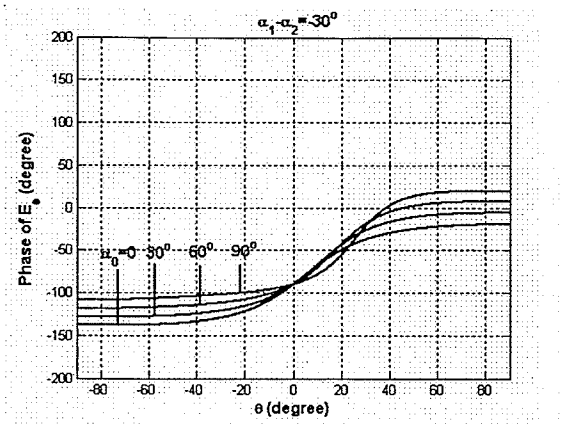

(a)

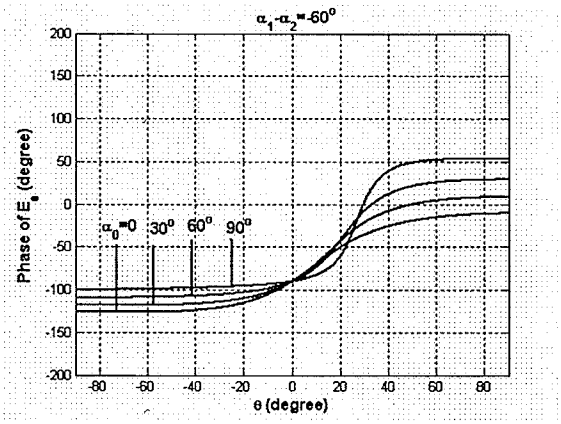

(b)

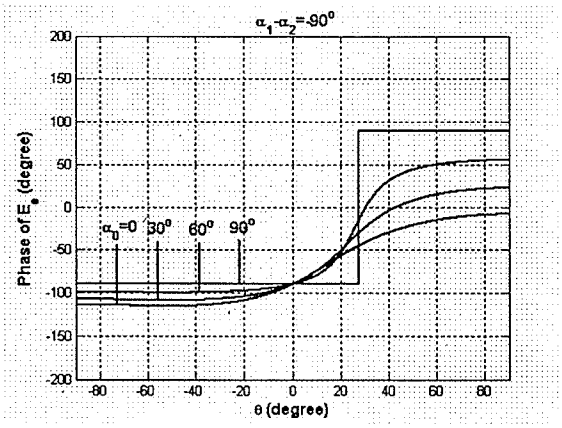

(c)

Fig. 5.7 Phase patterns of E_θ at $\phi = 0$ plane for different positive values of α_0 and $|C_1| = |C_2| = 1, |C_0| = 0.5$, of the antenna shown in Fig. 5.1, when it is located at the origin and all patches are fed along x-axis

(a) $\alpha_1 - \alpha_2 = -30^o$ (b) $\alpha_1 - \alpha_2 = -60^o$ (c) $\alpha_1 - \alpha_2 = -90^o$

Figures 5.8 and 5.9 illustrate particular cases, when the phase patterns may have negative slopes, when the entire antenna is located at the coordinate origin.

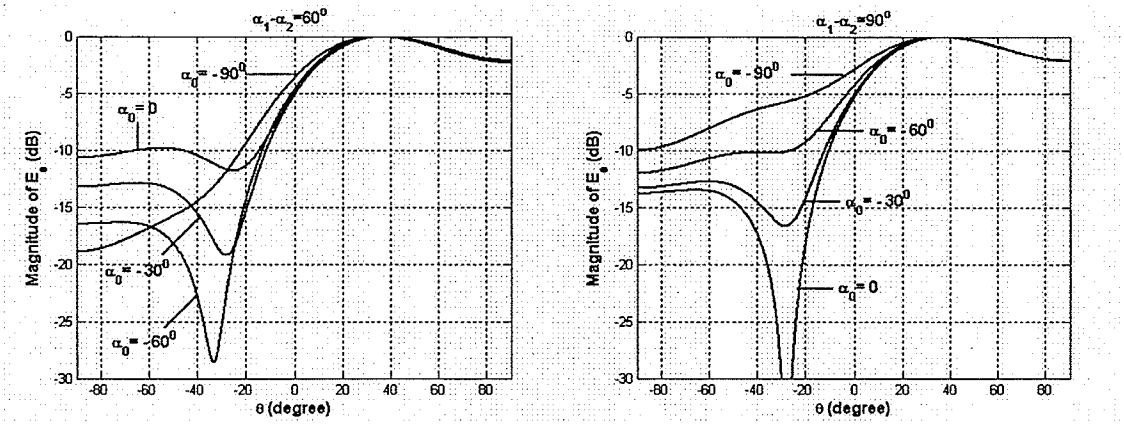

(a) *(b)*

Fig. 5.8 Magnitude patterns of E_θ at $\phi = 0$ plane for different negative values of α_0 and $|C_1| = |C_2| = 1, |C_0| = 0.5$, of the antenna shown in Fig. 5.1, when it is located at the origin and all patches are fed along x-axis

(a) $\alpha_1 - \alpha_2 = 60^o$ (b) $\alpha_1 - \alpha_2 = 90^o$

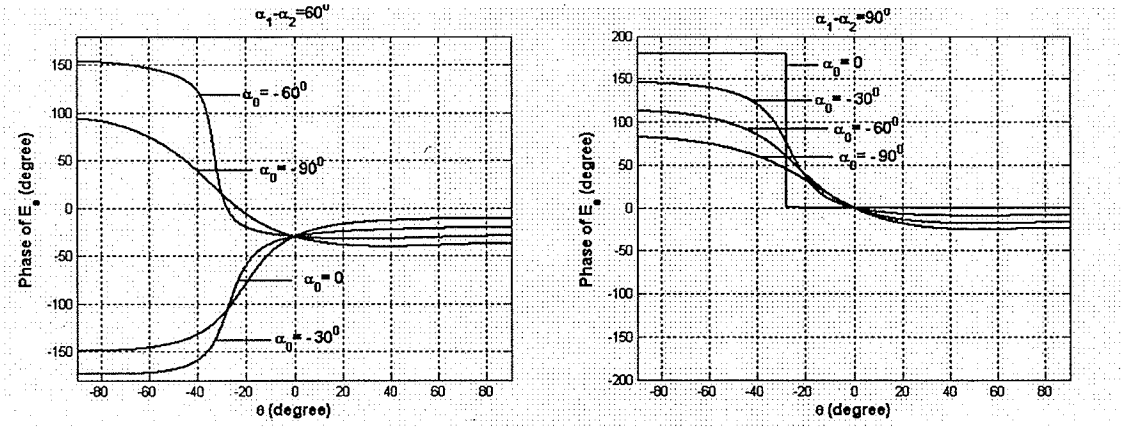

(a) *(b)*

Fig. 5.9 Phase patterns of E_θ at $\phi = 0$ plane for different negative values of α_0 and $|C_1| = |C_2| = 1, |C_0| = 0.5$, of the antenna shown in Fig. 5.1, when it is located at the origin and all patches are fed along x-axis

(a) $\alpha_1 - \alpha_2 = 60^o$ (b) $\alpha_1 - \alpha_2 = 90^o$

5.2.2 Phase centre location and main beam tilt angle

As shown in the preceding section, by adding two higher order modes to the dominant mode, which has a constant phase pattern, the far-field phase patterns change over the angles of the main beam axis and are not constant, except when $|\alpha_1 - \alpha_2| = 90^o$ and $\alpha_o = 0$. This means, the signals are not emanating from the center of the antenna, or in other words, the antenna phase centre has moved. In order to find the new phase centre location, one may displace the antenna from the coordinate origin, so that a new phase term can be introduced to the antenna function, which will be dependent on the displacement. Enforcing the constant phase values over the main beam will allow determination of the displacement coordinates. For all non-zero amplitude excitations, positive $\alpha_1 - \alpha_2$ and positive α_0, phase patterns have positive slope versus angle of axis implying that, one must add a negative slope to the initial phase pattern to obtain a constant phase distribution. But there are some cases with negative value of α_0 at a given positive value of $\alpha_1 - \alpha_2$, in which the phase patterns may have negative slopes, as in Fig. 5.9. In order to recognize these cases, the phase centres are plotted versus x_0 instead of r_0 in such a way that positive x_0 means the phase centre is located at $\phi_0 = 0$ and negative x_0 means it is located at $\phi_0 = 180^o$.

For the antennas discussed in chapters 3 and 4, the locus of the phase centre at a given ϕ in the cylindrical coordinates is a line perpendicular to the ϕ direction passing through the point $(r_0, \phi_0 = \phi + \pi)$, as discussed in sections 3.2.1.2 and 4.2.2. While for the TM_{11}, TM_{21} and TM_{02} modes , since the phase pattern slopes may change depending on

the sign of α_0, the locus will be lines perpendicular to the ϕ direction passing through either $(r_0, \phi_0 = \phi + \pi)$ or $(r_0, \phi_0 = \phi)$.

Figure 5.10 shows the phase centre loci of the E_θ patterns of the antenna shown in Fig. 5.1 for the two different cases. Figure 5.10a depicts the phase centre locus, which is shown by the solid line passing through the point $(r_0 = 0.16\lambda, \phi_0 = \pi)$, when all excitations are in-phase, i.e. $\alpha_1 = \alpha_2 = \alpha_0 = 0$ and $\frac{C_2}{C_1} = 0.25\angle 0, \frac{C_0}{C_1} = 0.3\angle 0$. Figure 5.10b illustrates this locus, which is a solid line passing through the point $(r_0 = 0.04\lambda, \phi_0 = 0)$, when $\frac{C_2}{C_1} = 1\angle -90^o, \frac{C_0}{C_1} = 0.5\angle -180^o$.

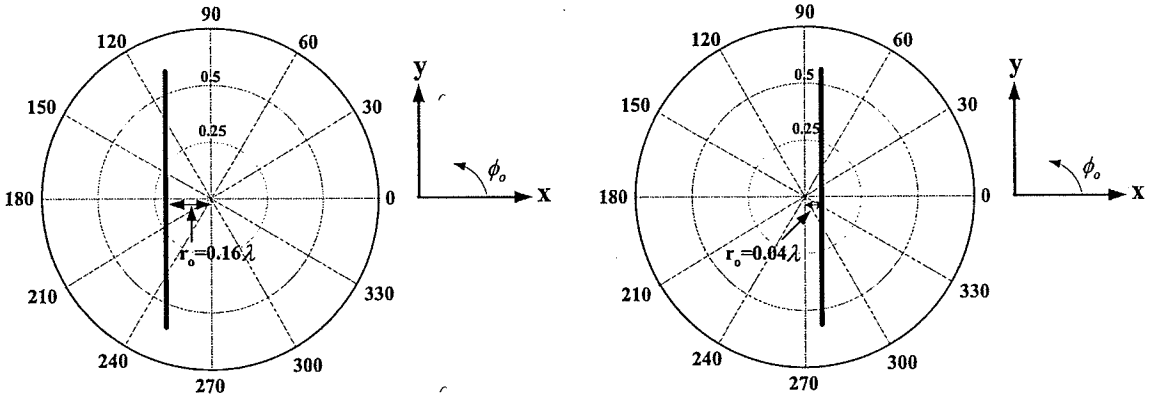

(a) *(b)*

Fig. 5.10 The locus of phase centre of the E_θ patterns of the antenna shown in Fig. 5.1, when all patches are fed along x-axis

(a) $C_1 = 1\angle 0, C_2 = 0.25\angle 0, C_0 = 0.3\angle 0$

(b) $C_1 = 1\angle 90^o, C_2 = 1\angle 0, C_0 = 0.5\angle -90^o$

The effects of in-phase excitation amplitude ratio on the phase centre location and main beam tilt angle are shown in Fig. 5.11 and 5.12, respectively, for two dielectric constants of 1.15 and 2.32 and different $\frac{C_2}{C_1}$, when C_0 changes from 0 to 2. As can be seen, for all in-phase amplitude excitations, the phase centre moves away from the center and then it returns to the antenna center. The main beam tilt also moves toward the endfire direction.

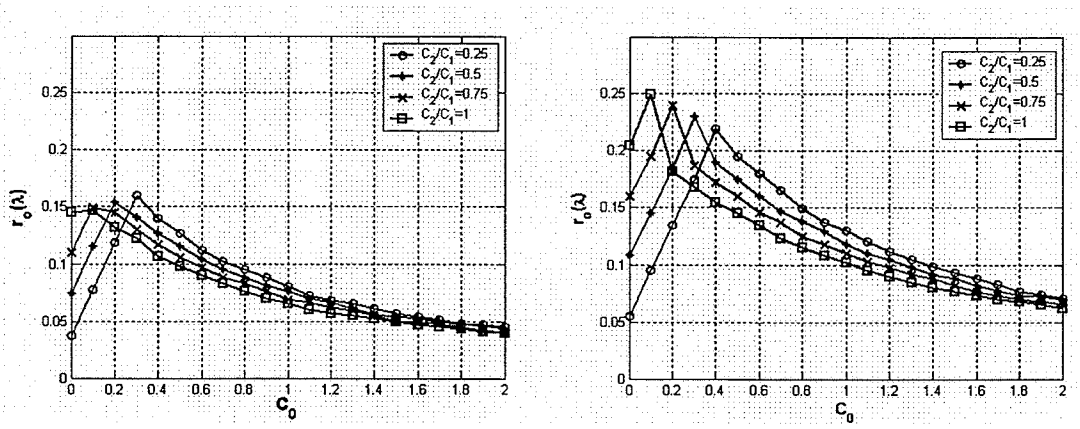

(a) *(b)*

Fig. 5.11 Effect of C_0 on phase centre location of E_θ at $\phi = 0^o$ plane for different $\left|\frac{C_2}{C_1}\right|$ with in-phase excitations over main beam, when all patches are fed along x-axis while $\phi_0 = 180^o$, for the antenna:
(a) shown in Fig. 5.1, ε_r=2.32
(b) has the same structure as Fig. 5.1 with ε_r=1.15,(a_{TM11}=6.8mm, a_{TM21}=12.42, a_{TM02}=15.27mm)

As can be seen from Fig. 5.11b, the TM_{02} mode makes the peak phase centre location move further away from the physical center of the antenna comparing to the Fig. 3.9, section 3.2.1.2, in which the antenna produced TM_{11} and TM_{21} modes with ε_r=1.15. That is, the maximum phase centre location of the antenna operating at TM_{11} and TM_{21}

modes is 0.21λ, while adding the TM_{02} mode to the above mentioned modes results in a maximum phase centre at 0.25λ.

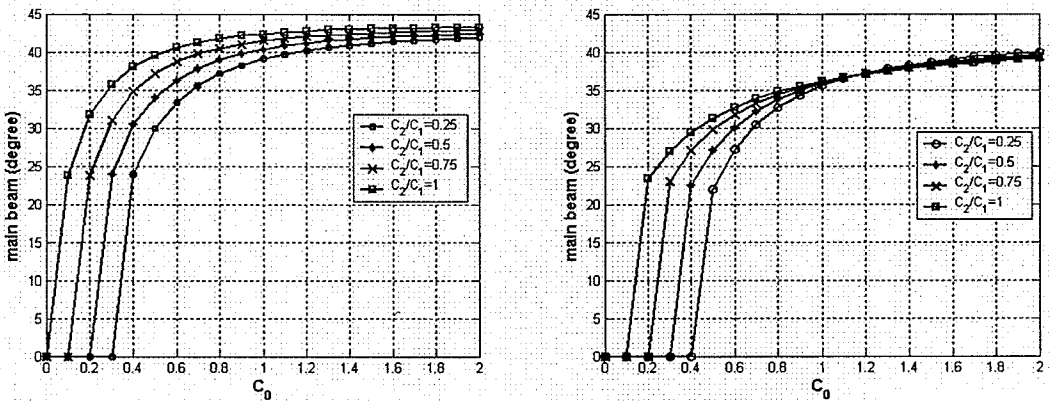

Fig. 5.12 Effect of C_0 on main beam tilt angle for E_θ at $\phi = 0^o$ plane for different $\left|\frac{C_2}{C_1}\right|$ with in-phase excitations, when all patches are fed along x-axis while $\phi_0 = 180^o$, for the antenna:
(a) shown in Fig. 5.1, ε_r=2.32
(b) has the same structure as Fig. 5.1 with ε_r=1.15,(a_{TM11}=6.8mm, a_{TM21}=12.42, a_{TM02}=15.27mm)

The effects of the excitation phase difference on the phase centre location and main beam tilt angle were also studied, which are shown in Fig 5.13 and 5.14, respectively, for certain amplitude excitation ratios. They show that, when $\frac{C_2}{C_1} = 1$ and $\alpha_1 - \alpha_2 = 90^o$, the main beam for all values of α_0 is almost constant, while the phase centre changes from positive x_0 to negative x_0 with passing at the origin. For the case $\frac{C_2}{C_1} = 0.25$ and $\alpha_1 - \alpha_2 = 0^o$, the negative value of α_0 makes the main beam move to the positive θ and vice versa, while there are symmetric patterns with two peaks for in-phase

excitations. The other cases with higher $\frac{C_2}{C_1}$ and positive $\alpha_1 - \alpha_2$, the main beam tilt moves from positive θ to the other side like cases b and c in Fig. 5.14.

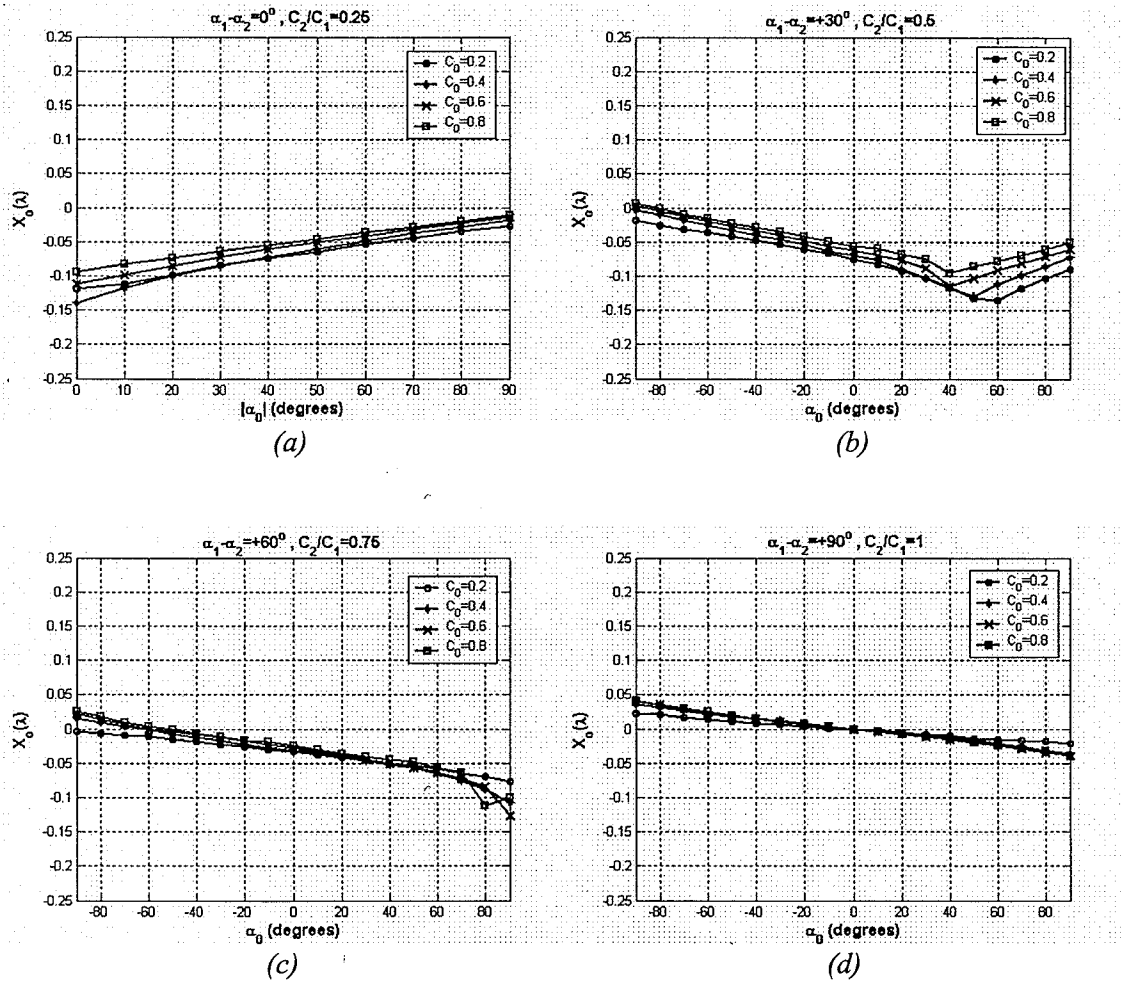

Fig. 5.13 Phase centre location of E_θ at $\phi = 0$ plane versus α_0 for different C_0, over main beam, for the antenna shown in Fig. 5.1, when all patches are fed along x-axis

$$(a)\ \frac{C_2}{C_1} = 0.25, \alpha_1 - \alpha_2 = 0 \quad (b)\ \frac{C_2}{C_1} = 0.5, \alpha_1 - \alpha_2 = +30^\circ$$

$$(c)\ \frac{C_2}{C_1} = 0.75, \alpha_1 - \alpha_2 = +60^\circ \quad (d)\ \frac{C_2}{C_1} = 1, \alpha_1 - \alpha_2 = +90^\circ$$

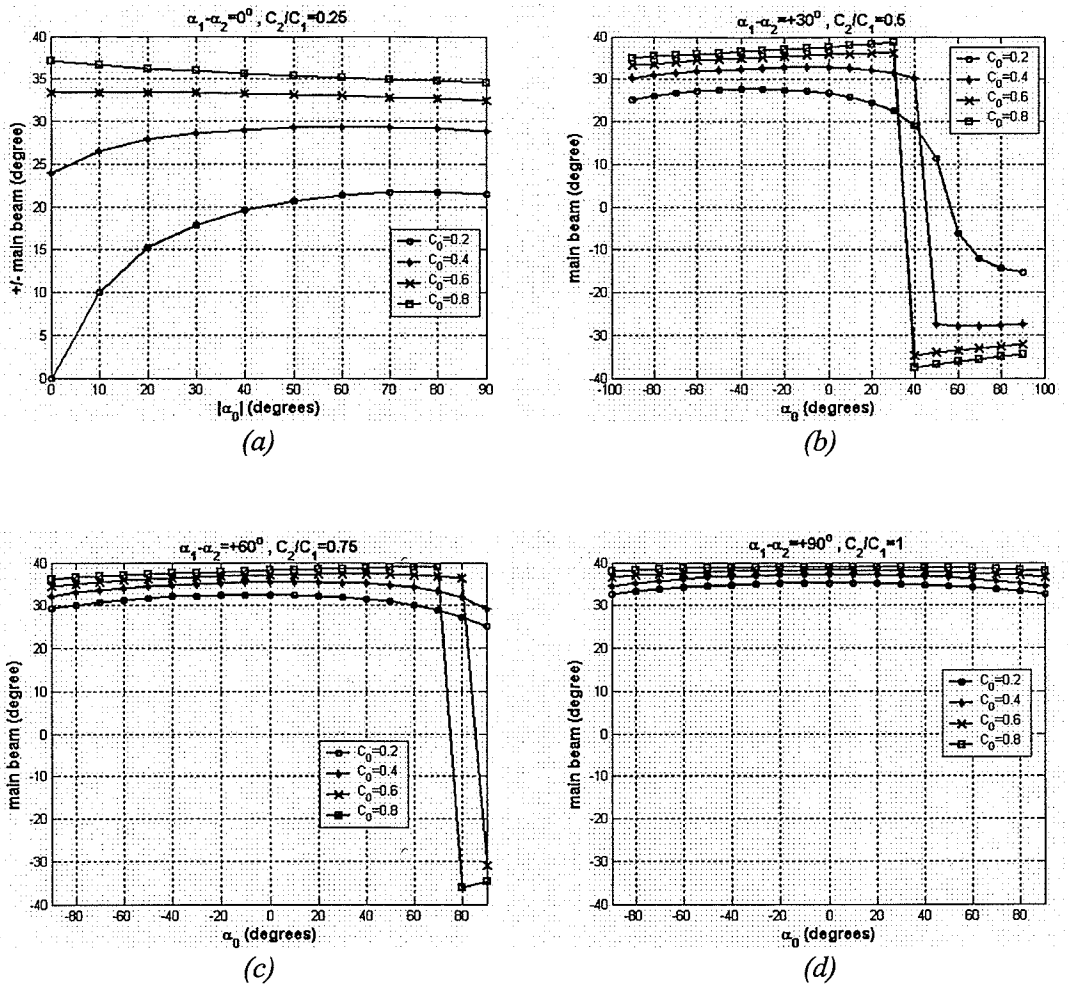

Fig. 5.14 Main beam tilt angle of E_θ at $\phi = 0$ plane versus α_0 for different C_0, over main beam, for the antenna shown in Fig. 5.1, when all patches are fed along x-axis

(a) $\frac{C_2}{C_1} = 0.25, \alpha_1 - \alpha_2 = 0$ *(b)* $\frac{C_2}{C_1} = 0.5, \alpha_1 - \alpha_2 = +30^o$

(c) $\frac{C_2}{C_1} = 0.75, \alpha_1 - \alpha_2 = +60^o$ *(d)* $\frac{C_2}{C_1} = 1, \alpha_1 - \alpha_2 = +90^o$

5.2.3 Polarization properties

As expressed in equations 5.1 and 5.2, the total field for the antenna under study is an x-polarized one. So, we can use Ludwig's third definition for an x-aligned field as expressed in equation 3.8.

Similarly, there will be a global phase centre for the antenna operating at TM_{11}, TM_{21}, and TM_{02} modes, when the copolar radiation pattern is considered, as discussed in chapter 3, section 3.2.13. For this antenna, such a phase centre is located at $\phi_0 = 180^\circ$ for excitation amplitude ratio less than 0.35, and $\alpha_1=\alpha_2=\alpha_0$. The effect of amplitude excitation ratio on the phase centre location of the copolar radiation pattern is shown in Fig. 5.15. Again, there will be a multiple phase centres beyond the excitation amplitude ratios shown in Fig. 5.15, since the peak radiation directions of E- and H-plane patterns will not be the same at all ϕ-planes.

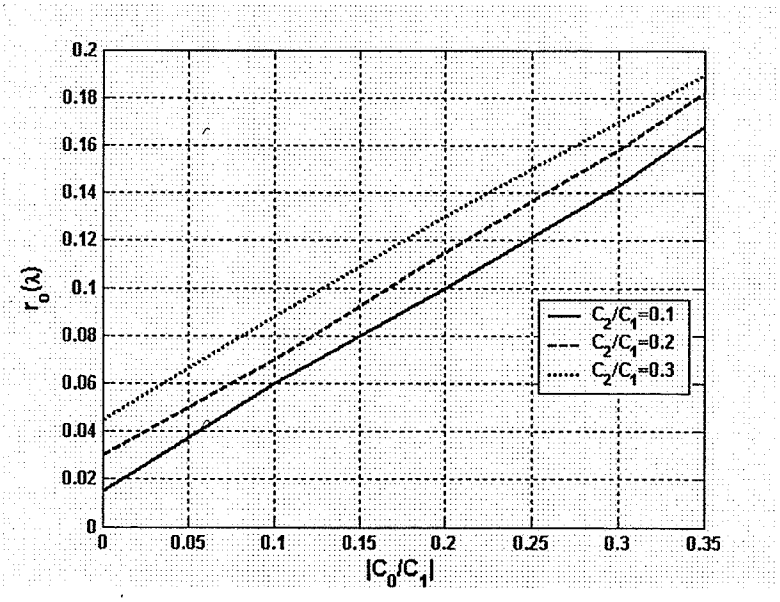

Fig. 5.15 Effect of $|C_0/C_1|$ on the phase centre location of copolar radiation pattern of the antenna shown in Fig. 5.1, over main beam for different excitation amplitudes C_2/C_1, when $\alpha_1=\alpha_2=\alpha_0$ and $\phi_0=180^\circ$.

The copolar and crosspolar patterns at different ϕ-planes are as below:

- At $\phi = 0$ plane:

$$\left\{\begin{array}{l} E_{co}\,|_{\phi=0} = E_{\theta}\,|_{\phi=0} \\ E_{xpol}\,|_{\phi=0} = E_{\phi}\,|_{\phi=0} = 0 \end{array}\right\} \tag{5.3}$$

- At $\phi = 90^{o}$ plane:

$$\left\{\begin{array}{l} E_{co}\,|_{\phi=90^{o}} = -E_{\phi}\,|_{\phi=90^{o}} \\ E_{xpol}\,|_{\phi=90^{o}} = E_{\theta}\,|_{\phi=90^{o}} \end{array}\right\} \tag{5.4}$$

- At $\phi = 45^{o}$ plane:

$$\left\{\begin{array}{l} E_{co}\,|_{\phi=45^{o}} = \left(\cos\phi\, E_{\theta} - \sin\phi\, E_{\phi}\right)|_{\phi=45^{o}} \\ E_{xpol}\,|_{\phi=45^{o}} = \left(\sin\phi\, E_{\theta} + \cos\phi\, E_{\phi}\right)|_{\phi=45^{o}} \end{array}\right\} \tag{5.5}$$

As can be seen, at $\phi = 0$ plane, the crosspolarization is zero since E_{ϕ} for all three modes vanishes on this plane.

The crosspolar patterns for the antenna operating at TM_{11} and TM_{21} modes, and TM_{11} and TM_{02} modes were investigated in chapters 3 and 4. It was shown that, by adding either TM_{21} or TM_{02} mode to the dominant mode, the normalized crosspolar to copolar level increases. If an antenna can generate all the first three modes, it is possible to control the crosspolarization by the TM_{02} mode. By exciting the proper amount of this mode, one can decrease the crosspolarization since the surface current pattern will become parallel lines, based on the discussion in section 2.4. Figure 5.16 shows the copolar and crosspolar patterns at $\phi = 90^{o}$ plane for different mode excitation ratios with and without the TM_{02} mode. The amount of this mode was selected to give the minimum crosspolarization, while it will change the phase centre location.

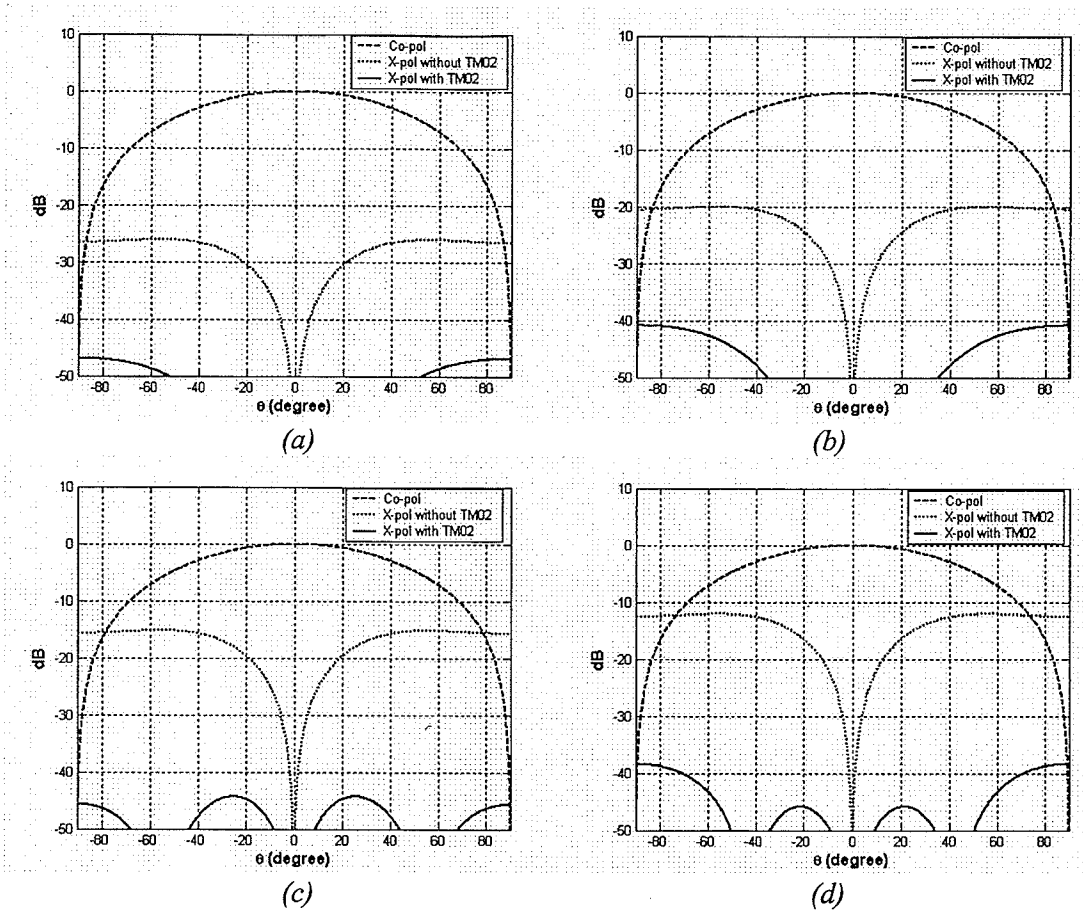

Fig. 5.16 Normalized copolar and crosspolar components at $\phi = 90^{\circ}$ plane, of the antenna shown in Fig. 5.1, when all patches are fed along x-axis

(a) $\frac{C_2}{C_1} = 0.1\angle 0, C_0 = 0.04\angle 0$, *(b)* $\frac{C_2}{C_1} = 0.2\angle 0, C_0 = 0.08\angle 0$

(c) $\frac{C_2}{C_1} = 0.35\angle 0, C_0 = 0.15\angle 0$, *(d)* $\frac{C_2}{C_1} = 0.5\angle 0, C_0 = 0.21\angle 0$

As can be seen form Fig. 5.16, one can decrease the crosspolarization level to less than -40dB by exciting the TM_{02} mode in the antenna working at TM_{11} and TM_{21} modes.

Figure 5.17 shows the copolar and crosspolar patterns at $\phi = 45^{\circ}$ plane for different mode excitation ratios with and without the TM_{02} mode. The amount of this mode was selected to give the minimum crosspolarization. Again, the antenna phase centre will be changed.

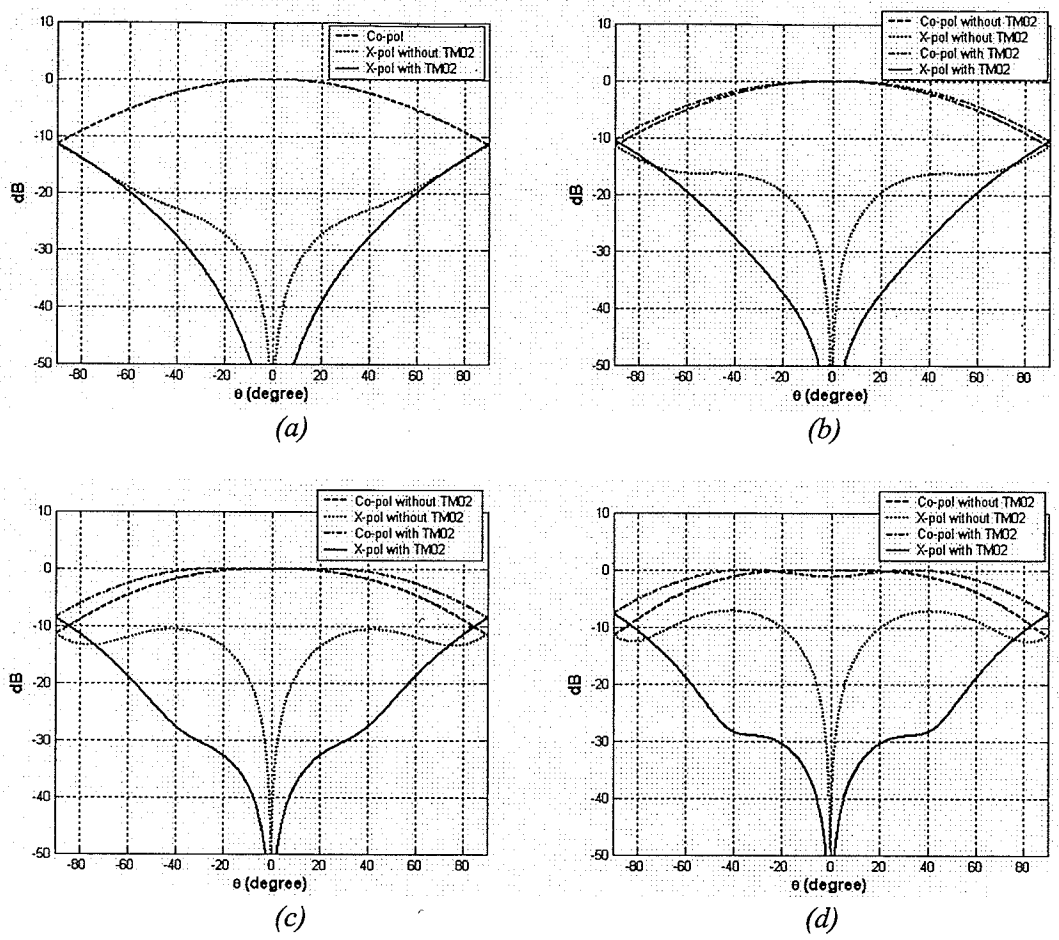

Fig. 5.17 Normalized copolar and crosspolar components at $\phi = 45^o$ plane, of the antenna shown in Fig. 5.1, when all patches are fed along x-axis

(a) $\frac{C_2}{C_1} = 0.2\angle 0, C_0 = 0.07\angle 0$ *(b)* $\frac{C_2}{C_1} = 0.5\angle 0, C_0 = 0.18\angle 0$

(c) $\frac{C_2}{C_1} = 1\angle 0, C_0 = 0.355\angle 0$ *(d)* $\frac{C_2}{C_1} = 1.5\angle 0, C_0 = 0.53\angle 0$

Figure 5.18 shows the required excitation amplitude of the TM_{02} mode, C_0, for a given $\frac{C_2}{C_1}$ at $\phi = 45^o$ plane over the range of $-45^o \le \theta \le +45^o$. It shows by increasing the

mode excitation ratio for the dominant mode and TM_{21} mode, $\frac{C_2}{C_1}$, the required amount of C_0, increases to obtain the minimum crosspolarization level.

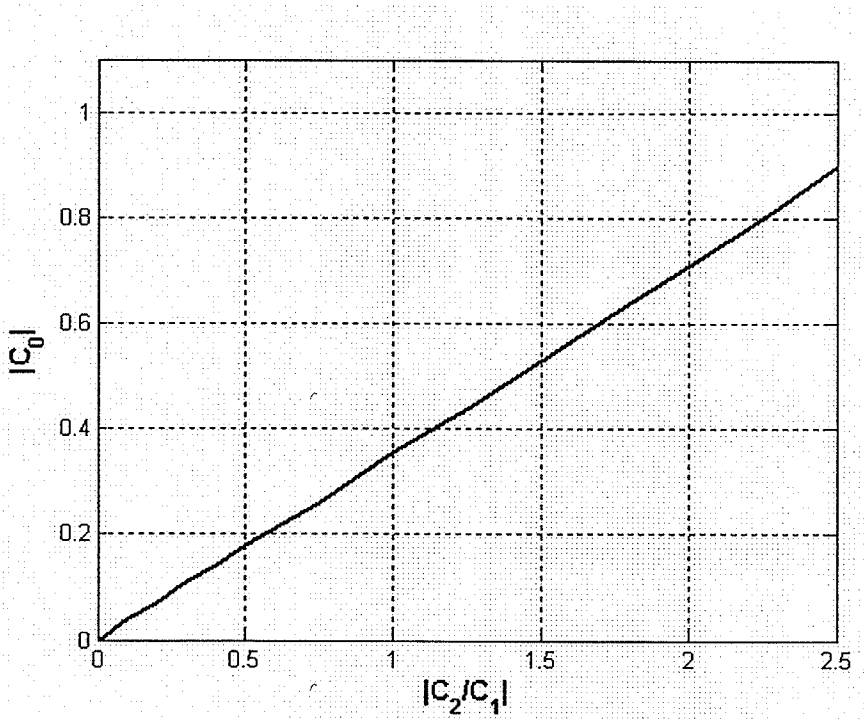

Fig. 5.18 Required C_0 versus $\frac{C_2}{C_1}$ to have minimum crosspolarization at $\phi = 45^o$ plane over the range of $-45^o \leq \theta \leq +45^o$, for the antenna shown in Fig. 5.1, when all patches are fed along x-axis, $\alpha_1=\alpha_2=\alpha_0$.

As mentioned earlier, adding the TM_{02} mode to the dominant and TM_{21} modes, provides an option to minimize the crosspolarization levels over the boresight angle. But as shown in Figs. 5.16 to 5.18, this can change the antenna phase centre location. In order to keep the phase centre location unchanged, one needs to change the excitation amplitude ratios

of all three modes. Table 5.1 gives the required TM_{02} mode in order to minimize the crosspolarization levels at ϕ=45° plane and keep the phase centre location constant.

C_2/C_1	C_0/C_1	Phase Centre r_o (ϕ_o=180°)	Crosspol level (ϕ=45°)
$1\angle 0$	0	0.15λ	≤-10.5dB
$0.55\angle 0$	$0.19\angle 0$	0.15λ	≤-31.5dB
$0.9\angle 0$	0	0.133λ	≤-11.5dB
$0.5\angle 0$	$0.17\angle 0$	0.133λ	≤-31.5dB
$0.8\angle 0$	0	0.118λ	≤-12.5dB
$0.4\angle 0$	$0.17\angle 0$	0.118λ	≤-32dB
$0.7\angle 0$	0	0.103λ	≤-13.5dB
$0.35\angle 0$	$0.15\angle 0$	0.103λ	≤-32dB
$0.6\angle 0$	0	0.088λ	≤-15dB
$0.3\angle 0$	$0.12\angle 0$	0.088λ	≤-33dB
$0.5\angle 0$	0	0.07λ	≤-16.5dB
$0.25\angle 0$	$0.09\angle 0$	0.07λ	≤-33dB
$0.4\angle 0$	0	0.0555λ	≤-19.25dB
$0.2\angle 0$	$0.08\angle 0$	0.0555λ	≤-33dB
$0.3\angle 0$	0	0.042λ	≤-21.5dB
$0.15\angle 0$	$0.06\angle 0$	0.042λ	≤-33dB
$0.2\angle 0$	0	0.029λ	≤-24.5dB
$0.12\angle 0$	$0.043\angle 0$	0.029λ	≤-33dB
$0.1\angle 0$	0	0.015λ	≤-29dB
$0.045\angle 0$	$0.015\angle 0$	0.015λ	≤-33dB

Table 5.1 Effect of TM_{02} mode on the crosspolarization at ϕ=45° plane, for the antenna operating at TM_{11} and TM_{21} modes, ε_r=2.32, while the phase centre location is unchanged, for different in-phase excitation amplitude ratios, when all patches are fed along x-axis, ε_r=2.32, ($-30^o \le \theta \le +30^o$) and θ_{peak} =0.

5.3 Design Example

In order to verify the above analytical results, a multi-layer antenna was designed and simulated by Ansoft Designer package version 2 which is based on a Method of Moment. The geometry of the antenna is shown in Fig. 5.19. The layer assignment and feeding structure will be discussed in chapter 6. One type substrate was used for all layers with $\varepsilon_r = 2.32$. The operating frequency is 10GHz. The finite ground plane was considered since it can be fabricated practically.

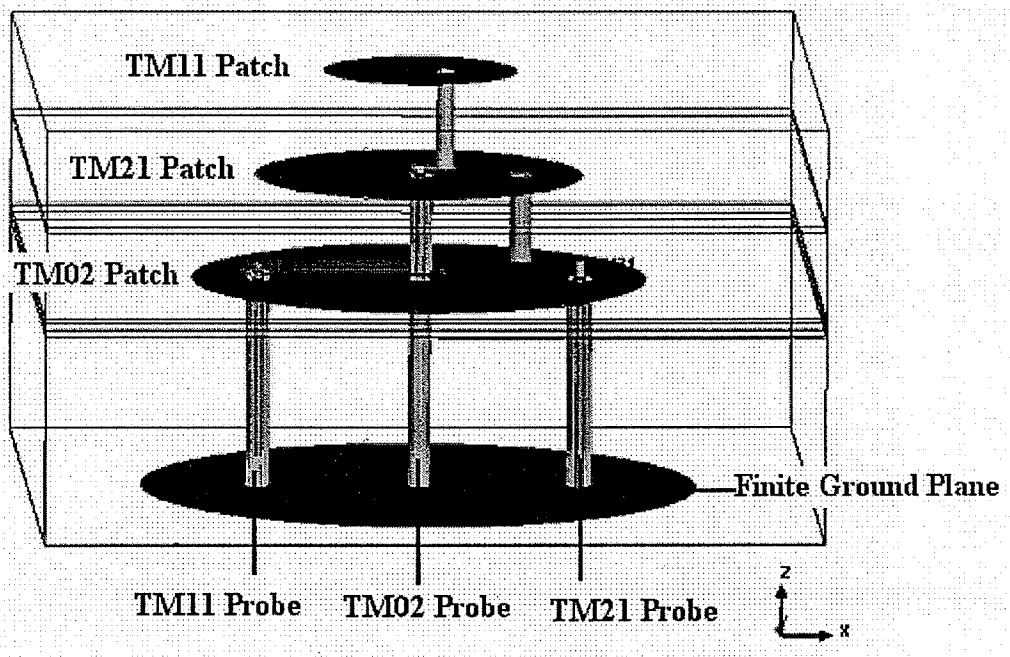

Fig. 5.19 The geometry of stacked patches operating at TM_{11}, TM_{21} and TM_{02} modes over a finite ground plane

$$a_{TM11} = 5.588mm,\ a_{TM21} = 9.4mm,\ a_{TM02} = 13.07mm,\ a_{ground} = 16mm$$

$$\rho_f^{TM11} = 1.4mm,\ \phi_m^{TM11} = 0$$

$$\rho_f^{TM21} = 5.83mm,\ \phi_m^{TM21} = 0$$

$$\rho_f^{TM02} = 0mm,\ \phi_m^{TM02} = 0$$

$$h_1 = h_2 = 1.5mm,\ h_3 = 3mm,\ \varepsilon_r = 2.32$$

Three individual probes have been used to excite the antenna, each for one of the TM_{11}, TM_{21}, and TM_{02} modes. The feed locations were optimized, in order to excite each mode properly, based on the discussion in chapter 2, section 2.2.3, and to have a good impedance match condition at 10GHz. The scattering parameters of the antenna are shown in Fig. 5.20. As can be seen, the return losses for all ports are below -10dB at 10GHz, which provides good impedance matches at the frequency of operation.

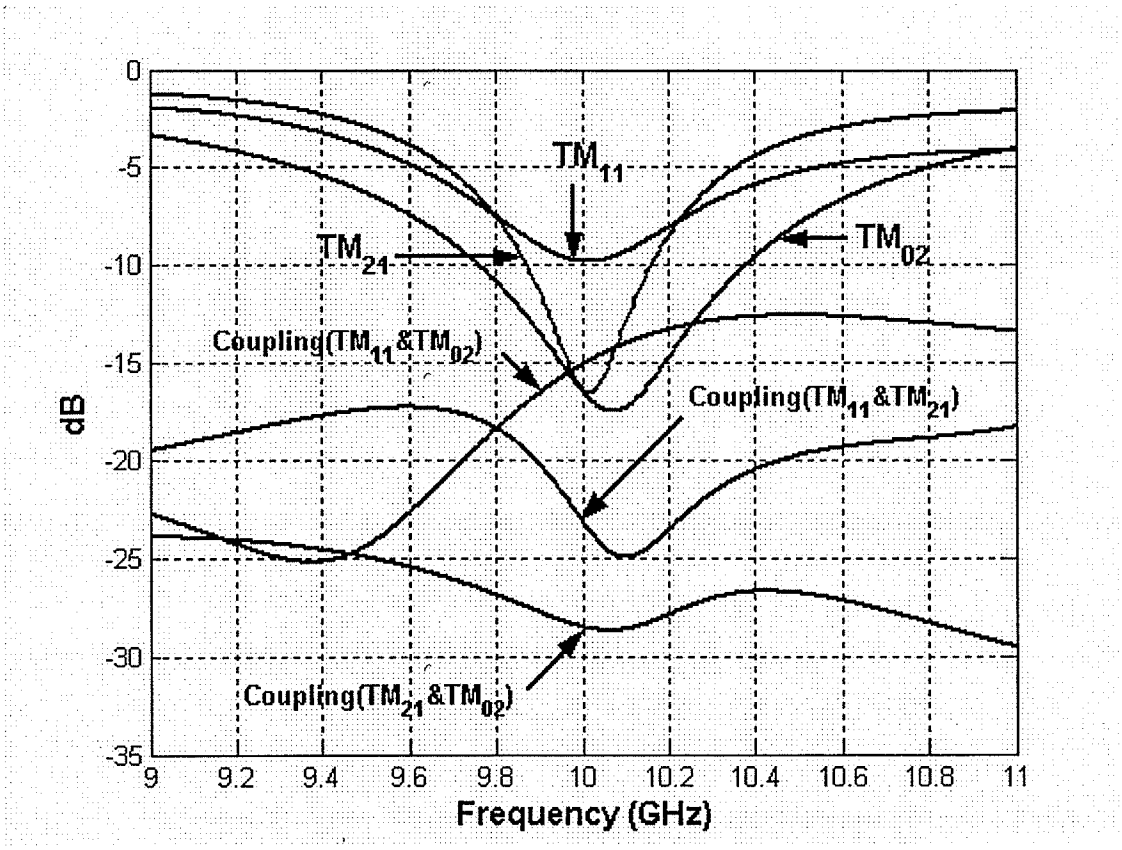

Fig. 5.20 Scattering parameters of stacked patch antenna shown in Fig. 5.19 operating at TM_{11}, TM_{21} and TM_{02} modes over a finite ground plane

As is known, a probe feed introduces a phase shift in real situation. So, in the above designed example, these feeds will cause phase shifts at each port. In order to compare the current simulation results with previous analytical ones, we must determine

the relationship between the mode constants, C_n, and V_n, as well as the phase shift values for each probe.

Based on equation 2.14, $V_n = \frac{2C_n}{a_n k_0}$,

If $C_1 = C_2$: $$\frac{V_1}{V_2} = \frac{a_2}{a_1} = \frac{\chi_{21}}{\chi_{11}} = \frac{3.054}{1.841} = 1.6589 \quad (5.6)$$

If $C_1 = C_0$: $$\frac{V_0}{V_1} = \frac{a_1}{a_0} = \frac{\chi_{11}}{\chi_{02}} = 0.48 \quad (5.7)$$

As we excited all patches in current, the amplitude of currents for each mode will be $|I_{TM11}| = 82.94mA, |I_{TM21}| = 50mA, |I_{TM02}| = 39.85mA$, based on the discussion in section 3.2.2. Now, we have to choose proper phase for each mode to cancel the probe phase shift. These values are $\angle I_{TM11} = -80^o$, $\angle I_{TM21} = 90^o$, $\angle I_{TM02} = 215^o$. They were chosen to make the analytical and numerical phase distributions identical as shown in Fig. 5.22 and Fig. 5.25. It means, the case with in-phase and equal amplitude (C_n) in the analytical approach is counterpart with following current excitations in numerical simulations, as shown in table 5.2:

$$I_{TM11} = 83mA\angle -80^o,\ I_{TM21} = 50mA\angle 90^o,\ I_{TM02} = 40mA\angle 215^o \quad (5.8)$$

Please note that, due to the poor impedance matching at the TM_{11} port and relatively high coupling between the TM_{11} port and TM_{02} port, the amplitude current excitation ratio may be slightly different from the calculated one.

Excitation Ratio	Amplitude	Phase (degrees)
Analytical $(\frac{C_2}{C_1})$	**1**	**0**
Numerical $(\frac{I_{TM21}}{I_{TM11}})$	**0.6024**	**+170°**
Analytical $(\frac{C_0}{C_1})$	**1**	**0**
Numerical $(\frac{I_{TM02}}{I_{TM11}})$	**0.48**	**+65°**

Table 5.2 Relation between excitation ratios C_2/C_1, C_0/C_1 in analytical method (Fig. 5.1) and current excitation ratios I_2/I_1 , I_0/I_1 in numerical method (Fig. 5.19) for the stacked patch antenna operating at TM_{11}, TM_{21}, and TM_{02} modes, when both patches are fed along x-axis.

As we are interested in having antennas with broadside radiation patterns, but phase centres away from the origin, we present two cases, with in-phase excitation ratios of $\frac{C_2}{C_1} = 0.25, \frac{C_0}{C_1} = 0.2$ and $\frac{C_2}{C_1} = 0.75, \frac{C_0}{C_1} = 0.1$. Figure 5.21 and 5.22 show the magnitude and phase of E_θ pattern of the antenna in $\phi = 0$ plane, when the antenna is located at the coordinate origin for the case of $\frac{C_2}{C_1} = 0.25, \frac{C_0}{C_1} = 0.2$. Figure 5.23 illustrates the phase pattern after displacing the entire antenna to $\left(r_o = 0.119\lambda, \phi_o = 180^o\right)$. Figures 5.24 to 5.26 show the same properties as above for the case of $\frac{C_2}{C_1} = 0.75, \frac{C_0}{C_1} = 0.1$. This time, the phase centre moves to $\left(r_o = 0.15\lambda, \phi_o = 180^o\right)$.

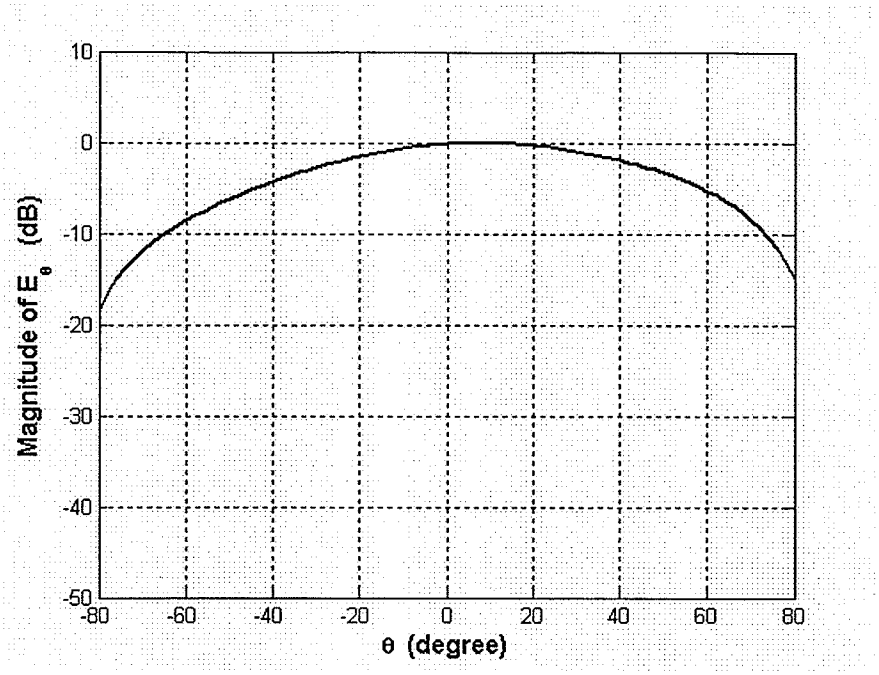

Fig.5.21 Magnitude pattern of E_θ at $\phi = 0$ plane for the antenna shown in Fig. 5.19, when all patches are fed along x-axis and located at the origin, C_2/C_1=0.25 ∠ 0, C_0/C_1=0.2 ∠ 0

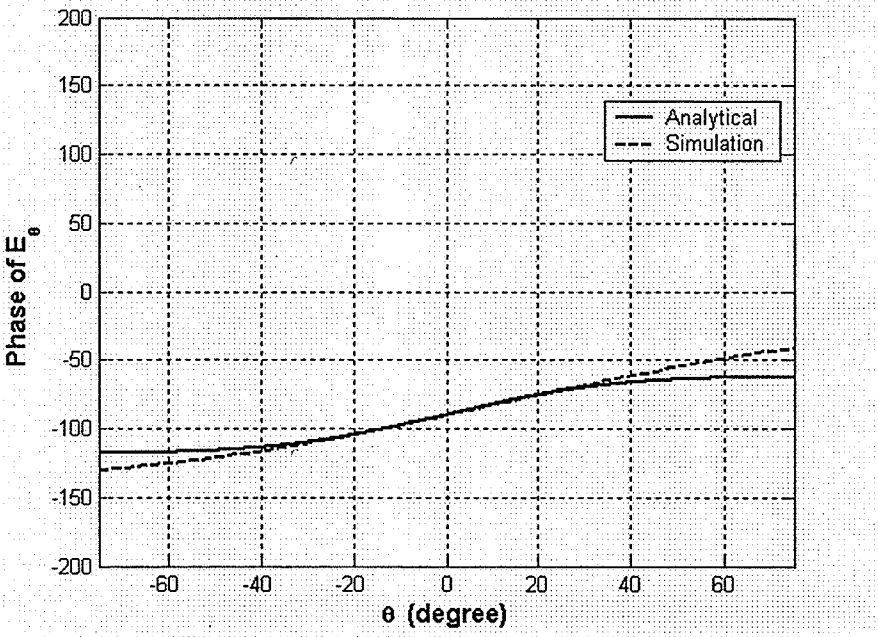

Fig. 5.22 Phase pattern of E_θ at $\phi = 0$ plane for the antenna shown in Fig. 5.19, when all patches are fed along x-axis and located at the origin, C_2/C_1=0.25 ∠ 0, C_0/C_1=0.2 ∠ 0

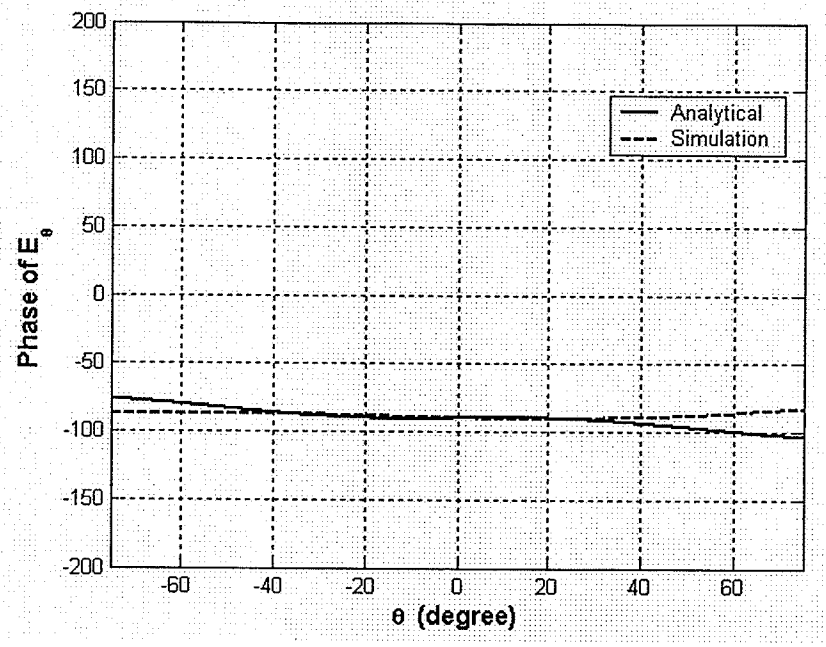

Fig. 5.23 Phase pattern of E_θ at $\phi = 0$ plane for the antenna shown in Fig. 5.19, when all patches are fed along x-axis $\left(r_0 = 0.119\lambda,\ \phi_0 = 180^o\right)$ and C_2/C_1=0.25∠0, C_0/C_1=0.2∠0

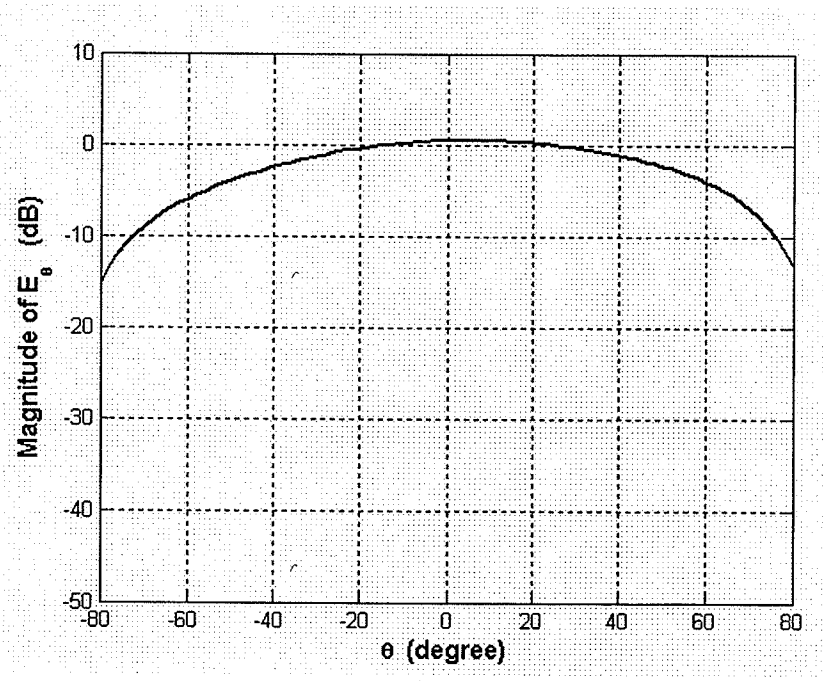

Fig. 5.24 Magnitude pattern of E_θ at $\phi = 0$ plane for the antenna shown in Fig. 5.19, when all patches are fed along x-axis and located at the origin, C_2/C_1=0.75∠0, C_0/C_1=0.1∠0

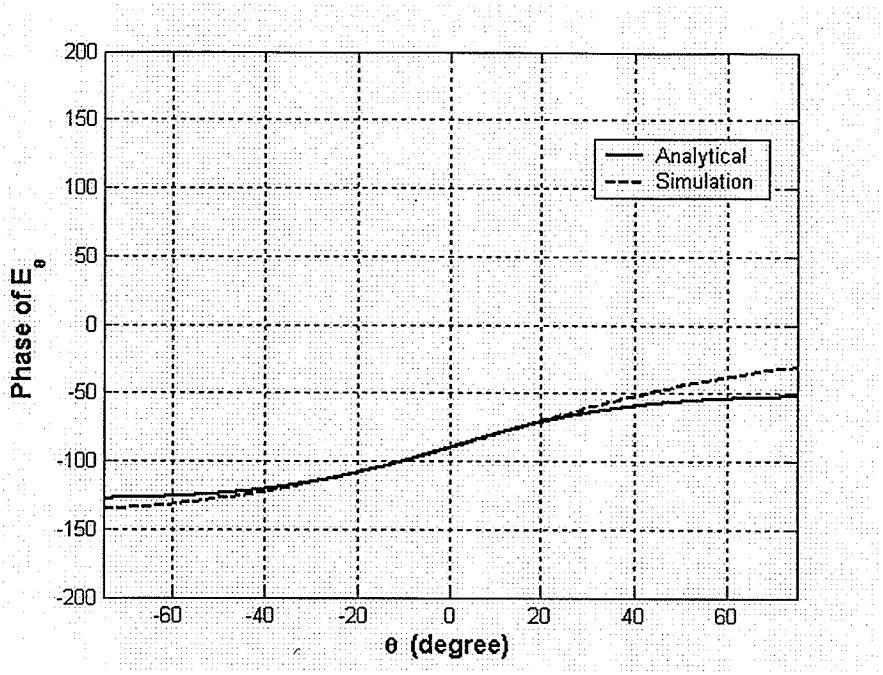

Fig. 5.25 Phase pattern of E_θ at $\phi = 0$ plane for the antenna shown in Fig. 5.19, when all patches are fed along x-axis and located at the origin, C_2/C_1=0.75 ∠ 0, C_0/C_1=0.1 ∠ 0

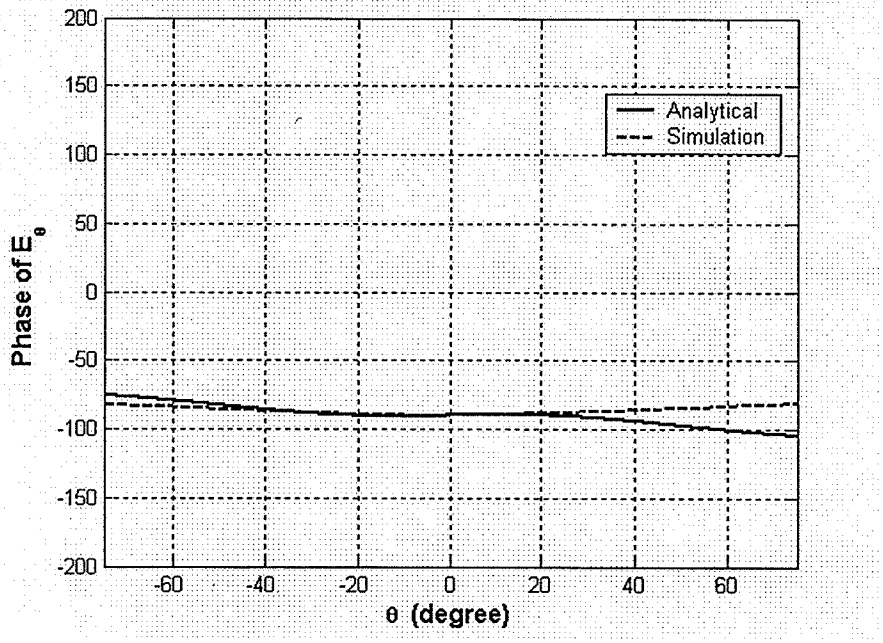

Fig. 5.26 Phase pattern of E_θ at $\phi = 0$ plane for the antenna shown in Fig. 5.19, when all patches are fed along x-axis $\left(r_0 = 0.15\lambda,\ \phi_0 = 180^\circ\right)$ and C_2/C_1=0.75 ∠ 0, C_0/C_1=0.1 ∠ 0

Figures 5.27 and 5.28 show the copolar and crosspolar radiation patterns at $\phi = 45^0$ and $\phi = 90^0$ planes, for the above two different amplitude ratios. As can be seen, the crosspolarization at $\phi = 45^0$ plane is more symmetric than the ones, obtained by simulation in chapters 3 and 4. This is due to the fact that, the ground plane size has been reduced by increasing the dielectric constant, which results in having more symmetric patterns. Moreover, the required value of the TM_{02} mode to decrease the crosspolarization level in practical design case is different from what was obtained by analytical model, according to Fig. 5.18. One reason is that, the physical radius of each mode over the finite ground plane changes in the numerical simulation, since this package considers infinite substrate for each layer affecting the fringing field, and eventually the patch size changes. Another reason is that, we compare the results with different ground plane sizes, like infinite in analytical model and finite in simulation. The other reason is that, the couplings between the three ports were ignored in the analytical model while there are considerable couplings between these three modes.

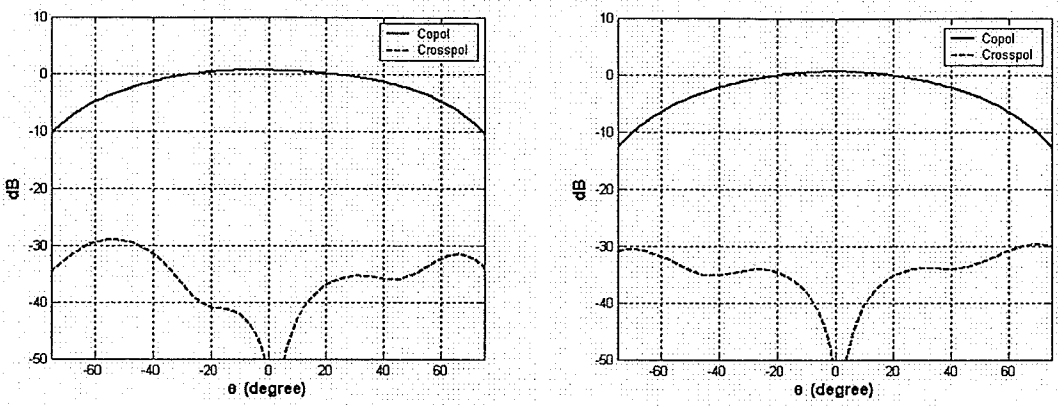

(a) *(b)*

Fig. 5.27 Copolar and crosspolar radiation patterns of the antenna shown in Fig. 5.19, when all patches are fed along x-axis, $\frac{C_2}{C_1} = 1\angle 0, \frac{C_0}{C_1} = 0.25\angle 0$ *at*

(a) $\phi = 45^o$, *(b)* $\phi = 90^o$

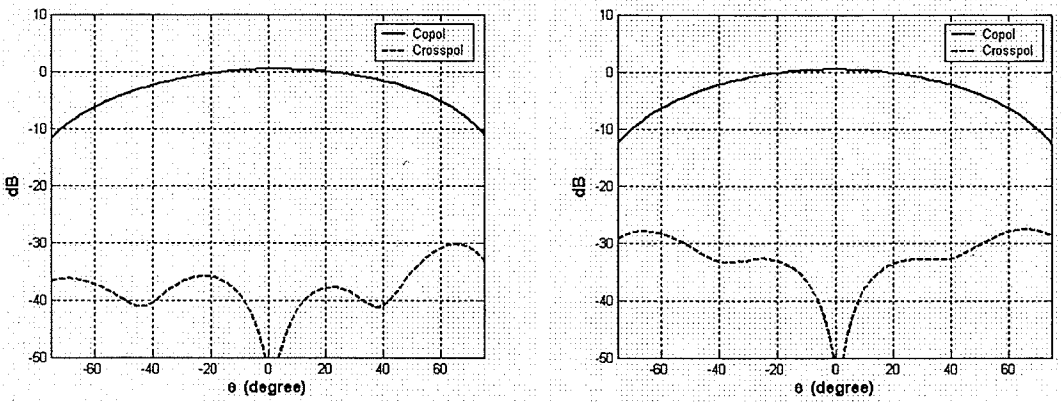

(a) *(b)*

Fig. 5.28 Copolar and crosspolar radiation patterns of the antenna shown in Fig. 5.19, when all patches are fed along x-axis, $\frac{C_2}{C_1} = 0.75\angle 0, \frac{C_0}{C_1} = 0.146\angle 0$ *at*

(a) $\phi = 45^o$, *(b)* $\phi = 90^o$

5.4 Summary

In this chapter, the phase centre location, main beam and polarization of a multilayer antenna operating at TM_{11}, TM_{21} and TM_{02} modes were studied both analytically and numerically. It has been shown that, by adding the TM_{02} mode to TM_{11} and TM_{21} modes, one can decrease the crosspolarization level. There are good agreements between analytical results, using the cavity model, and numerical results based on a Method of Moment, except due to the finite ground plane size, coupling between modes and infinite dielectric material in the simulation, the crosspolarization properties are not completely the same, since these parameters have pronounced impact on the microstrip antenna radiation patterns [21].

It was shown that, there is a global phase centre location for the antenna operating at TM_{11}, TM_{21} and TM_{02} modes, when C_0/C_1 is less than 0.35. By adding the TM_{02} mode to the dominant and TM_{21} modes, the phase centre moved further away from its physical center, comparing to that of the antenna operating at TM_{11} and TM_{21} modes. In addition, the TM_{02} mode provides an option to minimize the crosspolarization level over the boresight angle, while the phase centre location remains unchanged. This feature needs an adjustment on the excitation amplitudes of all three modes.

Chapter 6

Proposed feeding technique for Multilayer Microstrip Antenna

6.1 Introduction

There are several methods to feed a microstrip patch antenna including probe feeding, transmission line feeding, and slot coupling methods. Among them, the probe feeding is the most common method. In this thesis, all design examples were fed by coaxial feeding. When there is a single layer microstrip antenna, the probe feeding technique is very straightforward. For two and multilayer structures, in which every layer has to be fed individually, this method should be accompanied by other considerations in order to minimize the coupling effects, to excite each layer as desired as possible. This chapter proposes a feeding structure for the antennas discussed in chapters 3 and 5, operating at the fundamental mode and higher order modes. The idea is based on finding the electric field nulls and then passing the probe feeds of next top layers through these locations which can be shorted to the ground plane without perturbing the fields inside the cavity region of each mode.

6.2 Probe feed geometry for the two-layer antenna operating at TM_{11} and TM_{21} modes

If the patch is located on the x-y plane, the z-component of the electric field between the patch and ground plane, for all TM_{nm} modes, may be expressed as:

$$E_z = E_0 J_n(k\rho)\cos n\phi \qquad (6.1)$$

Where $J_n(k\rho)$ are the Bessel functions of order n, and n is an integer number. When the argument of these functions is zero, i.e. at the center of the patch, these functions are zero for all values of n, except zero. This means, the electric field inside the cavity at the center of the patch is very weak for all modes, except $n = 0$, so that, one may place a shorting via from the patch to the ground plane, at the patch center and pass the coaxial line through this via. This method is known as the center-feeding method discussed in [22-23].

In chapter 3, we excited one patch from the bottom and another one from the top, in order to simulate the antenna with a minimum coupling between the ports and simplify the model. However, this model is not practical. So, for the antenna discussed in chapter 3 operating at TM_{11} and TM_{21} modes, i.e. $n \neq 0$, we could use the center-feeding method explained above. The TM_{21} mode could be excited directly from the bottom, as a conventional probe feed. The top patch could be excited by passing a coaxial line through a hole at the center of the ground plane, the middle patch, and the top patch. Then, a microstrip line could connect this coaxial line to the 50Ω feed point of the top patch, where a via will connect the upper patch to the middle patch, about 0.25λ away from the center of TM_{11} patch. Figure 6.1 illustrates the geometry of the antenna with this feeding

structure. The holes at the center of each patch must be shorted to the ground plane in order to avoid the excitation of the TM_{02} mode. The central shorting post does not perturb the fields between the layers, since the electric field is zero at the center. In this structure, the middle layer plays the ground plane role for the top patch affecting the resonant frequencies [23].

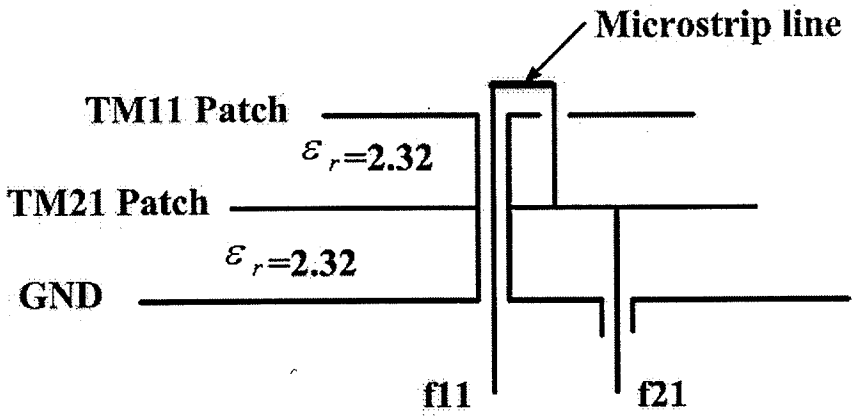

Fig. 6.1 Geometry of a two-layer circular Microstrip antenna operating at TM_{11} and TM_{21} modes using center-feeding technique

As the simulation package used in this thesis was a two-dimensional simulator, we have to model the central shorting post. Thus, two circular slots, each of diameter greater than the diameter of probe feed, were placed at the patch centers, then eight shorting vias were used to connect the upper and lower patches. Figure 6.2 shows the geometry of the antenna, which used this method to excite the two-layer microstrip antenna operating at TM_{11} and TM_{21} modes.

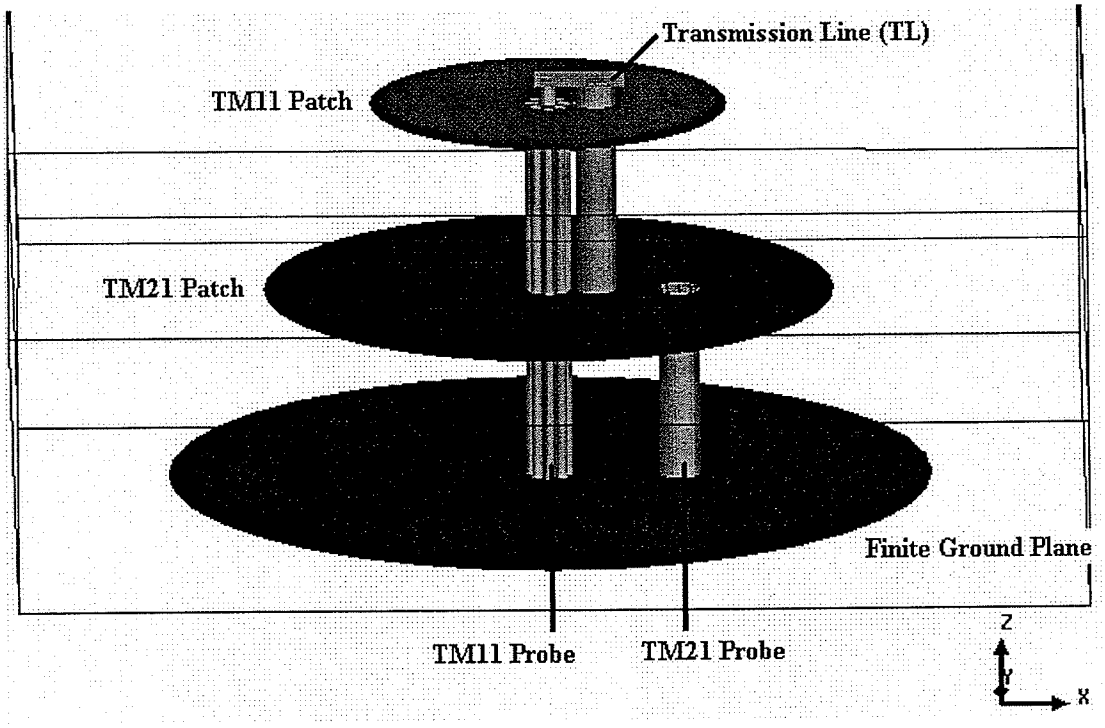

Fig. 6.2 The geometry of stacked patches operating in TM_{11} and TM_{21} modes over finite ground plane

$$a_{TM11} = 5.6mm,\ a_{TM21} = 8.95mm,\ a_{ground} = 12mm$$

$$\rho_f^{TM11} = 1.5mm \qquad \phi_m^{TM11} = 0$$

$$\rho_f^{TM21} = 4.1mm \qquad \phi_m^{TM21} = 0$$

$$h_1 = h_2 = 1{,}5mm,\ TL\ width=1.7mm,\ h=0.2mm$$

The dielectric constant of the substrate used in Fig. 6.2 is 2.32 while the dielectric between the microstrip line, which connects the center probe to the 50Ω feed point, and the top layer is air. The width of this transmission line is 1.7mm and is placed at a height of 0.2mm over the top layer. The piece of transmission line used in the feed structure also changes the phase difference between two feeds which has to be taken into account.

For the identical material used as a substrate for each layer, the size of TM_{11} patch is smaller than TM_{21} patch as explained before. So, in order to reduce the blockage

presented by the upper patch to below one [24], the TM_{11} patch was located on the top layer, the TM_{21} patch on the middle layer and the ground plane on the bottom.

The scattering parameters of the antenna shown in Fig. 6.2 are illustrated in Fig 6.3. The return loss for both ports is less than -10dB and the coupling between the two ports is about -21dB at the frequency of 10GHz.

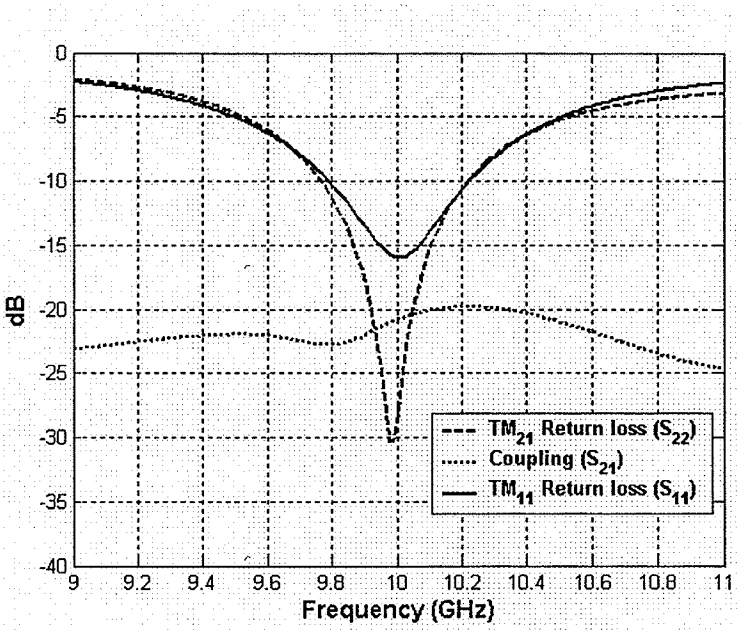

Fig. 6.3 Scattering parameters of stacked patch antenna shown in Fig. 6.2 operating in TM_{11} and TM_{21} modes over finite ground plane

The ground plane size of the antenna shown in Fig. 6.2 is 0.8λ, which can provide symmetric crosspolarization pattern based on [10]. The radiation patterns to the antenna of Fig. 6.2 are shown in Fig. 6.4 at $\phi = 45^{o}$ plane. The crosspolarization patterns are not completely symmetrical and further ground plane size reduction may be required.

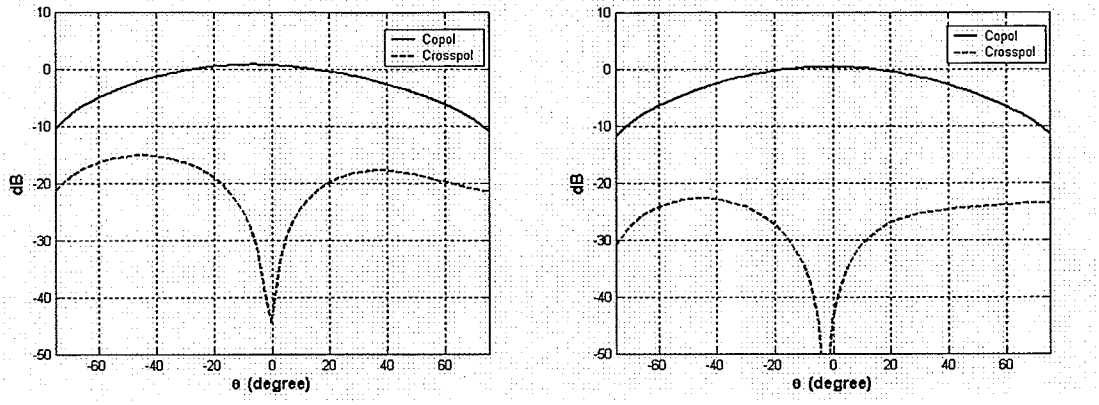

(a) *(b)*

Fig.6.4 Copolar and crosspolar of stacked patch antenna shown in Fig. 6.2 at $\phi = 45^{o}$ plane When both patches are fed along x-axis

(a) $\frac{C_2}{C_1} = 1\angle 0$, *(b)* $\frac{C_2}{C_1} = 0.5\angle 0$

6.3 Probe feed geometry for the three-layer antenna operating at TM_{11}, TM_{21} and TM_{02} modes

The electric field between the TM_{02} patch and ground plane is governed by the first kind Bessel function of order zero, as expressed in equation 6.2. This function is finite and has the peak amplitude when the argument is zero, emphasizing that the field at the patch center is strong.

$$E_z = E_0 J_0(k\rho) \qquad (6.2)$$

So, the center-feeding technique discussed above could not be applied for the TM_{02} patch. If one could place the TM_{02} patch on the top layer, the center feeding may be applied to the two other modes and the top layer could be fed at its center. In order to place the TM_{02} patch on the top layer, one needs to use a different substrate to reduce the patch size for TM_{02} mode. So, the layer assignment from the top to the bottom would be TM_{02}, TM_{11} and TM_{21}, respectively. By choosing a high dielectric constant for the TM_{02} patch, this arrangement will be possible. One example is shown in Fig. 6.5. But the problem we had in simulation was infinite size of the substrate which does not allow to properly reduce the patch size due to the effect of superstrate on the patch size based on [25, 26].

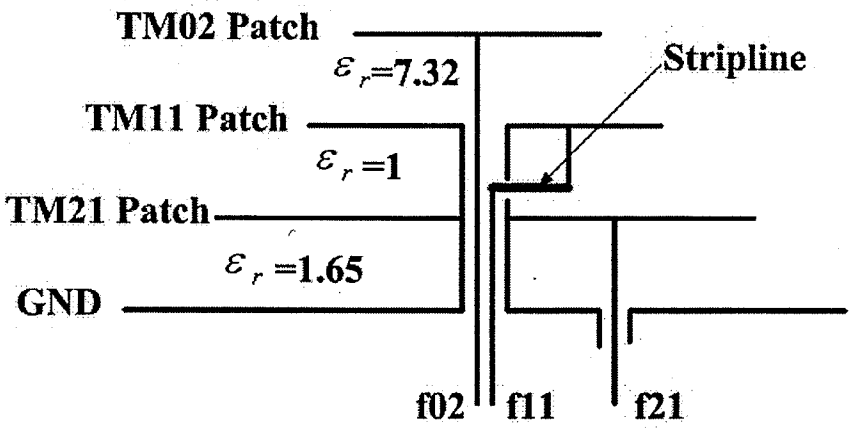

Fig. 6.5 Geometry of a stacked microstrip antenna with different dielectric constants for each layer

In case of using an identical material for all three modes, the order of layers from the top to the bottom must be as TM_{11}, TM_{21} and TM_{02}, respectively, in order to reduce the blocking effect. Therefore, we have to find the locations of field-null between the TM_{02} mode patch and the ground plane and pass the feeds of the other top patches, through these shorting posts. The first root of the first kind Bessel function of order zero happens at 2.405 (the other roots will be outside the patch and are not of interest). Using equation 2.8 and Table 2.1:

$$3.8317\frac{\rho}{a_{TM02}} = 2.405 \quad \Rightarrow \quad \rho = 0.6277 a_{TM02} \qquad (6.3)$$

So, the electric field is zero on a cylindrical wall inside the TM_{02} cavity with radius of $0.6277 a_{TM02}$. In the simulation, this value is changed to $0.71 a_{TM02}$.

Since the TM_{02} patch is the largest and in the bottom, it can be probe fed directly from bellow at its center, where the field is strong. For the remaining two modes, i. e. TM_{11} and TM_{21} modes, their respective feed cables can be passed through the TM_{02} patch at a radius of $0.71 a_{TM02}$, where the field is zero. Figure 6.6 shows these two feed cables on opposite sides of the patch axis. Above the TM_{02} patch these cables feed two stripline feeds. The right side cable feeds the TM_{21} mode, and its stripline S_3 is terminated where this mode has 50Ω impedance, and is connected to the patch through a via. The left side cable is connected to another feed cable, at the centre of the TM_{21} patch, through a second stripline S_2. This second cable and the stripline S_1 feed the upper TM_{11} mode patch. This configuration is similar to the center-feeding technique in [22-23]. The stripline S_1 connects the central feeding cable to the 50Ω feed point of the TM_{11} patch, as shown in Fig. 6.6. The latter central feed cable is approximated by a central via, to

connect S_2 to S_1, and shorting peripheral vias. In this manner all three patches are fed appropriately by their respective signals, with minimum interactions.

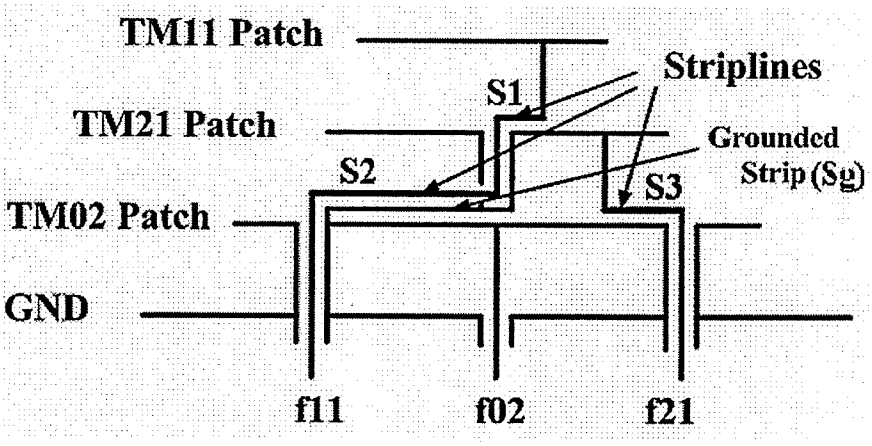

Fig. 6.6 The side view geometry of three stacked patches operating in TM_{11}, TM_{21} and TM_{02} modes, Line widths S_1=1.5mm, S_2=2.5mm, S_3=1.3mm, Sg=2mm

The three dimension view of the antenna with the above feeding structure is shown in Fig 6.7. The width of transmission line S_2 is made narrower near the central shorted vias, in order to pass through these grounded vias at the center and connect to the central feeding cable. As can be seen, this method increases the number of layers, increasing the antenna cost in terms of fabrication. Its simulated performance was discussed in chapter 5.

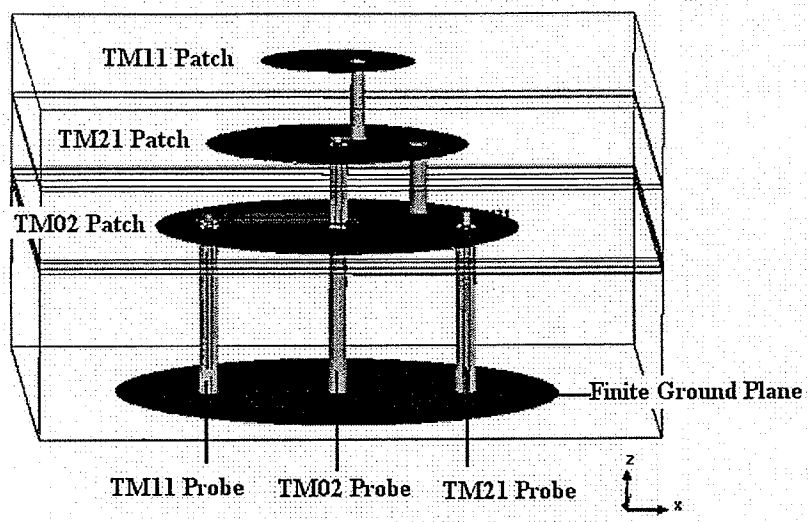

Fig. 6.7 The geometry of stacked patches operating at TM_{11}, TM_{21} and TM_{02} modes over a finite ground plane

$$a_{TM11} = 5.588mm,\ a_{TM21} = 9.4mm,\ a_{TM02} = 13.07mm,\ a_{ground} = 16mm$$
$$\rho_f^{TM11} = 1.4mm,\ \phi_m^{TM11} = 0$$
$$\rho_f^{TM21} = 5.83mm,\ \phi_m^{TM21} = 0$$
$$\rho_f^{TM02} = 0mm,\ \phi_m^{TM02} = 0$$
$$h_1 = h_2 = 1.5mm,\ h_3 = 3mm,\ \varepsilon_r = 2.32$$

6.4 Summary

This chapter has covered the probe feeding methods for multilayer circular microstrip antennas, operating at fundamental and two next higher order modes, discussed in chapters 3 and 5. The idea is based on placing a shorting post at the location of field-nulls between the patch and ground plane, where it does not perturb the fields inside the cavity. Then, a probe is passed through the post, along with a section of transmission line, to connect the extended probe to the 50Ω feed point of the patch. The disadvantage of this method, especially when the $n = 0$ mode exists, is that additional layers should be assigned for placing the transmission lines, which increase the antenna fabrication cost.

Chapter 7

Conclusion

7.1 Summary

This thesis provided a thorough study of the phase centre location and polarization of stacked circular microstrip patch antennas, excited in multiple modes. A single disk antenna operating at its fundamental mode, which generates a broadside radiation pattern, has a phase centre at its origin, but adding the higher order modes may change its phase centre. In such a case, it was shown how one can find the phase centre of the antenna by simply displacing the antenna and investigating the antenna far field phase distributions. Three different stacked antennas were studied, both analytically using a cavity model and numerically based on Method of Moment.

The first antenna was operating at the TM_{11} and TM_{21} modes, when both patches were fed along x-direction, or when the feeds were 45 degrees apart. The phase centre of this antenna depended on the excitation amplitude and phase of each mode. It was shown that, if the phase difference between these two modes was 90^{o}, the phase centre of the antenna was located at its center. In addition, it is possible to have a broadside radiation pattern, but move the phase centre away from the origin, introducing the virtual antenna concept. The crosspolarization of this antenna was increasing, when the excitation of the second higher order mode was increased. Moreover, there was a global phase centre location, when the copolar radiation pattern was considered for amplitude ratios less than unity.

The second antenna was a two-layer circular patch operating at the TM_{11} and TM_{02} modes. By exciting the two patches with a quadrature phase shift of 90°, the far field phase pattern was constant over the main beam, implying the phase centre being at the origin. The crosspolarization level was also increased with higher mode amplitude ratios. This antenna had a global phase centre location for amplitude ratios less than 0.45.

The third antenna was a three-layer circular microstrip patch antenna, when the lower patch operated at the TM_{02} mode, which has a circularly symmetrical pattern with a null at the broadside, the middle patch generated at the TM_{21} mode, which has a boresight-nulled radiation pattern, and the upper patch radiated the TM_{11} mode, which has a broadside radiation pattern. It was shown that, the TM_{02} mode provides an option to minimize the crosspolarization level over the boresight angle, while the phase centre location remains unchanged. This feature needs an adjustment on the excitation amplitudes of all three modes. Moreover, by adding the TM_{02} mode to the TM_{11} and TM_{21} modes, the phase centre moved further away from that of the antenna operating at TM_{11} and TM_{21} modes.

The phase centre of this antenna could be controlled by the excitation amplitude and phase of each mode. Due to the fact that, the TM_{02} mode has the strongest field at its center, it prevented a central-feeding method described in [22-23]. So, a novel probe feeding structure was introduced for such an antenna based on finding the electric field nulls of the TM_{02} mode, which is on a cylindrical wall inside the TM_{02} mode cavity, at a finite radius from its center.

7.2 Future work

A few future research topics arising from controlling the phase centre and polarization of an antenna are listed below that need to be studied.

- Study of phase centre location and polarization of stacked rectangular patch antennas operating at higher order modes.
- Study of possibilities of adding the TM_{0n} modes to reduce the crosspolarization other that n=2.
- Applying the idea of controlling the phase using higher order modes, to microstrip reflectarrays, instead of using conventional methods like stubs or patches of variable size, rotating the elements to perform the phase shifts.
- Employing the central feeding method for the stacked antenna, operating at the TM_{11}, TM_{21} and TM_{02} modes, by using different substrates for each layer in such a way that the TM_{02} mode can be etched on the top layer with a minimum blockage effect.
- Using higher order mode microstrip antenna for beam shaping and scanning.
- Investigating the possibility of designing multimode circular microstrip antennas using a single layer structure.

BIBLIOGRAPHY

1. G. A. Deschamps, "Microstrip Microwave Antennas," presented at *the 3rd USAF Symposium on Antennas*, 1953.
2. H. Gutton and G. Baissinot, "Flat Aerial for Ultra high Frequencies," *French Patent No. 703113*, 1955.
3. C. A. Balanis, *Antenna Theory Analysis and Design*. Hoboken, NJ: John Wiley and Sons Inc., 2005.
4. Y.J Guo, A. Paez, R.A. Sadeghzadeh, and S.K. Barton, "A circular patch antenna for radio LAN's", *IEEE Trans. On Antennas and Propagation*, vol. 45, Issue 1, pp. 177 – 178, January 1997.
5. M. N. Solomon, "Multi-mode patch antenna system and method of forming and steering a spatial null," *US Patent No. 6252553 B1, 2001.*
6. J. Haung, "Circularly polarized conical patterns from circular microstrip antennas", *IEEE Trans. On Antennas and Propagation*, vol. 32, Issue 9, pp. 991-994, September 1984.
7. L. Shafai, "Properties of microstrip phased array with self scanning elements", in *1989 Antennas and Propagation Society International Symposium Digest*, vol.2 pp. 986 – 988.
8. K. Antoszkiewicz and L. Shafai, "Impedance characteristics of circular microstrip patches", *IEEE Trans. On Antennas and Propagation*, vol. 38, No. 6, June 1990.
9. A.D. Olver, P.J.B. Clarricoats, A.A. Kishk, and L. Shafai, *Microwave Horns and Feeds*. New York: IEEE Press, USA, 1994.

10. A.A. kishk and L. Shafai, "Optimization of microstrip feed geometry for prime focus reflector antennas", *IEEE Trans. on Antennas Propagation*, vol. 37, pp. 445-451, 1989.

11. A.A. Kishk and L. Shafai, "The effect of various parameters of circular microstrip antennas on their radiation efficiency and the mode excitation", *IEEE Trans. On Antennas and Propagation*, vol. AP-34, No. 8, pp. 969 – 976, Aug. 1986.

12. L.I. Basilio, J.T. Williams, and D.R. Jackson, "Defining an effective point of radiation for a microstrip patch antenna", in *Symposium on Antenna Technology and Applied Electromagnetics,* 2002, pp. 455-458.

13. R. Garg, P. Bhartia, I. Bahl, and A. Ittipiboon, *Microstrip Antenna Design Handbook.* Norwood, MA: Artech House, 2001.

14. A.G. Derneryd, "Analysis of the microstrip disk antenna element", *IEEE Trans. On Antennas and Propagation*, vol. AP-27, No. 5, pp. 660 – 664, Sep. 1979.

15. L.C. Shen, S.A. Long, M.R. Allerding, and M.D. Walton, "Resonant frequency of a circular disk printed-circuit antenna", *IEEE Trans. On Antennas and Propagation*, vol. AP-25, pp. 595-596, 1977.

16. Rajanish and T.S. Vedavathy, "A generalized expression for resonant frequency of circular microstrip antennas", in *2000 Microwave Conference*, Asia-Pacific 3-6 Dec. 2000, pp. 743 – 746

17. L. Yu, B. Rawat, and M. Williamson, "An omnidirectional microstrip antenna for mobile communications", in *1991 Antennas and Propagation Society International Symposium, AP-S. Digest*, vol.2, pp. 848 – 851.

18. IEEE Std 145-1993, *IEEE Standard Definition of Terms of Antennas.*

19. J. Watkins, "Circular resonant structures in microstrip", *Electronic Letters*, vol. 5, pp. 524-525, 1969.

20. A.C. Ludwig, "The definition of cross-polarization", *IEEE Trans. On Antennas and Propagation*, vol. 21, pp. 116-119, 1973.

21. S. Noghanian and L. Shafai, "Control of microstrip antenna characteristics by ground plane size and shape", *IEE proceedings on Microwaves, Antennas and Propagation*, vol. 145, Issue 3, pp. 207-212, June 1998.

22. K.S. Kona, M. Manteghi, and Y. Rahmat-Samii, "A novel feed system for soil moisture spaceborne radar: dual-polarized stacked patch microstrip array", in *2004 Antennas and Propagation Society International Symposium,* vol. 4, pp. 4368 – 4371.

23. K.S. Kona and Y. Rahmat-Samii, "Design and analysis of a novel probe-feeding method for stacked microstrip patch antennas", in *2003 Antennas and Propagation Society International Symposium,* vol. 1, pp. 425 – 428.

24. S. Chebolu, S. Dey, R. Mittra, and M. Itoh, "A dual-band stacked microstrip antenna array for mobile satellite applications", in *1995 Antennas and Propagation Society International Symposium Digest*, vol. 1, pp. 598 – 601.

25. K.M. Luk, W.Y. Tam and C.L. Yip, "Analysis of circular microstrip antennas with superstrate", *IEE Proc. On Microwaves, Antennas and Propagation*, vol. 136, Issue 3, pp. 261-262, June 1989.

26. D. Guha and J.Y. Siddiqui, "Resonant frequency of circular microstrip antenna covered with superstrate dielectric", *IEEE Trans. on Antennas and Propagation*, vol. 51, Issue 7, pp. 1649-1652, July 2003.